Wide Field 3D Orientation Contrast Microscopy

Breedveld-3D-oriëntatiecontrastmicroscopie

Hadi Pirgazi

Promotoren: prof. dr. ir. L. Kestens, prof. dr. ir. R. Petrov
Proefschrift ingediend tot het behalen van de graad van
Doctor in de Ingenieurswetenschappen: Materiaalkunde

Vakgroep Toegepaste Materiaalwetenschappen
Voorzitter: prof. dr. ir. J. Degrieck
Faculteit Ingenieurswetenschappen en Architectuur
Academiejaar 2014 - 2015

UNIVERSITEIT
GENT

ISBN 978-90-8578-799-0
NUR 971
Wettelijk depot: D/2015/10.500/43

Acknowledgments

Knowledge is in the end based on acknowledgement.
Ludwig Wittgenstein (Austrian-British philosopher 1889-1951)

This research was carried out in the department of materials science and engineering of Gent University during the last five years. After completion, it is a great pleasure to look over the past years and remember all the inspiring friends, lovely family and friendly colleagues who have helped and supported me during this long but delightful journey.

First and foremost I offer my sincerest gratitude to my supervisor, Professor Leo Kestens who accepted me as one of his PhD students in December 2009. During these five years he has shown a remarkable interest to my work, even in situations I would have qualified as desperate. He gave me the opportunity to expand my scientific background, and put me at the right track whenever I got lost. He always provided instructive comments and evaluations at every stage of my thesis development. Many thanks for showing constant interest in my work and giving me whatever a young researcher needs. I particularly appreciate his outstanding availability and generosity in all situations. Leo, I would always be thankful to you for believing in me and asking me to join to your research team. I am indebted to you forever!

I would like to give special thanks to Professor Roumen Petrov who was closely involved in this research. I thoroughly enjoyed the numerous discussions on complex topics and the way that he motivated me to further my project. Roumen, without your helps my research would not have been accomplished. Thanks a lot.

I am always grateful to my previous professors during my Bachelor and Master programs, professors of department of materials science and engineering of Isfahan University of Technology and Sharif University of Technology, who supported me to learn fundamentals of Materials Science.

My special gratitude also goes to the committee members for their critical comments on this thesis and their willingness to be part of the promotion committee.

I would also like to thank the administrative and technical staff of the department

of materials science and engineering, Marnix Van Dorpe, Alex De Groote, Vitaliy Bliznuk, Aline De Bondt, Ilse Vercruysse, Roger Van Hecke, Christiana Sonck and Michel Moors for their assistance during my PhD.

I extend my appreciation to Dr. Tom Van de Putte and Dr. Sigrid Jacobs from OCAS NV for providing the materials for part of this research.

I wish to sincerely thank, Dr. Sepideh Ghodrat at Delft University of Technology for her collaboration in part of this work. Sepideh, thanks a lot for your contribution in our publications, sharing your experiences and for your encouragement.

Next, I would like to thank all my colleagues from department of materials science and engineering of Gent University, who made my time here enjoyable and always made me feel at home. Let me especially thank Elisabete Pinto da Silva, Edgar Gomes de Araujo and Jurij sidor for all they have done for me during this period. Elisabete, Edgar and Jurij, I never forget all the parties, pizzas, fondues, BBQs and drinks which we had together.

Special thanks to An Verdiere for translating the summary of this thesis into Dutch.

I would like to thank again my colleague and friend Edgar Gomes de Araujo for his friendship and continuous support in my research. Edgar, even though I kept disturbing you at times, you were always willing to help and engage in fruitful discussions. Thanks a lot my friend.

I may not forget to thanks all my friends during these years in Gent, of whom the list of the names will be too long to be mentioned here. Thanks so much for the great times we have spent together.

My deepest gratitude goes to my family. Their constant inspiration and guidance kept me focused and motivated. I can't express my gratitude for my mom in words, whose unconditional love has been my greatest strength. Thanks mom for encouraging me in every decision I made in my life and for believing in my choices that led me to this place. The constant love and support of my brother and my lovely sisters is sincerely acknowledged.

Last but not least, my girlfriend Azadeh, of whom I have had her patience, friendship and understanding. Azadeh, your love, support and encouragement during the frustrating stage of my thesis writing have been really important to me. Thanks a lot.

Hadi Pirgazi

Gent, 2015

Summary

Microstructure is an important aspect of materials science, which is of essential importance of material characteristics and performance. Due to its crucial role, characterization of microstructures has been at the core of any materials research program. For decades, two-dimensional (2D) characterization techniques including light microscopy, Scanning Electron Microscopy (SEM) and Electron Back-Scattering Diffraction (EBSD) have been extensively employed to reveal detailed microstructural characteristics of various materials. These conventional techniques have been successful in observing many microstructural features at different length scales, from sub-micrometer (e.g. internal structures of grains and small precipitates) to millimeter (e.g. large grains in silicon steels). However, microstructures are of a three-dimensional (3D) nature, and all the above-mentioned techniques are applied on 2D planar sections cut through the material. As a consequence, by a conventional 2D characterization parts of the information of the microstructure remain inaccessible, such as e.g. the number of features per volume unit, the true size and shape of microstructural features, the connectivity between features, and the inclination of planar interfaces associated with grain boundaries or cracks. In some cases, this information may be partially derived from 2D sections by stereological methods. However, the accuracy of such methods highly depends on the extent to which the microstructure complies with a set of topological assumptions. Therefore, real 3D characterization methods are required to investigate some important features of the microstructure.

The techniques for 3D characterization of the microstructures are based on two different approaches: (i) observation with high energy radiation (i.e. atom probe tomography, 3D X-ray diffraction and X-ray tomography) and (ii) by serial sectioning. With regard to acquisition speed, resolution, field width and complexity, each of these techniques has advantages and disadvantages. According to current state-of-the-art technology, serial sectioning offers the best balance between high resolution and high field width. Furthermore, this technique does not need complex instruments and can be performed by conventional characterization facilities. For these reasons, it has been the most widely used method to acquire 3D data for different materials at the meso and microscale.

In the serial sectioning technique, the third dimension of the microstructure is revealed by a series of closely spaced parallel sections. The usual method for serial sectioning involves the sequential removal of parallel layers of the sample, interrupted by imaging (e.g. by EBSD technique) of the planar sections. The

removal of the material can be performed with different methods, e.g. mechanical polishing, chemical polishing, Focused Ion Beam (FIB) tomography and laser or electrical discharge ablation. Fully automated EBSD combined with FIB tomography is a precise but time consuming method that can be used for measuring small volumes (~μm^3 scale) and consequently its relevance is limited to materials with very small characteristic features (nm^3 scale). On the other hand, serial sectioning by mechanical polishing is a valid alternative to obtain reliable microstructural data of bulk metals for structural and functional applications.

In this thesis, serial sectioning by mechanical polishing was employed to collect several consecutive parallel EBSD sections of different materials: non-oriented electrical steels, compacted graphite iron, and pure nickel. The collected sections were used to reconstruct the 3D microstructural image. A dedicated algorithm based on the minimization of misorientation between two adjacent sections was developed to accurately align the sections. By employing this algorithm, any stretching, translational and rotational misalignment between the sections can be corrected. Surface meshing by triangulation between corresponding grain boundary traces of the adjacent sections was used to reconstruct the grain boundary surfaces. The developed technique and algorithms were used to study the 3D dependent material properties in different case studies.

The interaction between grain boundaries and magnetic domains during the magnetization process of non-oriented electrical steels was studied considering the curvature of the grain boundary (GB) plane. The density of magnetic free poles at a grain boundary depends not only on the misorientation across the boundary but also on the relative angle between the GB normal and the magnetization vectors in two neighboring grains. Experimental results from 3D EBSD experiments were employed to measure the GB orientation for several samples with different chemical composition and grain size. The values of free pole density, grain size, magnetocrystalline anisotropy energy, and silicon equivalent were used to derive an empirical model to predict the magnetic induction based on physical understanding of the interaction between the magnetic field variables and local microstructural variables. By comparing modeled and measured values of magnetic induction measured at low, medium and high magnetic fields, it was shown that the magnetization behavior can be more accurately predicted when the grain boundary characteristics are taken into account.

The developed 3D technique was used to meticulously characterize the complex crack path morphology of Compacted Graphitic Iron (CGI) that was tested under conditions of Thermo-Mechanical Fatigue (TMF). CGI is an important material for fabrication of cylinder heads in which heating and cooling cycles can lead to localized cracking due to TMF. By 3D investigation it is possible to find out how and by which mechanisms cracks develop in relation to microstructural features. To investigate the relationship to local microstructure, a fatigue specimen was cycled under TMF conditions to replicate the thermal and mechanical conditions in the valve bridge area of cylinder heads. A 3D data set was reconstructed from EBSD sections measured from the crack, including the crack tip. The 3D image was used to study the crystallographic preference of fracture plane. Based on the precise

quantitative microstructural analysis, it is found that graphite particles do not only play a crucial role in the crack initiation, but also are of primary significance for crack propagation, i.e. crack growth is enhanced by the presence of graphite particles. This can be derived from the observation that the density of graphite particles on the fracture plane is more than double as high as in any other arbitrary plane of the structure. The results did not indicate a particular crystallographic preference of the fracture plane, i.e. the crystal plane parallel to the fracture plane was nearly of random orientation.

To understand the role of grain boundaries on the material properties, a full 3D characterization of grain boundaries is required. Many important properties of materials such as corrosion resistance, brittleness, toughness and magnetic properties are affected by the grain boundaries. Five parameters are required to fully describe a grain boundary plane: three parameters corresponding to the misorientation across the grain boundary and two parameters, which specify the orientation of the grain boundary plane known as the grain boundary normal vector. Three parameters of the misorientation and one parameter of the grain boundary normal can be directly derived from a 2D EBSD. The fifth parameter can also be estimated from planar sections using stereological methods, or can be precisely extracted from 3D data. The mentioned serial sectioning technique and the corresponding alignment and triangulation algorithms were employed to reconstruct the 3D microstructure of a pure nickel sample. The relative frequency of occurrence of grain boundaries with specific misorientation and boundary plane normal, known as the Grain Boundary Character Distribution (GBCD), was derived from reconstructed grain boundary planes. The results show that more precise topological information can be obtained after precise translational and rotational alignment and correction of the planparallelity between neighboring sections. It was also found that the grain boundary planes carrying a Σ3 misorientation (<111>60°) are dominantly parallel to the {111} crystal plane, which indicates the presence of coherent twin boundaries.

Samenvatting

Microstructurele controle is een belangrijk aspect van de materiaalkunde omdat het direct de eigenschappen van het materiaal en de prestaties beïnvloedt. Door zijn cruciale rol is karakterisatie van microstructuren nog steeds de kern van elk materiaalkundig onderzoeksprogramma. Al tientallen jaren worden twee-dimensionale (2D) karakterisatietechnieken, waaronder lichtmicroscopie, scanning elektronenmicroscopie en Electron Back-Scattering Diffractie (EBSD), uitgebreid gebruikt om gedetailleerde microstructurele kenmerken van allerlei materialen in kaart te brengen. Deze conventionele technieken kunnen veel kenmerken van microstructuren in verschillende lengteschalen onthullen, van sub-micrometer (bijvoorbeeld interne structuren van korrels en kleine precipitaten) tot millimeter (bijvoorbeeld grote korrels in siliciumstaal). Reële microstructuren zijn echter van driedimensionale (3D) aard en alle bovengenoemde technieken worden toegepast op 2D vlakke secties die door door het material gesneden worden. Hierdoor, blijft bij een gebruikelijke 2D karakterisatietechniek belangrijke informatie omtrent de microstructuur achterwege. De hoeveelheid karakteristieke elementen per volume, de ware grootte en 3D vorm van microstructurele eigenschappen zijn voorbeelden van microstructurele informatie die slechts ten dele verkregen wordt bij 2D microscopie. Een deel van deze informatie kan geschat worden met behulp van stereologische technieken uit een 2D sectie. De nauwkeurigheid van deze methode is echter sterk afhankelijk van een aantal aannames omtrent de statistische verdeling van de betrokken microstructurele elementen. Daarom zijn 3D karakterisatie methoden nodig om een aantal belangrijke kenmerken van de microstructuur te onderzoeken.

De technieken voor 3D karakterisatie van microstructuren zijn gebaseerd op twee verschillende benaderingen: (i) observatie met hoog—energetische straling (zoals atom probe tomografie, 3D röntgendiffractie en X-ray tomografie) en (ii) observatie door seriële sectionering. Met betrekking tot de snelheid van de meting, de resolutie, de lengteschaal en de complexiteit van de techniek en de instrumenten, heeft elk van deze technieken voor- en nadelen. Onder deze technieken is seriële sectionering de enige die een evenwicht kan vinden tussen hoge resolutie en hoge lengteschaal. Bovendien zijn voor deze techniek geen ingewikkelde instrumenten nodig en kan het uitgevoerd worden met gebruikelijke karakterisatiefaciliteiten. Om deze redenen is het de meest gebruikte methode om 3D microstructurele gegevens op de micro- en mesoschaal te bekomen.

In de seriële sectioneringstechniek wordt de derde dimensie van de microstructuur

onthuld in een reeks van dicht bij elkaar gelegen evenwijdige. De gebruikelijke werkwijze voor deze techniek bestaat erin om parallelle lagen van het monster één vor één te verwijderen, afgewisseld door beeldvorming (bijvoorbeeld met EBSD) van de vlakke secties. De verwijdering van het materiaal voor seriële sectionering kan uitgevoerd worden met verschillende methoden zoals mechanisch polijsten, chemisch polijsten, Focused Ion Beam (FIB) tomografie en ablatie met behulp van laserstraling of elektrische ontlading. Volledig geautomatiseerde EBSD voorzien gecombineerd met FIB is een nauwkeurige maar tijdrovende tomografische methode die gebruikt kan worden voor het meten van kleine volumes en daardoor is de toepassing beperkt tot materialen met een zeer kleine gemiddelde korrelgrootte. Anderzijds, seriële sectionering door mechanisch polijsten lijkt een veelbelovende methode om betrouwbare microstructurele gegevens van bulk metalen voor structurele en functionele toepassingen te verkrijgen.

In deze thesis werd seriële sectionering door mechanisch polijsten gebruikt om om 3D beelden van de microstructuur te bekomen voor diverse materialen: niet-georiënteerd elektrisch staal, vermiculair gietijzer en zuiver nikkel. De verzamelde secties werden gebruikt om de 3D microstructuren te herconstrueren. Een specifiek algoritme gebaseerd op het minimaliseren van de misoriëntatie tussen twee aangrenzende secties werd ontwikkeld om de secties nauwkeurig uit te lijnen. Door gebruik te maken van dit algoritme, kan elke distortionele, translationele en rotationele uitlijningsfout tussen de secties gecorrigeerd worden. Oppervlakte meshing door triangulatie tussen overeenkomstige korrelgrenssegmenten van aangrenzende secties werd gebruikt om de korrelgrensvlakken te reconstrueren. De ontwikkelde techniek en algoritmes werden gebruikt om de 3D microstructurele kenmerken van diverse aard te bestuderen.

De interactie tussen korrelgrenzen en magnetische domeinen gedurende het magnetisatieproces van niet-georiënteerd elektrisch staal werd onderzocht, met speciale aandacht voor de rol van de kromming van korrelgrensvlakken. De dichtheid van de magnetisch vrije polen aan een korrelgrens is niet alleen afhankelijk van de kristallografische misoriëntatie aan de korrelgrenzen, maar ook van de relatieve hoek tussen de loodrechte op de korrelgrens en de magnetisatie-vectoren in twee aangrenzende korrels. De experimentele resultaten van 3D EBSD experimenten werden gebruikt om de korrelgrensoriëntatie en de dichtheid van de vrije polen te berekenen voor diverse monsters met verschillende chemische samenstelling en korrelgrootte. De waarden van vrije pooldensiteit, korrelgrootte, magnetokristallijne anisotropie energie en silicium-equivalent werden gebruikt in een empirisch model dat toelaat om de magnetische inductie te voorspellen op basis van dergelijke microstructurele en chemische toestandsvariabelen. Alhoewel het model essentieel empirisch van aard is, is het niettemin gebaseerd op een fysisch begrip van de wisselwerking tussen variabelen van het magnetische veld en lokale microstructurele variabelen. Door het vergelijken van gemodelleerde en gemeten waarden van magnetische inductie, gemeten bij lage, gemiddelde en hoge magnetische velden, werd aangetoond dat het magnetisatie gedrag nauwkeuriger voorspeld kan worden wanneer de korrelgrenseigenschappen in rekening gebracht worden.

De ontwikkelde 3D-observatietechniek werd gebruikt om de complexe morfologie en het scheurgedrag in vermiculair gietijzer (*Engelse afkorting*: CGI - Compacted Graphite Iron) als gevolg van thermo-mechanische vermoeiing (TMF) nauwgezet te karakteriseren. CGI is een belangrijk materiaal voor de productie van cilinderkoppen van vrachtwagenmotorblokken waarin verwarmings- en afkoelcycli kunnen leiden tot gelokaliseerde scheurvorming als gevolg van TMF. Door 3D-onderzoek is het mogelijk vast te stellen hoe het scheurpad zich een weg baant doorheen de microstructuur en welke elementen van de microstructuur hierbij van belang zijn. Daartoe werd een vermoeiingsproef uitgevoerd onder TMF condities om de thermische en mechanische omstandigheden na te bootsen in de cilinderkop van een motorblok. Een 3D dataset werd gereconstrueerd uit EBSD secties die gesampled werden in de buurt van de scheurtip. Deze dataset werd nadien gebruikt om de kristallografische voorkeur van het breukvlak te bestuderen. Op basis van de precieze kwantitatieve microstructurele analyse werd vastgesteld dat grafietdeeltjes niet enkel een cruciale rol spelen in de initiatie van de scheur, maar ook van primair belang zijn voor scheurpropagatie, d.w.z. scheurgroei wordt versterkt door de aanwezigheid van grafietdeeltjes. Dit blijkt uit het feit dat de dichtheid van grafietdeeltjes op het breukvlak meer dan dubbel zo hoog als in elk ander willekeurig vlak van de structuur. De verkregen resultaten wijzen niet op een bepaalde kristallografische voorkeur van het breukvlak, aangezien het kristalvlak evenwijdig aan het breukvlak bij benadering een willekeurige oriëntatie had.

De korrelgrens is bij uitsek één van de microstructurele aspecten waarvoor een 3D observatie noodzakelijk is voor een volledige structuurbepaling. Veel belangrijke eigenschappen van materialen zoals corrosieweerstand, broosheid, taaiheid en magnetische eigenschappen worden beïnvloed door de korrelgrenzen. Om het effect van korrelgrenzen op de materiaaleigenschappen te begrijpen, is een volledige karakterisatie van korrelgrenzen vereist. Vijf parameters zijn nodig om een korrelgrensvlak te beschrijven: drie parameters om de kristallografische misoriëntatie over de korrelgrens te kenmerken en twee parameters die de oriëntatie van het korrelgrensvlak bepalen aan de hand van de korrelgrensnormale. De drie kristallografische parameters en één parameter van de grensvlaknormale kunnen direct afgeleid worden uit een 2D EBSD scan. Aan de hand van een stereologische methode kan de vijfde parameter geschat worden op basis van vlakke secties. Een exacte bepaling is enkel mogelijk uit 3D-beelden. De reeds vermelde seriële sectioneringstechniek en de bijhorende uitlijnings- en triangulatie-algoritmes, die in het kader van dit onderzoek werden ontwikkeld, werden aangewend om de 3D microstructuur van een zuiver nikkel monster te reconstrueren. De relatieve frequentie van korrelgrenzen met een specifieke kristallografische misoriëntatie en grensvlaknormaal, beter bekend als de Grain Boundary Character Distribution (GBCD), werd afgeleid uit de 3D dataset. De resultaten tonen het belang van de translationele en rotationele uitlijning. Voor het onderzochte materiaal werd vastgesteld dat de korrelgrensvlakken met een Σ3 type misoriëntatie (<111>60°) overwegend evenwijdig zijn aan het {111} kristalvlak, wat wijst op de aanwezigheid van coherente tweelinggrenzen.

Table of Contents

List of Abbreviations

2D	Two-Dimensional
3D	Three-Dimensional
APT	Atom Probe Tomography
BCC	Body-Centered Cubic
CGI	Compacted Graphite Iron
CSL	Coincident Site Lattice
DCT	Diffraction Contrast Tomography
EBSD	Electron Back-Scatter Diffraction
FCC	Face-Centered Cubic
FIM	Field Ion Microscopy
GBCD	Grain Boundary Character Distribution
GBE	Grain Boundary Engineering
IPF	Inverse Pole Figure
LD	Loading Direction
MRD	Multiples of Random Distribution
ND	Normal Direction
ODF	Orientation Distribution Function
OIM	Orientation Image Microscopy
OPS	Oxide Polishing Suspension
RD	Rolling Direction
SEM	Scanning Electron Microscopy
TD	Transverse Direction
TEM	Transmission Electron Microscopy
TMF	Thermo-Mechanical Fatigue
XRD	X-Ray Diffraction

Chapter 1. Foreword

"The more I know, the less I know for sure."

Leo Kestens
(Inspired by the quote of John Lennon, "The more I see, the less I know for sure")

1.1. Introduction

Each microstructure is composed of two basic elements: lattice defects and second phase components, on a space scale ranging from Angstroms to meters. In order to fully characterize the microstructure of a crystalline material the following information is needed [1]:

i) the spatial distribution of crystallographic orientations;
ii) morphological characterization (type, shape, size and distribution) of all the microstructural elements;
iii) microstructural anisotropy by characterization of orientation distribution of microstructural elements.

These parameters ought to be represented in a statistically relevant manner by appropriate orientation and spatial correlation functions. The role of microstructure in materials science is of crucial importance for bridging the gap between processing parameters and material properties. Processing parameters influence the microstructure; and, in turn, the microstructure affects the material properties. Therefore, for materials research purposes it is of crucial importance to meticulously characterize, represent and investigate the microstructures.

The microstructure of materials is of a three dimensional nature. But the characterization of microstructure is conventionally carried out on two-dimensional (2D) sections. By conventional 2D analytical techniques, it is possible to characterize a vast number of microstructural features. However, there remain many features of the real three dimensional microstructure that can only be measured in three-dimension (3D).

The number of features per volume unit, the true size and shape of microstructural elements, the connectivity between features, the grain boundary inclination and

the interface morphology are examples of microstructural information that can be obtained only from 3D microscopy observation. Consequently, the 3D description of the microstructure is of crucial importance for a better conceptual and quantitative understanding of the structure-properties relationships in polycrystalline materials.

The direct techniques for 3D characterization of the microstructures are based on two different approaches: (i) observation with high energy radiation and [2, 3] and (ii) by serial sectioning [4-6]. Furthermore, some indirect stereological methods [7] have been proposed and employed to derive 3D information from 2D images.

So far, serial sectioning has been the most widely used method to acquire 3D data at the macro/microscale of opaque materials. This technique has been widely used to extract 3D information from various materials, including magnesia [8], lead-tin alloy [9], yttria [10], nickel [7, 11] and CuZr alloy [12]. In this technique, a series of closely spaced parallel sections reveal the third dimension of the microstructure. The usual method for serial sectioning involves the sequential removal of parallel layers of the sample, interrupted by imaging of the planar sections [4, 13], e.g. by Electron Back-Scattering Diffraction.

The removal of the material for serial sectioning can be performed with different methods: e.g. mechanical polishing, chemical polishing, Focused Ion Beam (FIB) tomography and laser or electrical discharge ablation [5]. Fully automated EBSD equipped with FIB is a precise but time consuming tomography method that can be used for measuring small volumes and consequently limits its application only for materials with a very small average grain size. On the other hand, serial sectioning by mechanical polishing seems to be a promising method to obtain reliable microstructural data of bulk metals for structural and functional applications. The latter is of primary interest in the present research.

1.2. Objective and outline of the thesis

The main aim of this work is to acquire, post-process, analyze and represent statistically representative data sets from 3D microstructures. To this purpose, the primary objectives of this research are:

- Establishing an appropriate procedure for acquiring 3D data sets covering wide fields of view, extending over various mm^3 of sample volume, employing serial sectioning by mechanical polishing;

- Developing required post-processing procedures including section alignment, segmentation of the dataset in constituent grains, and grain boundary surface meshing in order to reconstruct the 3D microstructural image.

The reconstructed 3D microstructure is employed to address several questions regarding the microstructure and its correlation with material properties and performance, which can only be answered by having the 3D data set. This aim translates into the following specific objectives of this research:

- To understand the role of grain boundaries in the magnetization behavior of non-oriented electrical steels and to find out how the interaction between magnetic domains and grain boundaries will affect the magnetization process. To this purpose, the grain boundary curvature was derived from 3D microstructure.

- To meticulously characterize fatigue crack paths, in relation to microstructural features and to find out how and by which mechanisms the cracks predominantly develop. To this purpose, an effort to explore the 3D nature of a propagating crack was initiated.

- To derive the grain boundary character distribution from a 3D EBSD data set and to find out whether the grain boundary planes carrying a specific type of misorientation are parallel to a specific crystallographic plane or not.

Addressing the above mentioned objectives, this dissertation is structured as follows:

Chapter 2 "An Overview of the EBSD Technique"

This chapter describes the fundamental basis of the EBSD technique, including the basic crystallography required for the application, the historical development of the technique, a brief explanation of the hardware setup of EBSD in the SEM chamber, and lastly, details about acquiring and analyzing EBSD data.

Chapter 3 "Three-Dimensional Characterization Techniques"

Different techniques for 3D characterization of the microstructures are explained in this chapter. Basic information about the techniques, their advantages, limitations and their applications are the subjects of this chapter. The techniques will be also compared with regard to their spatial resolution, width-of-field and speed of the measurement. Because serial sectioning technique is the technique of choice in this work, this technique is explained in more details with some examples of senior researchers.

Chapter 4 "General Experimental Procedures and Data Processing Techniques"

The fourth chapter of this thesis deals with the common experimental procedures employed to reconstruct the three-dimensional microstructure of materials used in chapters 5 to 7. The experimental procedures explained in this chapter include the sample preparation techniques and the details of the EBSD measurements in terms of microscope settings and data collecting parameters. Detailed explanation about data processing techniques and algorithms developed to reconstruct the 3D microstructure pertaining to section alignment and data segmentation as well as the method employed to visualize the 3D data are presented in this chapter.

Chapter 5 "Grain Boundary-Magnetic Domain Interaction: a 3D investigation"

The goal of this chapter is to employ the 3D investigation to study the interaction between magnetic domains in electrical steels and grain boundaries with a focus on grain boundary curvature derived from the 3D experiments. To this purpose, the effort was made to model/predict the magnetic behavior of non-oriented electrical

steels based on their chemical composition and the microstructural variables such as grain size, crystallographic orientation and grain boundary inclination. In view of the main subject of this thesis, the focus of this chapter is on the effect of the grain boundary curvature and the interaction between magnetic domains and grain boundaries.

Chapter 6 "Three-Dimensional EBSD Characterization of Fatigue Crack Morphology"

The emphasis of the sixth chapter is on analyzing the crack path evolution induced in Compacted Graphite Iron (CGI) during the process of Thermo-Mechanical Fatigue (TMF). TMF is believed to be the dominant process responsible for cracks developing in engine components [14]. The 3D EBSD technique is employed to meticulously characterize TMF crack paths, in relation to microstructural features and to find out how and by which mechanisms the cracks predominantly develop.

Chapter 7 "Deriving the Grain Boundary Character Distribution from 3D EBSD Data"

The emphasis of this chapter is to derive the grain boundary character distribution from a 3D data set. A general alignment algorithm is proposed to correct spatial misalignment as well as the misorientation between planar sections. In this chapter, the method is explained in detail to transform the grain boundary normal from the triangulated surface mesh to the crystal reference frame. Additionally, a procedure is proposed for the discretization of the grain boundary space to represent the five dimensional data set pertaining to the grain boundary character distribution.

Chapter 8 "Conclusions and Suggestions for Future Research"

1.3. References

1. Cahn, R.W. and P. Haasen, *Physical Metallurgy*. 1996: Elsevier Science.
2. Gault, B., et al., *Atom Probe Microscopy*. 2012: Springer.
3. Miller, M.K., *Atom Probe Tomography*, in *Handbook of Microscopy for Nanotechnology*, N. Yao and Z.L. Wang, Editors. 2005, Kluwer Academic Publisher. p. 227-246.
4. DeHoff, R.T., *Quantitative serial sectioning analysis: preview.* Journal of Microscopy, 1983. **131**: p. 259-263.
5. Zaefferer, S., S.I. Wright, and D. Raabe, *Three-dimensional orientation microscopy in a focused ion beam-scanning electron microscope: A new dimension of microstructure characterization.* Metallurgical and Materials Transactions a-Physical Metallurgy and Materials Science, 2008. **39A**(2): p. 374-389.
6. Uchic, M., et al., *An Automated Multi-Modal Serial Sectioning System for Characterization of Grain-Scale Microstructures in Engineering Materials*. Proceedings of the 1st International Conference on 3d Materials Science, ed. M. DeGraef, et al. 2012. 195-202.
7. Rohrer, G.S., et al., *Deriving grain boundary character distributions and relative grain boundary energies from three-dimensional EBSD data.* Materials Science and Technology, 2010. **26**(6): p. 661-669.
8. Saylor, D.M., A. Morawiec, and G.S. Rohrer, *The relative free energies of grain boundaries in magnesia as a function of five macroscopic parameters.* Acta Materialia, 2003. **51**(13): p. 3675-3686.
9. Rowenhorst, D.J. and P.W. Voorhees, *Measurement of Interfacial Evolution in Three Dimensions.* Annual Review of Materials Research, Vol 42, 2012. **42**: p. 105-124.
10. Dillon, S.J. and G.S. Rohrer, *Characterization of the Grain-Boundary Character and Energy Distributions of Yttria Using Automated Serial Sectioning and EBSD in the FIB.* Journal of the American Ceramic Society, 2009. **92**(7): p. 1580-1585.
11. Li, J., S.J. Dillon, and G.S. Rohrer, *Relative grain boundary area and energy distributions in nickel.* Acta Materialia, 2009. **57**(14): p. 4304-4311.
12. Khorashadizadeh, A., et al., *Five-Parameter Grain Boundary Analysis by 3D EBSD of an Ultra Fine Grained CuZr Alloy Processed by Equal Channel Angular Pressing.* Advanced Engineering Materials, 2011. **13**(4): p. 237-244.
13. Alkemper, J. and P.W. Voorhees, *Quantitative serial sectioning analysis.* Journal of Microscopy-Oxford, 2001. **201**: p. 388-394.
14. Hallstein, R., et al., *Thermal-mechanical fatigue behaviour of vermicular cast iron*. Progress in Mechanical Behaviour of Materials, ed. F. Ellying and J.W. Provan. 1999. 301-306.

Chapter 2. An Overview of the EBSD Technique

"With EBSD we look straight at the planes and directions of the crystal lattice, as if they are pulled out of the crystal towards our macroscopic world."

Leo Kestens

2.1. Introduction

The large majority of engineering materials of technological importance such as almost all common metals and many ceramics are polycrystalline. A polycrystalline material is composed of many crystallites of varying sizes and crystallographic orientations. When at least one dominant orientation exists, the polycrystalline is said to have a crystallographic texture or preferred orientation, otherwise it has a random distribution of orientations. It has been known since long that most of the physical and mechanical properties of the polycrystalline materials are highly dependent on the crystallographic orientation (texture) of the individual crystallites and their arrangement within the polycrystalline aggregate.

On the one hand, texture data can be collected using X-ray diffraction (XRD) or neutron diffraction for bulk texture measurements. On the other hand, transmission electron microscopy (TEM) and electron backscatter diffraction (EBSD) methods have been widely used to obtain the local crystallographic information (microtexture). In the transmission electron microscope (TEM), the techniques based on Kikuchi diffraction patterns offer a very good spatial resolution, a low sensitivity to strain, and relatively high precision orientation measurements. However, this technique suffers from complicated and very difficult sample preparation step and can be carried out only on a very small area that for most materials covers only a few numbers of crystals. The EBSD technique, on the other hand, due to the automated indexing of the diffraction patterns and relatively easier sample preparation can, in most cases, replace the more time-consuming and difficult TEM investigations [1].

The EBSD technique is now widely accepted as being the most powerful method for measuring microtexture. Its main strength and limitations are shortly summarized

below:

- High spatial resolution
- Good angular resolution (0.5 to 0.7°)
- Potential of covering wide sample areas
- Sample preparation can be time consuming and requires a level of expertise (although it is easier than TEM technique)
- Visualization of local texture and local crystal orientations
- Reasonable statistics because of full automation
- Potential of extending 2D to 3D observations
- Sample needs to be small enough to fit in a SEM on a 70° titled stage
- Speed of crystal orientations measurement
- Relative ease or low cost of attaching EBSD hardware to new or existing scanning electron microscopes

The EBSD technique is also known as backscatter Kikuchi diffraction (BKD), or electron backscatter pattern technique (EBSP), and one of the commercial name for this application is Orientation Imaging Microscopy (OIM^{TM}). The wide-spread application of the EBSD technique led to the fact that the term EBSD is now synonymous with both the scanning electron microscope (SEM) technique, and also as an accessory system that can be attached to a SEM [2].

This chapter provides the fundamental knowledge of the EBSD technique including the basic crystallography required for the application, the historical development of the technique, a brief explanation of the setup of a state-of-the-art EBSD system (hardware), and additionally some details about acquiring and analyzing the EBSD data.

2.2. Basic Crystallography

Because EBSD is based on electron *diffraction*, the method is basically applicable for crystalline materials, i.e. *"a solid composed of atoms arranged in a pattern periodic in three dimensions"* [3]. Crystallography, which is the science of examination of molecules, atoms and ions in crystalline structures, is a very broad subject. In this section only the basic requirements of crystallography which are necessary for a better understanding of EBSD patterns formation and further post-processing of EBSD data are presented.

2.2.1. Crystal Lattice

To represent a crystal lattice, it is more convenient to ignore the real atoms and replace them by points which directly relate to the position of the atoms (or molecules) in the crystal structure (cf. the boldface points in **Figure 2.1a**). These points may be regarded as the framework on which the actual crystal is built. They divide the space into small cells, which are identical in size, shape and orientation (cf. **Figure 2.1a**). Since all the cells of this lattice are identical, one of them is chosen as a unit cell, which is the simplest repeating cell in a crystal. The unit cell has the shape of a parallelepiped described by three vectors **a**, **b**, and **c** (cf. **Figure 2.1b**).

These three vectors are called crystallographic axes of the unit cell. The lengths of these three vectors ($\bar{a}$, $\bar{b}$ and $\bar{c}$) and the angles between them (α, β and γ) are called the lattice constants or lattice parameters of the unit cell [3, 4].

Although it seems that changing the lattice parameters produces various kinds of lattices, only seven types of unit cell are necessary to make all possible configurations of point lattices. These are called the crystal *systems* and are listed in **Table 2-1**. Different point lattices can easily be made by putting points at the vertices of each parallelepiped that represents the cell of one of the seven crystal systems.

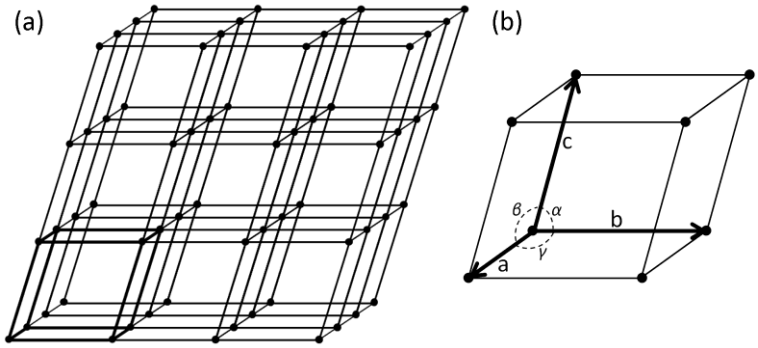

Figure 2.1 Schematic representation of (a) a point lattice, and (b) a unit cell [3].

In 1848 a French scientist, Auguste Bravais explained that placing an extra point in the geometric center or on the faces of the parallelepipeds representing the cells of the seven crystal systems, leads to 7 new lattices. Therefore, we have a total number of 14 lattice types in three dimensions which are called the *Bravais* lattices (cf. **Figure 2.2**). Seven out of these 14 lattices are simple or primitive (P) in which the lattice points are located only on the cell corners. The new lattices are as follow [3]:

- Body-centered (I): with one extra point at the center of the unit cell.
- Face-centered (F): with one extra point at the center of each of the faces of the unit cell.
- Base-centered (C): with one extra point at the center of one pair of opposite faces of the unit cell.

2.2.2. Crystal Symmetry

All crystal lattices exhibit various kinds of symmetry. It means that there are certain operations (i.e. reflection, rotation, inversion and rotation-inversion) when applied on the crystal lattice, it will bring it into coincidence with the original state. These operations are called symmetry operations. Reflection or mirror type symmetry exists when each point of the lattice coincides with an identical point by projecting it through a mirror plane and extending an equal distance beyond this plane [3]. This type of symmetry transfers a right handed object to a left handed object.

Table 2-1 Seven crystal systems and restriction on lattice parameters for each system [3, 4]

Crystal System	Restrictions of the Lattice Parameters	Bravais Lattice	Lattice Symbol
Triclinic	None	Simple	P
Monoclinic	$\alpha = \beta = 90°$	Simple Base-centered	P C
Orthorhombic	$\alpha = \beta = \gamma = 90°$	Simple Body-centered Base-centered Face-centered	P I C F
Tetragonal	$\alpha = \beta = \gamma = 90°$ $\bar{a} = \bar{b}$	Simple Body-centered	P I
Cubic	$\alpha = \beta = \gamma = 90°$ $\bar{a} = \bar{b} = \bar{c}$	Simple Body-centered Face-centered	P I F
Rhombohedral *	$\alpha = \beta = \gamma$ $\bar{a} = \bar{b} = \bar{c}$	Simple	P
Hexagonal	$\alpha = \beta = 90°$ $\gamma = 120°$ $\bar{a} = \bar{b}$	Simple	P

* Also known as Trigonal

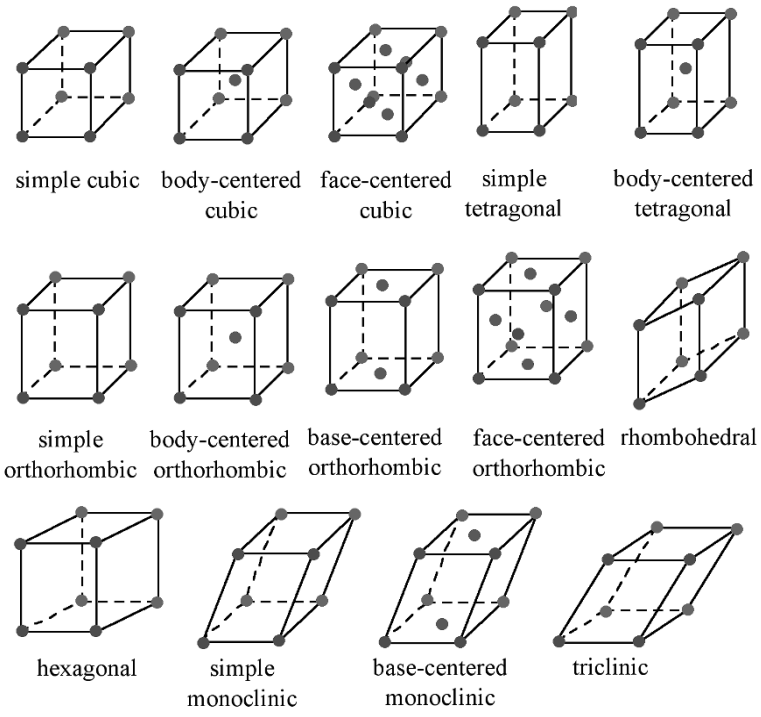

Figure 2.2 The fourteen Bravais lattices [3].

A crystal lattice has n-fold rotational symmetry if a rotation of 360°/n about an axis brings each point of the lattice back to an identical point. In other words, a n-fold rotation axis of symmetry is a line that will make the lattice coincide with itself n times when rotated 360° around this axis. The possible rotational symmetries are 1, 2, 3, 4, and 6-fold rotational symmetries. A 1-fold axis of rotation is obviously present in any irregular shaped body while a 5-fold rotation axis or one of higher degree than 6 is not possible because with such symmetry a unit cell cannot be copied without leaving open spaces. **Figure 2.3** shows 2-fold, 3-fold and 4-fold axis of symmetry in a cubic unit cell. Square, triangle and ellipse shapes in this figure designate 4-fold, 3-fold and 2-fold rotational symmetry, respectively. A 4-fold symmetry operator brings A1 to A2, while a 3-fold symmetry operator brings A1 to A3 and by a 2-fold symmetry operator A1 turns to A4 [3].

A body has an inversion centre if for every point in it there is an identical point equidistant from the centre but on opposite side [5-7]. These symmetry elements are summarized in **Table 2-2** and it can be seen that there are in total ten symmetry elements for a crystal [7].

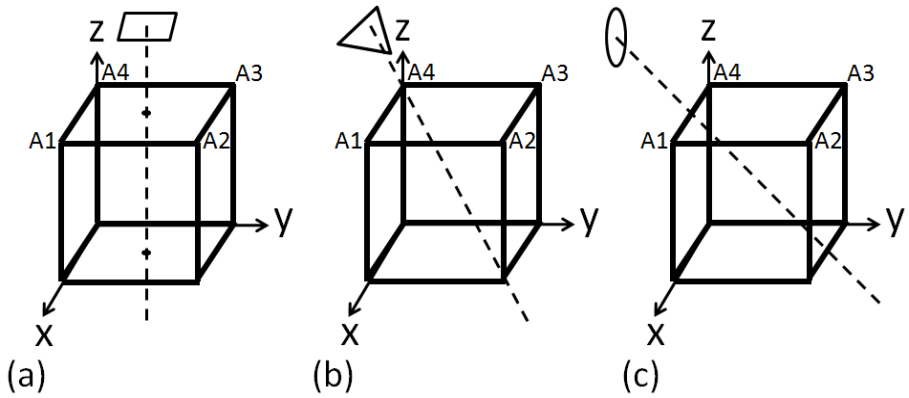

Figure 2.3 Schematic representation of (a) four-fold, (b) three-fold and (c) two-fold rotational symmetry axes [7].

The collection of symmetry elements at any point of the lattice is termed as the point “group”. A group of symmetry elements includes all elements so that the combination of any 2 of them results in an element that is already in the group [8]. It can be analyzed that from a large number of possible combination of the ten symmetry elements (reflection, inversion, rotation, and rotation-inversion); there are only 32 possible combinations of one or more of them. In other words, there exist only 32 point groups of symmetry. These 32 point groups can be re-grouped into seven different sets and the groups in each set have one common symmetry element. These seven sets are the seven crystal systems listed in **Table 2-1**. It means that, there is one common symmetry element between the point groups belonging to each crystal system. The common symmetry element possessed by

each crystal system is presented in **Table 2-3** [7].

The most convenient way to apply the symmetry elements is by expressing them as symmetry operators in the form of matrices. **Table 2-4** represents the symmetry operators of the rotation group for cubic crystals in matrix form. These 24 symmetry operators consist of 9 four-fold rotation (90°, 180°, 270° rotation about 3 axes), 8 three-fold rotation (120°, 240° rotation about 4 axes) and 6 two-fold rotation (180° rotation about 6 axes) plus the identity matrix. The identity matrix is always a member of the symmetry group.

Table 2-2 All symmetry elements and their numbers in a crystal [7]

Symmetry operation	Number
Reflection	1
Inversion	1
Rotation	5
Rotation-Inversion	3
Total number of symmetry elements = 10	

Table 2-3 Seven crystal systems and their common point symmetry elements [7]

Crystal system	Common essential symmetry
Triclinic	None (Identity symmetry)
Monoclinic	One 2-fold rotation
Orthorhombic	Three perpendicular 2-fold rotation
Tetragonal	One 4-fold rotation
Cubic	Four 3-fold rotation
Rhombohedral	One 3-fold rotation
Hexagonal	One 6-fold rotation

Table 2-4 Symmetry operators of rotations group for cubic crystal system [8]

1	0	0	0	0	1	0	1	0	0	-1	0	0	-1	0
0	1	0	1	0	0	0	0	1	0	0	1	0	0	-1
0	0	1	0	1	0	1	0	0	-1	0	0	1	0	0
0	1	0	0	0	-1	0	0	-1	0	0	1	-1	0	0
0	0	-1	1	0	0	-1	0	0	-1	0	0	0	1	0
-1	0	0	0	-1	0	0	1	0	0	-1	0	0	0	-1
-1	0	0	1	0	0	0	0	-1	0	0	1	0	0	1
0	-1	0	0	-1	0	0	-1	0	0	-1	0	0	1	0
0	0	1	0	0	-1	-1	0	0	0	1	0	-1	0	0
0	0	-1	-1	0	0	1	0	0	1	0	0	-1	0	0
0	1	0	0	0	-1	0	0	-1	0	0	1	0	0	1
1	0	0	0	-1	0	0	1	0	0	-1	0	0	1	0
0	-1	0	0	1	0	0	1	0	0	-1	0			
-1	0	0	-1	0	0	1	0	0	1	0	0			
0	0	-1	0	0	1	0	0	-1	0	0	1			

2.2.3. Lattice Directions and Planes

When studying crystallographic related objects it is often necessary to describe particular lattice planes or directions. Conventionally, three integers or indices are used to specify directions and planes. The origin of the coordinate system is located at one corner of the unit cell, and the crystallographic axes (i.e. the edges of the unit cell) are the three axes of the coordinate system. Obviously, these three axes are not necessarily perpendicular.

A lattice direction can be described as a vector between two lattice points. In order to determine the direction of any line in the lattice a vector parallel to the line is positioned in such a way that it passes through the origin of the coordinate system. The vector is projected on each of the three axes and the length of the vector projection on each axis is determined in term of the unit cell parameters and are multiplied or divided by a common factor to be reduced to the smallest integer values. By convention, the three indices representing the lattice direction are presented between square brackets, e.g. [uvw]. The minus sign is presented by a bar over the corresponding index. Directions which – from the symmetric point of view – are equivalent are called directions of a form. All directions which belong to the same form are presented with the indices of one of them between angular brackets (e.g. <uvw>). For example, [110], [10$\bar{1}$] and [0$\bar{1}$ $\bar{1}$] are directions with the same form and all of them together may be presented with <110> [9]. Examples of lattice direction indices are presented in **Figure 2.4**.

To represent the orientations of crystallographic planes again the unit cell is the basis, whereby the three-axis coordinate system and three indices are used to determine the orientations of the plane. If the crystallographic plane intersects with the three axes, then the length of the planar intercept for each axis is determined in terms of the lattice parameters. Two points need to be taken into account. First, if the plane passes through the origin of the coordinate system, either another parallel plane must be considered by an appropriate translation or the origin must be moved to a new position at another corner of the unit cell. Second, if a plane is parallel to an axis, then the length of the planar intercept for that axis is infinity.

The inverses of the planar intercepts for all axes are taken and changed to the set of smallest integers by multiplication/division by a common factor. These indices are presented within parentheses, e.g. (hkl) and are called Miller indices (introduced in 1839 by the British mineralogist and crystallographer William Hallowes Miller). Again the minus sign is presented by a bar over the corresponding index. In cubic systems the planes and directions with the same indices are perpendicular to one another. Similar to crystallographic directions, all planes which are crystallographically equivalent belong to the same “family” and family is designated by indices that are presented in braces, e.g. {hkl}. For example, in cubic crystals the (111), ($\bar{1}$ 11), ($\bar{1}$ $\bar{1}$ 1), ($\bar{1}$ $\bar{1}$ $\bar{1}$), ($\bar{1}$ 1$\bar{1}$) planes all belong to the {111} family [9]. Examples of crystallographic plane indices are presented in **Figure 2.5**. It is worth to remember that in the cubic crystal system the direction [abc] is always perpendicular to the plane with the same indices, i.e. the plane (abc).

There is a problem for crystals with hexagonal lattice because some crystallographic equivalent directions will not have the same set of direction and plane indices. This problem can be solved by considering a four-axis coordinate system (or Miller–Bravais system) in which there are three coplanar axes with 120 ° angles to one another and the fourth axis perpendicular to the other three axes. Further explanation about direction and plane indices in the hexagonal lattice is beyond the scope of this thesis and is referred to the references [3, 9].

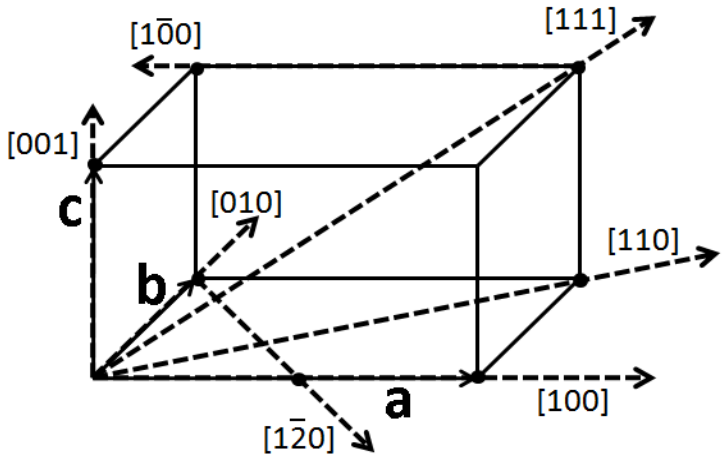

Figure 2.4 Indices of some crystallographic directions.

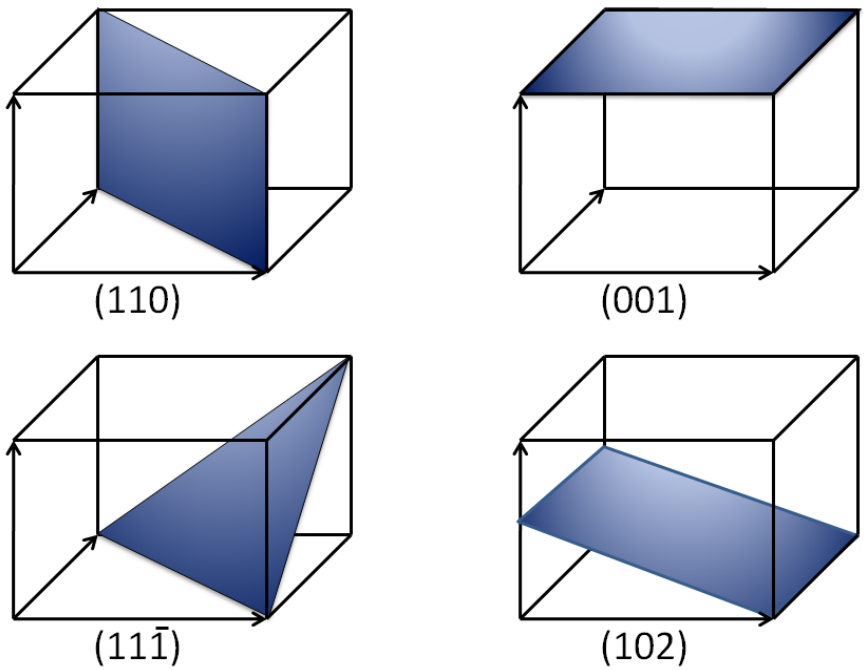

Figure 2.5 Miller indices of some examples of crystallographic planes.

2.2.4. Structure of Metals

All of the above mentioned topics were about geometrical arrangement of atoms in a unit cell and nothing about actual crystals. The basic principle of a crystal structure is that atoms in a real crystal are located either in the place of the points in a Bravais lattice or in some fixed positions related to those points. The simplest crystals are those which are made by replacing one type of atom on the point's positions of a Bravais lattice. Although not all crystals are composed of only one type of atom, many conventional metals for structural application crystallize in this simple fashion and present two well-known crystal structures, i.e. the Face-Centered Cubic (FCC) and Body-Centered Cubic (BCC) lattices.

FCC is the crystal structure of many metals (copper, aluminum, silver, nickel, and γ-iron) which has a unit cell with cubic geometry. Atoms are located at each corner of the cube and at the centers of all the cube faces and they touch each other along the diagonals of the cube faces. For the FCC crystal structure, one atom at the corner of the cube is shared among eight unit cells, and one atom at the center of a face is shared with two unit cell (cf. **Figure 2.6a**). It means that there are totally 4 atoms in each unit cell ($8\times(1/8)+6\times(1/2)=4$). FCC structures have the highest atomic packing factor (0.74) in comparison with other crystal structures. The atomic packing factor is the volume fraction of atoms in a unit cell.

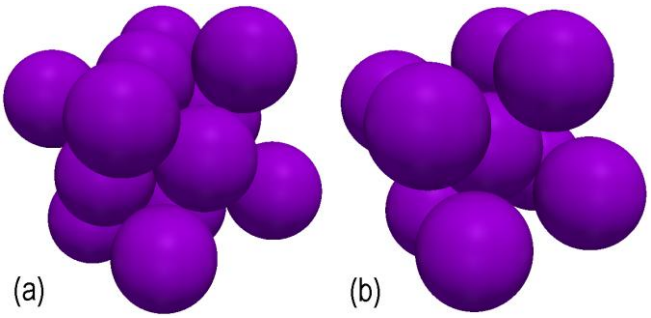

Figure 2.6 Common crystal structures in metals, (a) Face-Centered Cubic (FCC), and (b) Body-Centered Cubic (BCC).

BCC is another common crystal structure in metals (e.g. α-iron, molybdenum, tungsten). In BCC structures eight atoms are located at each corner and one single atom at the center of the cube in a way that the atom at the center and the atoms at the corners touch one another along the cube body diagonals. There are totally 2 atoms in each BCC unit cell, one at the center and the equivalent of one atom at the eight corners. The atomic packing factor for BCC crystals is less than the one for FCC crystals and is equal to 0.68 [9].

The next most common crystal structure in metals, which is more complex than the above mentioned structures, is Hexagonal Close-Packed (HCP). Metals with HCP crystal structure include cadmium, magnesium, titanium, zirconium and zinc. HCP is a simple hexagonal structure (as illustrated in **Figure 2.2**) in which the top and bottom faces of the unit cell consist of six atoms that form regular hexagons and surround a single atom in the center. But there is another plane with three

additional atoms between the top and the bottom planes (cf. **Figure 2.7**). Together with FCC, also in the HCP lattice atoms can be packed together in the space with the highest possible density and keeping the periodic arrangement. Similar to FCC, the HCP crystal structure has an atomic packing factor of 0.74 [3].

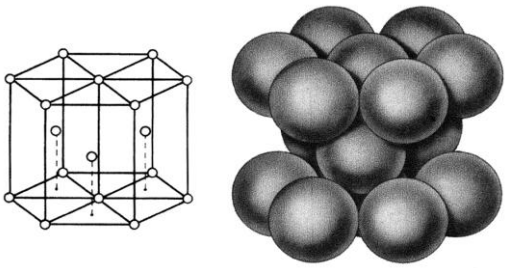

Figure 2.7 Schematic representation of the Hexagonal Close-Packed (HCP) structure [3].

2.2.5. Stereographic Projection

So far, the crystallographic planes and directions were represented by a perspective drawing or Miller indices. Stereographic projection is a graphical method for representing planes and direction of a crystal and calculating the angles between them.

Although the first application of stereographic projection in crystallography was the work of F. E. Neumann and after him W. H. Miller, the stereographic projection is a very ancient geometrical technique originated in the second century A.D. which was used as a method of representing the stars [10].

As it was explained before, for cubic crystals the Miller indices of a plane are the same as the indices of the normal to that plane; therefore, all the planes in a crystal can be represented by the plane normals originating from a reference point. Now if a sphere is considered with its center located at that reference point, the plane normals will intersect with the surface of the sphere. The points of these intersections are called poles. **Figure 2.8a** shows the {100} poles of a cubic crystal. The angle between two planes (α) is obviously equal to the angle between their normals (cf. **Figure 2.8b**) and can be measured on the surface of the sphere along the great circle connecting two poles (P1 and P2) [3].

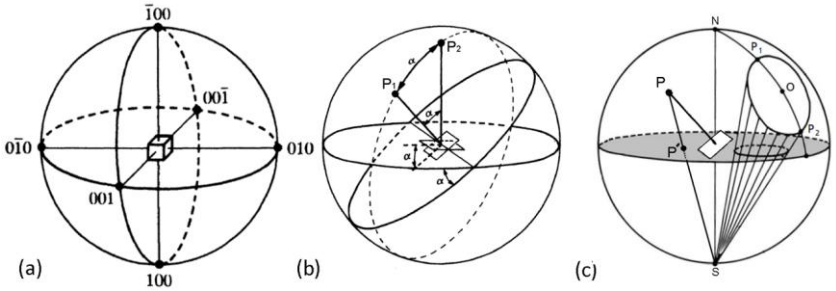

Figure 2.8 (a) {100} poles of a cubic crystal, (b) angle between two planes and (c) the stereographic projection of a pole [3].

The next step is to present this three-dimensional information in two dimensions by projecting them. To this purpose, in crystallography, the stereographic projection is preferred because after projection it preserves the angular relationship between points although the areas are distorted. Alternatively, geographers prefer to use equal area projection so that the countries with equal areas will be represented by equal areas on the map. In the stereographic projection, the intersections of the plane normals with the surface of the sphere which are in the North Pole are projected to the South Pole (and vice versa) as shown in **Figure 2.8c**. The intersections of the projected lines to the South Pole with the equatorial plane (point P' in **Figure 2.8c**) are considered as the stereographic projection of the plane normals. In a stereographic projection the equal angles are represented by larger distances as we move out from the centre; however, it has one very important geometrical advantage and that is that the circles on the surface of the sphere appear as circles, not ellipses, in the plane of projection (cf. **Figure 2.8c**) [10].

The stereographic projection map (the stereogram) of poles of different crystallographic planes in a cubic crystal system is shown in **Figure 2.9a**. To manipulate the stereographic projected data and for example to calculate the angle between two poles a stereographic graph paper is needed. To this purpose, a net developed by the Russian mineralogist George Viktorovich Wulff (cf. **Figure 2.9b**) is used. Measuring the angle between two poles in the Wulff net is possible; if and only if, they are both located on one of the great circles. Therefore, in order to measure the angle between two poles, the Wulff net is rotatable (around a pin in the centre) [10]. In addition to measuring the angle between poles, the stereographic projection has more applications as it allows for:

- Representation of point group symmetry
- Representation of orientation relationships
- Representation of preferred orientations (texture)

Further details about stereographic projections and manipulating the Wulff net can be found in the reference books [3, 10].

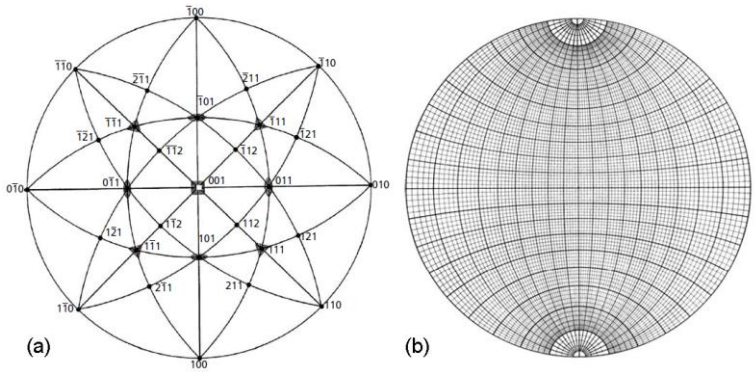

Figure 2.9 (a) Stereographic projection map showing the poles of different planes in a cubic crystal, (b) the Wulff net representing the stereographic projections of a set of large and small circles [10].

2.2.6. Representation of Orientations

By simple definition, the crystallographic orientation is the coordinate relation between the axes of the crystal lattice and an external reference coordinate system. This reference coordinate system is usually defined by the sample geometry. For example, for a rolled sheet metal, the reference coordinate system can be made up of the rolling, transverse and normal directions (RD, TD and ND, respectively) (cf. **Figure 2.10**).

Generally, the relation between two coordinate systems can be represented in various ways, which is the topic of this section. One simple way of specifying a single orientation is by the Miller indices of two directions: the normal to the crystal plane that is parallel to the x,y plane of the sample reference system and the crystal direction in that plane, which is parallel to the x-axis of the sample reference system. Hence, in rolled sheet metals orientation can be specified by {hkl}<uvw>, which means that the {hkl} plane of the orientation is parallel to the rolling plane and the <uvw> direction is parallel to the rolling direction. For example the {110}<100> orientation (known as the Goss orientation) in which the {110} plane is parallel to the rolling plane and the <100> is aligned with the rolling direction, cf. **Figure 2.10**.

Another method consists of three rotations that will bring the crystal coordinate system (K_c) in coincidence with the sample coordinate system (K_s). Considering **Figure 2.11** these three rotations include:

φ_1: The first rotation about Z_S and brings X_S into the X_C-Y_C plane.
Φ: The second rotation is about the new X_S axis (i.e. X'_S) and brings Z_S in coincidence with Z_C.
φ_2: The last rotation is about the new Z_S axis (i.e. Z'_S) and brings all the axes of sample reference system in coincidence with the axes of the crystal reference system [11].

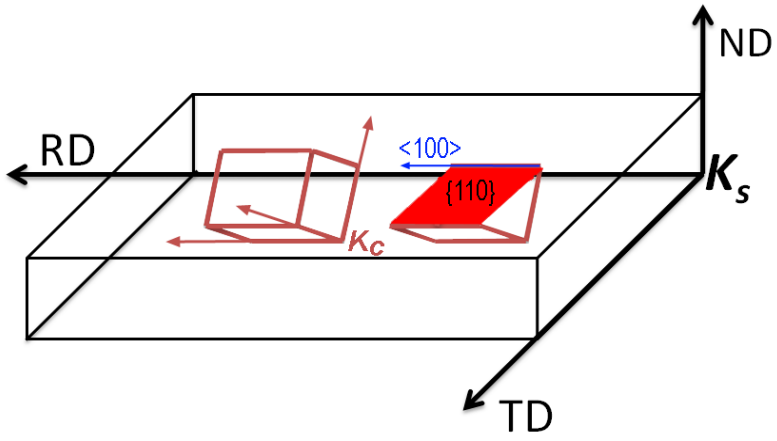

Figure 2.10 Schematic representation of the orientation of a cubic crystal with respect to the sample. K_s and K_c are the sample and crystal reference systems, respectively. RD, ND and TD are the abbreviations for rolling direction, normal direction and transverse direction, respectively.

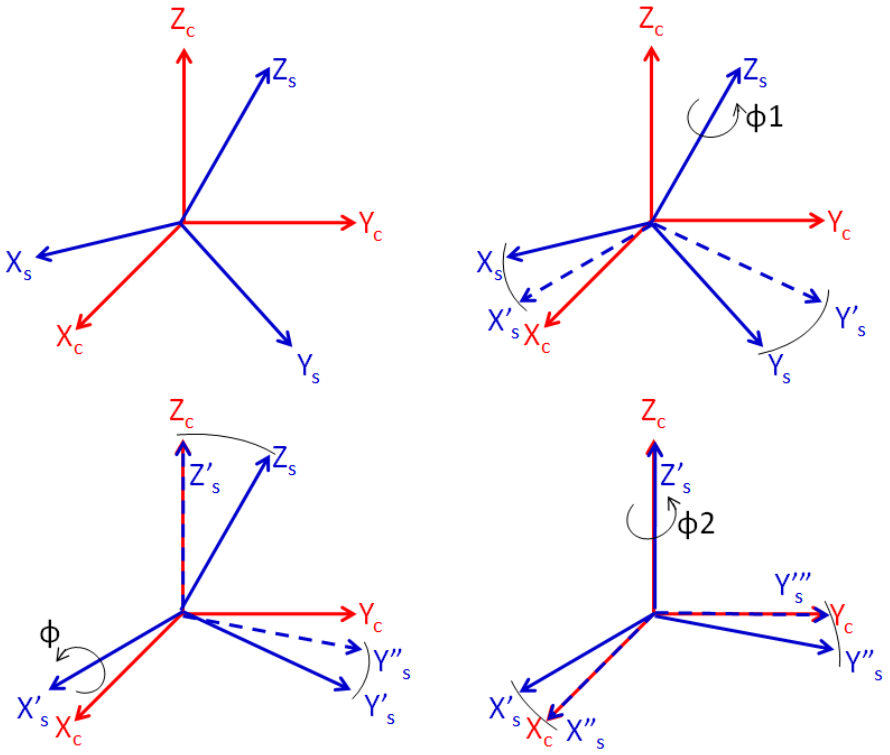

Figure 2.11 Representation of the rotations corresponding to the Euler angles [11].

φ_1, Φ, φ_2 represent a set of Euler angles, according to Bunge notation (Hans Joachim Bunge, German crystallographer, 1929-2004) and they are commonly used to represent a crystal orientation. For instance the Euler angles of the Goss orientation {110}<100> shown in **Figure 2.10** are (0°, 45°, 90°). Euler angles can alterantively be expressed according to the Roe notation (ψ, Θ, Φ) and the Kocks notations (Φ, Θ, φ). The relationship between these angles is as follows [8]:

- Bunge notation (φ_1, Φ, φ_2)
- Roe notations (ψ, Θ, Φ) = (φ_1-90°, Φ, 90°- φ_2)
- Kocks Notations (Φ, Θ, ϕ) = (φ_1-90°, Φ, 90°+ φ_2)

Another way of representing the relation between crystal and sample reference system, is by an axis and an angle of rotation about that axis, which together produce an axis/angle pair, cf. **Figure 2.12**. According to this method, one considers one axis and one angle of rotation around that axis that will bring the sample coordinate system into coincidence with the crystal coordinate system [8, 12]. The axis/angle pair method is very similar to another method which is called the Rodrigues vector in which instead of an axis (d) a vector (R) is associated of this rotation. The direction of this vector is parallel to the rotation axis, whereas its magnitude is equal to the tangent of the rotation angle (ω) divided by two (cf. **Equation 2.1**)[13].

$$R = d.tan\frac{\omega}{2} \qquad 2.1$$

The Rodrigues vector is represented in Rodrigues-Frank (R-F) space, which is defined by the three orthogonal axes R1, R2, R3. All possible angle/axis combinations are found in R-F space. Because of symmetry equivalents, there are 24 possible R vectors (for cubic symmetry) and in practice the vector with the smallest rotation angle is used. All such R vectors lie close to the origin of R-F space and they represent a fundamental zone, which has the shape of a truncated cube (cf. **Figure 2.13**). The shape of the fundamental zone is controlled by the crystal symmetry and the sample symmetry [14, 15].

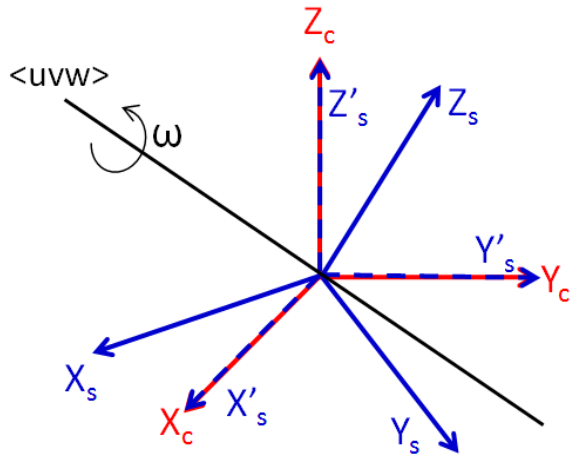

Figure 2.12 Schematic representation of an axis/angle pair connection between two reference frames [11].

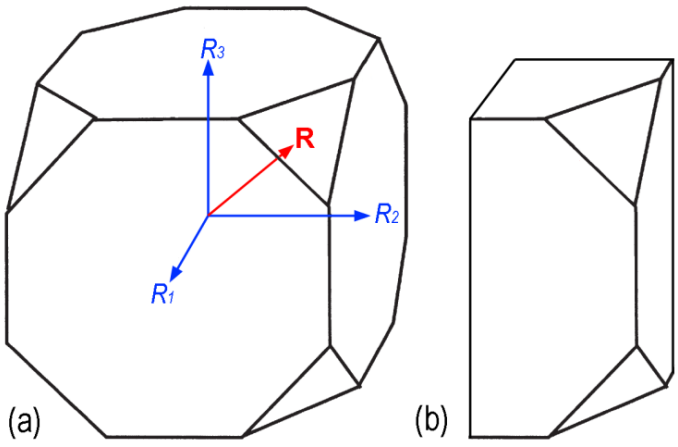

Figure 2.13 The fundamental zone of the Rodrigues-Frank space for cubic crystal symmetry, (a) no sample symmetry, (b) with orthorhombic sample symmetry [14, 15].

The advantages of this method for representation of an orientation are:

- Each orientation appears only once in the fundamental zone.
- The volume element of R-F space is homogeneous.

On the other hand, in comparison with R-F space, the fundamental zone of the Euler space is curved for cubic crystal symmetry (cf. **Figure 2.14**) [12]. For this reason, a convenient with straight boundaries defined by $0 \leq \phi_1 \leq \pi/2$, $0 \leq \Phi \leq \pi/2$, and $0 \leq \phi_2 \leq \pi/2$ is often used to represent the Euler angles. Although this region contains three points for every orientation, the advantage of a two dimensional presentation by a series of parallel sections has turned it to a routine method for orientation representation [16]. **Figure 2.15** shows the locations of the Goss orientation ({110} <001>) in the two dimensional sections of the Euler space.

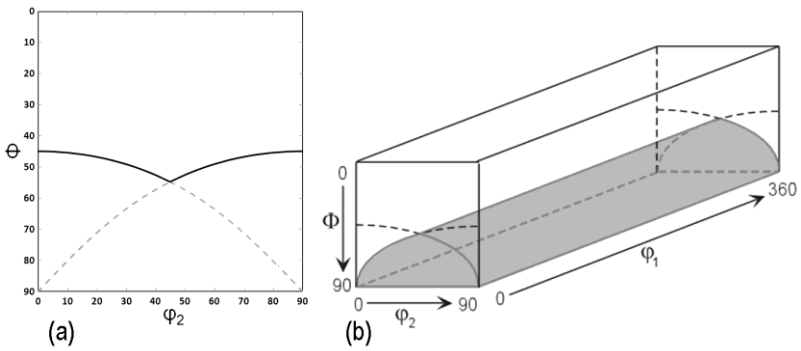

Figure 2.14 The fundamental zone for the cubic symmetry in (a) the φ_1=0° section [12], and (b) the entire Euler space [11].

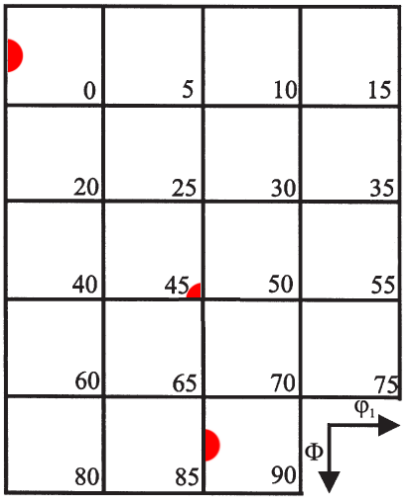

Figure 2.15 The locations of the Goss orientation ({110} <001>) in the two dimensional sections of the Euler space. The number in each section shows the φ_2 value of that section [17].

In linear algebra it is customary to express transformations form the sample reference system to the crystal reference system by an orientation matrix. The orientation matrices on the basis of Euler angles and axis/angle pair are represented by **Equation 2.2** and **Equation 2.3**, respectively.

$$g = \begin{bmatrix} cos\,\varphi_1 cos\,\varphi_2 - sin\,\varphi_1 sin\,\varphi_2 cos\,\Phi & sin\,\varphi_1 cos\,\varphi_2 + cos\,\varphi_1 sin\,\varphi_2 cos\,\Phi & sin\,\varphi_2 sin\,\Phi \\ -cos\,\varphi_1 sin\,\varphi_2 - sin\,\varphi_1 cos\,\varphi_2 cos\,\Phi & -sin\,\varphi_1 sin\,\varphi_2 + cos\,\varphi_1 cos\,\varphi_2 cos\,\Phi & cos\,\varphi_2 sin\,\Phi \\ sin\,\varphi_1 sin\,\Phi & -cos\,\varphi_1 sin\,\Phi & cos\,\Phi \end{bmatrix} \qquad 2.2$$

$$g = \begin{bmatrix} (1-d_1^2)\cos\omega + d_1^2 & d_1 d_2(1-\cos\omega) + d_3 \sin\omega & d_1 d_3(1-\cos\omega) - d_2 \sin\omega \\ d_1 d_2(1-\cos\omega) - d_3 \sin\omega & (1-d_2^2)\cos\omega + d_2^2 & d_2 d_3(1-\cos\omega) + d_1 \sin\omega \\ d_1 d_3(1-\cos\omega) + d_2 \sin\omega & d_2 d_3(1-\cos\omega) - d_1 \sin\omega & (1-d_3^2)\cos\omega + d_3^2 \end{bmatrix} \qquad 2.3$$

ω is the rotation angle about the axis d=[d_1, d_2, d_3] (with normalized components)

In these matrices, the rows represent the coordinates of crystal axes with respect to the sample axes, whereas the columns represent the base vectors of the sample reference system (i.e. RD, TD and ND) with respect to the crystal reference system. Such a transformation matrix describes a transformation from the sample reference system to the crystal reference system [12].

A crystallographic orientation can also be graphically represented on a stereographic projection, whereby a pole figures is used to visualize the distribution of crystallographic poles in a two-dimensional plane. A pole figure is a stereographic projection which shows the distribution of the poles (the normals to the lattice planes) of particular crystallographic planes. To construct a pole figure, the sample is considered at the center of a unit sphere (cf. **Figure 2.16a**). The sample RD and TD directions coincide with the equatorial plane of the stereographic sphere, whereas the sample ND direction coincides with the North-South direction of that sphere. For an arbitrary crystal in the sample, the intersections of the normals to the planes {hkl} -which belong to the same family- with the surface of the sphere, are specified (cf. **Figure 2.16b**). The pole figure represents the distribution of the stereographic projection of these points (cf. **Figure 2.16c**) for many different crystals in the sample [18].

In order to relate the pole distributions to the sample reference system, a pole figure must have some reference directions. Traditionally these directions refer to the forming process, e.g. the rolling direction in rolled sheets (ND, RD and TD in **Figure 2.16**). This has the benefit of revealing any sample symmetry in the resulting pole figures. Sample symmetry is imposed during processing of the material. A rolled sheet, for example, generally exhibits orthotropic sample symmetry. It means that a statistically identical pole figure can be reproduced from any one of the four quadrants [16].

Whereas a pole figure shows the distribution of particular crystallographic pole with respect to the sample directions, alternatively, the orientation of the sample coordinate system can be projected into the crystal coordinate system. This representation is called the *inverse* pole figure. The inverse pole figure is mainly useful for the samples in which the processing history strongly identifies a single direction, e.g. wire drawing or extrusion processes, which require the specification

of only a single axis. The forming processes in which all three axes are important (i.e. rolling) can also be described by an inverse pole figure but in this case separate plots are used for each of the principal strain axes ND, RD and TD. Constructing an inverse pole figure is carried out with a procedure very similar to that of a pole figure. The only difference is that instead of projecting a crystallographic pole, the vector parallel to a given sample direction is projected on the stereographic plane [8, 16].

It is worth to mention that the representation of an orientation with a pole figure or an inverse pole figure is not complete and they do not uniquely identify the orientation of a specific crystal, meaning that only the orientations of particular crystallographic poles or directions can be indicated by pole figures or inverse pole figures. Even in this case, the poles of different orientations may overlap and the intensity of an individual pole in a pole figure cannot clearly be assigned to a specific orientation.

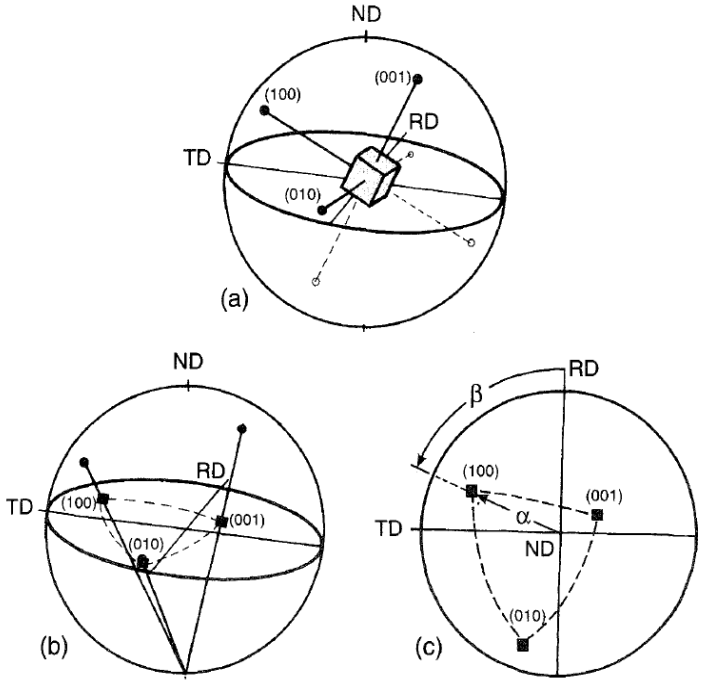

Figure 2.16 Representation of the (100) pole figure for a cubic crystal, (a) the crystal is located at the center of a unit sphere, (b) stereographic projection of the (100) poles, (c) (100) pole figure. The angles α and β are used to describe the position of a given pole [18].

To overcome these ambiguities, the crystallographic texture of a polycrystalline material is usually described in terms of its orientation distribution function (ODF). The ODF presents the probability of finding a specific volume element dV within a crystalline material of orientation g±dg. This kind of distribution is actually more useful for the analysis of texture information than discrete orientation measurements.

In the general case, a pole figure can be obtained by integrating the orientation distribution function, f(g), along a path (Γ) in Euler space corresponding to a 2π rotation of a crystal about its (hkl) pole [8, 12].

$$P_{(hkl)}(y) = \frac{1}{2\pi} \cdot \int_0^{2\pi} f(g)\, d\Gamma \qquad \text{where } g=\{\varphi_1, \Phi, \varphi_2\} \qquad 2.4$$

An important problem in texture analysis is to solve **equation 2.4** in a reverse way, i.e. to calculate the ODF from the pole figure data. This is called *pole figure inversion* and because of the missing crystallographic information in a pole figure, one pole figure is not enough to determine an ODF and thus additional pole figures are needed. Furthermore, it is not possible to solve it analytically and several mathematical approaches have been proposed for pole figure inversion solution. Here, only the most common method based on harmonic series expansion will be briefly introduced, but for a more detailed account the reader is referred to the text by Bunge [12].

The series expansion method is based on the assumption that both the measured pole figures and the ODF can be expressed by a series expansion in terms of appropriate mathematical functions. This method is called harmonic method because the functions used in a spherical coordinate system are the spherical harmonic functions. According to this method, the ODF, f(g), can be developed in a series of generalized spherical harmonic functions:

$$f(g) = \sum_{l=0}^{\infty} \sum_{m=-l}^{+l} \sum_{n=-l}^{+l} C_l^{mn} T_l^{mn}(g) \qquad 2.5$$

Where g can be expressed by means of Euler angles. T_l^{mn} are the spherical harmonic functions and C_l^{mn} are the series expansion coefficients.

The pole figures can also be expanded in a series of spherical harmonic functions:

$$P(\alpha, \beta) = \sum_{l=0}^{l_{max}} \sum_{n=-l}^{l} F_l^n \dot{K}_l^n(\alpha, \beta) \qquad 2.6$$

Where the F are the pole figure coefficients and the K are the symmetrized spherical harmonic functions. It should be mentioned that as a pole figure is characterized by two angles (α, β), an expansion in symmetrized spherical harmonic functions is sufficient. The dot over the harmonic function denotes its symmetrization.

The pole figures series expansion coefficients are related to the C_l^{mn} coefficients through:

$$F_l^n = \frac{4\pi}{2l+1} \cdot \sum_{m=-l}^{l} C_l^{mn} \dot{K}_l^{*m}(\xi, \eta) \qquad 2.7$$

Where ξ and η are the polar coordinates of a pole in the crystal coordinate system. The star over the harmonic function denotes complex conjugate. This equation forms a system of linear equations which can be solved to derive the C_l^{mn} coefficients.

So far the construction of the orientation distribution function from pole figure data was discussed. It should be noted that even when the Euler angles are directly available, construction of a continuous function which represents the orientation distribution has some benefits. Traditionally, diffraction techniques lacked the spatial resolution to measure the orientations of individual crystals; and an ODF makes it possible to estimate the volume fraction of a particular orientation within the material. To make such a continuous function, a Gaussian type distribution is attributed to each single orientation in the Euler angle space. For N individual orientations the ODF is determined by superposition of the corresponding N Gauss-peaks. More detailed explanations and equations can be found in the text by Bunge and Randle [12, 18].

The results of such an orientation distribution function is presented in **Figure 2.17**, where a continuous ODF (cf. **Figure 2.17b** and **c**) is constructed from a discrete distribution of single orientations with less than 3° angular distance with Goss orientation (cf. **Figure 2.17a**). A harmonic series expansion with series rank of 16 and Gaussian half-width of 5° was used determine this ODF. **Figure 2.17d** shows the recalculated pole figure from the generated ODF after applying orthorhombic sample symmetry.

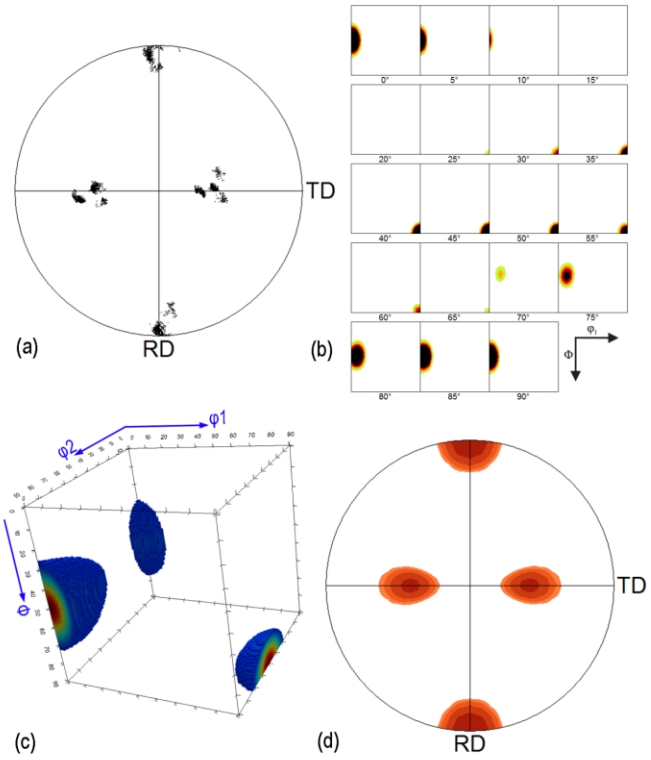

Figure 2.17 (a) Discrete (100) pole figure of a set of orientations within 3° angular distance to the Goss orientation, (b) 2D sections of the ODF represented in Euler space, (d) the 3D view of the ODF, and (d) the recalculated (100) pole figure with imposed orthorhombic sample symmetry.

2.3. History of EBSD

The first observation of electron diffraction was reported in 1928 by Shoji Nishikawa and Seishi Kikuchi [19]. They directed a monochromatic beam of 50 KeV from a gas discharge on a cleavage face of calcite at a grazing incidence of 6°. The diffraction patterns were recorded on photographic plates placed 6.4 cm behind the crystal, normal to the primary beam. The pattern consisted of a number of bands of different widths and also many black and white lines (cf. **Figure 2.18**).

> *"Usually a black line makes a pair with a white line parallel to it. When the distance between the lines becomes small, the pair looks like a band. In fact, one edge of a band is bounded by a black line and the other edge by a white. There is no doubt that the band is nothing but a pair of lines separated by a short distance."*

According to Nishikawa and Kikuchi [19], the intersection of each crystallographic plane with the photographic plate is between the black and white lines of a pair. These lines are shown in **Figure 2.18** by the lines prolonged outside the picture (the indices of the planes are given in the square brackets). Each pair of black and while lines (or each band) is used to calculate these indices. The authors called this new type of pattern "*pattern of the fourth type*". They have later been named backscatter Kikuchi patterns (BKP).

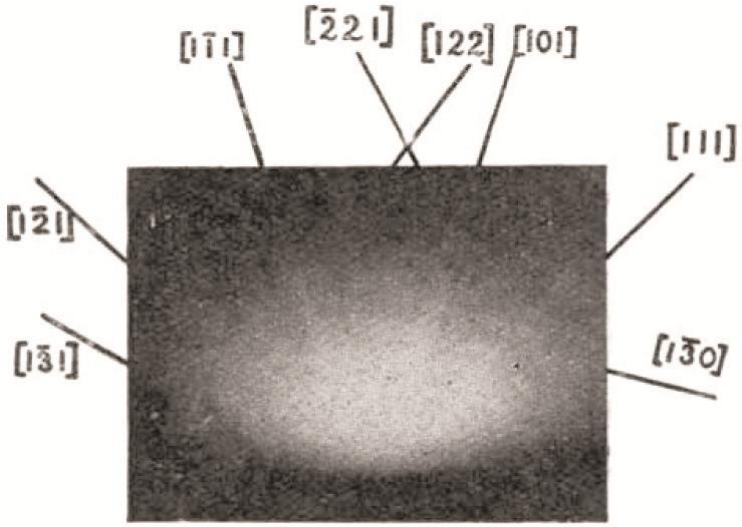

Figure 2.18 Diffraction pattern from calcite cleavage [19].

The reason of the low quality of the first Kikuchi pattern may be the contamination of the sample due to the poor vacuum facilities at that time. Besides on calcite, Nishikawa and Kikuchi collected similar patterns from cleavage faces of mica, topaz and quartz. They claimed that this new technique would be more useful than the transmission method due to its possibility of extensive application on many crystals.

Since then many examples of these types of Kikuchi pattern have been published and the quality of the patterns was remarkably improved. However, the most often quoted paper describing the above mentioned diffraction phenomena was published in 1954 by Alam, Blackman and Pashley [20], in a paper entitled "*High-Angle Kikuchi Patterns*". The authors recorded the patterns directly on photographic film using a purpose-built vacuum chamber. A cylindrical chamber and camera (cf. **Figure 2.19a**) were used to study the Kikuchi patterns obtained by reflection (*reflexion* is the term used by the authors) of electrons, of energy 6 to 50 keV, from the cleavage surfaces of crystals with the sodium chloride structure (cf. **Figure 2.19b**). Angles of scattering ranging from 0 to 164° were covered. The relative intensity of the pattern at different scattering angles was measured using a photographic technique.

45 years after the first observation of backscatter Kikuchi patterns, Venables and Harland (1973) [21] described how these patterns can be obtained in the Scanning Electron Microscope (SEM) and be used to collect the crystallographic information from the specimen. The patterns were recorded on a fluorescent phosphor screen placed in the specimen chamber and viewed by a TV camera attached to the SEM. The patterns were then photographed directly from the screen on which the video signal was displayed and analyzed on the basis of this photograph. The terms "EBSP" or "EBSD" as acronyms for "Electron BackScattering Pattern" or "Electron BackScattering Diffraction" which were proposed by Venables, have been universally adopted today to refer to the Kikuchi patterns recorded in an EBSD system.

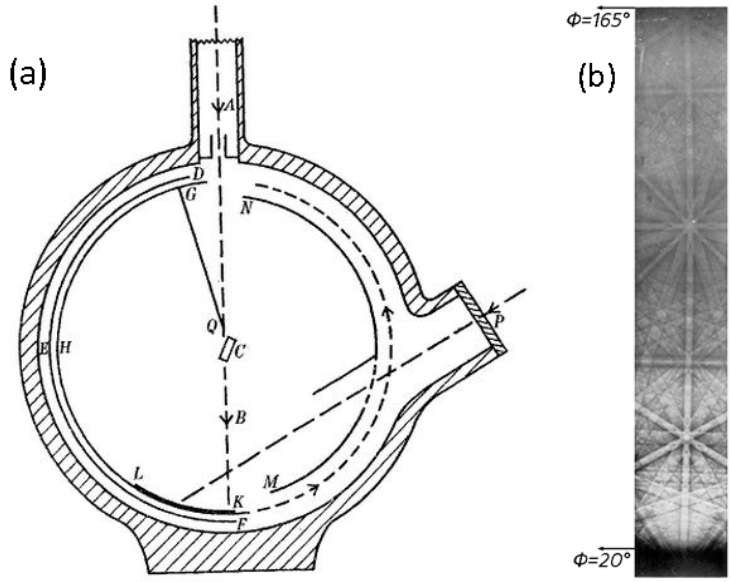

Figure 2.19 (a) Schematic representation of the specimen chamber and camera of the diffraction apparatus. A beam of electrons from a hot filament gun travels in the direction AB and impinges on the crystal specimen situated at C. A photographic film DEF is mounted on a cylindrical frame and records electrons scattered through angles up to 164°. (b) Backscatter diffraction pattern from lead sulphide obtained at 30 KeV [20].

A major advance towards faster and more user-friendly crystallographic orientation determination took place in 1984 when Dingley continued Venables earlier work with a phosphor screen and TV camera but with on-line computer-assisted indexing of the EBSD patterns [22, 23]. In this system, the video signal was sent through a frame store unit for temporal image averaging. This averaging improves the signal to noise ratio of the recorded pattern. The video signal was then sent to a computer controlled frame-grabber in such a way that the patterns can be digitized and accessed by the computer. This was a major step forward and became the model for modern-day EBSD systems.

The first commercial systems became available in 1986. They were marketed by Oxford Instruments and used the original Dingley software. Compared with modern systems the technology and especially the software were very elementary. A trained operator had to identify and locate three low-index poles in the pattern by visual inspection, and then the program calculated the rotation matrix. The requirement of a trained and experienced operator who must be able to identify and locate the low index zone axes was the main disadvantage of the software developed by Dingley [22, 23].

In 1989, a procedure developed by Schmidt and Olesen [24] represents an important step towards faster and more user friendly determination of crystal orientations from Kikuchi patters. In their technique, Kikuchi bands were used rather than zone axes to determine the orientation and the operator must identify the positions of three or more bands in the pattern by drawing the screen cursor along each band. The angles between the marked bands were determined and from the known camera geometry the corresponding inter-planar angles were calculated. Correct identification of the bands was assumed when there was a consistent matching of the experimentally measured and theoretical inter-band angles. This procedure did not require a highly skilled operator, and the corresponding computer program was able to analyze the patterns from materials of all crystal structures. Furthermore, it is an important advantage of the procedure that it is based on the position of bands, since the bands are easier to localize through digital image processing techniques.

The work of Schmidt was basically about the simulation of Electron Channeling Pattern (ECP) and led to the creation of a software package CHANNEL, which permitted rapid ECP pattern recognition and lattice-orientation determination. After that, Schmidt adapted his general indexing solution for ECP along with the technique of Dingley and Venables to create software to index all seven-crystal systems using EBSPs. With this, he founded HKL Technology in 1990 [25].

In 1991 and 1992 the first attempts for an automated determination of the orientation from an EBSD pattern was carried out by a research group from Yale University (Wright, Zhao and Adams [26, 27]. Their pattern indexation technique was based on the comparison between electron backscattering Kikuchi patterns and a set of idealized patterns and finding the best match. Shortly after that, Kunze, Wright, Adams and Dingley [28] introduced a completely automated system which couples automatic analysis of electron backscatter diffraction patterns with a

precise movement of the sample in the SEM. In their new approach to locate the bands in the diffraction pattern, they used the Hough transform for identifying lattice orientations through automatic analysis of EBSPs. Their hardware configuration included a high gain fiber optic camera to record video images, which were processed by the camera control unit. The control unit was capable of averaging 64 video frames and subtracting a background image, which was obtained when the SEM was in image mode. The sample holder was fixed on a piezoelectric x-y stage, which was mounted at an angle of 70° to the horizontal in the SEM vacuum chamber so as to obtain the grazing angle condition. The smallest possible step size was 0.1 µm. The camera control unit and the stage control unit were interfaced to a mini-super computer, and the computer was the central control unit for both the stage and the video camera unit (cf. **Figure 2.20**). Using the Hough transform to identify the bands provided the advantage of being somewhat material independent and faster for higher quality patterns [28].

In 1993, when rapid indexation was coupled with computer-controlled stage (or beam) motion, Adams et al [29] introduced the concept of orientation imaging microscopy (OIM^{TM}), which based on assigning color or gray scales to portions of the section plane corresponding to local lattice orientation. In 1994 the OIM™ development team (Adams and Dingley) founded TSL (TexSEM Laboratories Inc.) which offered the first commercially available fully automated EBSD System [30, 31].

Since then EBSD has gained popularity in many areas of research and developments. **Figure 2.21** represents the exponential growth in the number of EBSD related publications in the period of 1994 to 2012. Although EBSD has been widely used for microstructural characterization purposes, there are many other areas in which EBSD has played a crucial role in the progress of research. The main applications of EBSD are listed in **Table 2-5** [32]. By now, many attempts have been done to mainly improve the pattern indexation and the speed of pattern acquisition, although perhaps the most important progress was to include the determination of chemical composition and phase identification simultaneously with collection of the EBSD patterns [33].

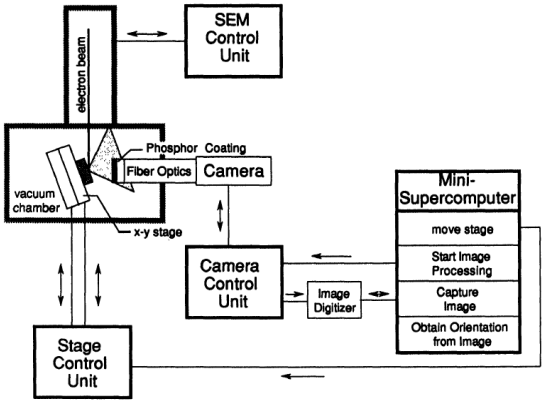

Figure 2.20 Schematic illustration of the automated backscatter Kikuchi pattern measurement system [28].

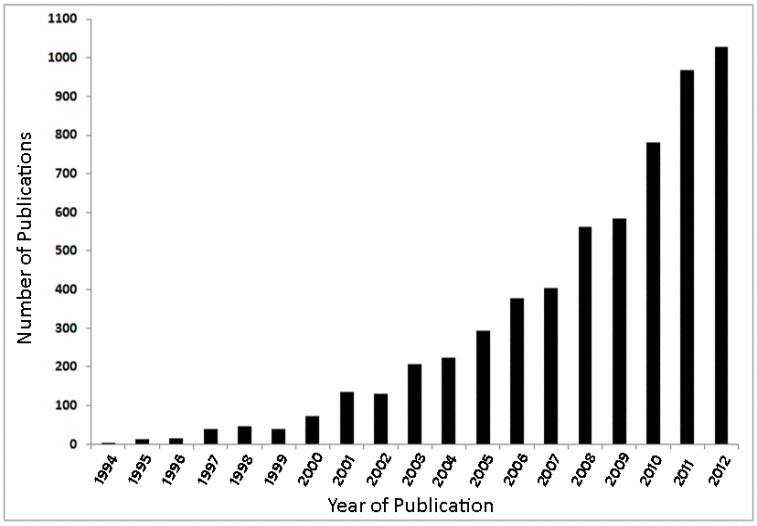

Figure 2.21 Growth in the number of EBSD related publications in the period of 1994-2012, (source: Web of Knowledge).

Table 2-5 The main applications of EBSD in materials characterization [32]

Application	Characterization
Materials development	- texture measurement and mapping - texture evolution and gradients - strain gradient measurement and mapping - grain morphology and grain fragmentation - grain boundary character distribution - phase identification - phase distribution and phase transformation
Process quality and control	- texture control in deformation and annealing processes - heat treatment effect on structural changes - heterogeneity of structures in welds - texture gradients in sputtering targets - grain size and texture in microelectronic devices - epitaxial layer in thin films - retained ferrite and austenite measurements in steel
Failure analysis	- texture effect on crack propagation behavior - grain boundary effect on corrosion, fracture and fatigue - grain boundary segregation and precipitation effect on creep - grain boundary sliding - identification of defects

2.4. Basics of EBSD: How It Works

The current configuration of the EBSD system is basically the same as the schematic representation in **Figure 2.20**. However, the modern systems have been equipped with an energy dispersive spectrometer which enables the simultaneous collection of the EBSD pattern and determination of chemical composition.

An automated electron backscatter diffraction system consists of three main components: the scanning electron microscope, the pattern acquisition system, and the software (cf. **Figure 2.22**). In the scanning electron microscope a stationary beam of primary electrons is focused on a small area of the specimen. The electrons interact with the surface of the specimen, and a fraction of them are diffracted depending on the arrangement of atoms. In order to maximize the fraction of backscattered electrons, the sample is tilted 70° with respect to the horizontal position (the angle between the specimen normal and the incident beam is 70°). Diffracted patterns are captured by a fluorescent phosphor. The interaction between the phosphor in the screen and the diffracted electrons, emits light which is suitable for a camera to record. The EBSD software controls the data acquisition, solves the diffraction patterns and stores the data in a file which will be analyzed later.

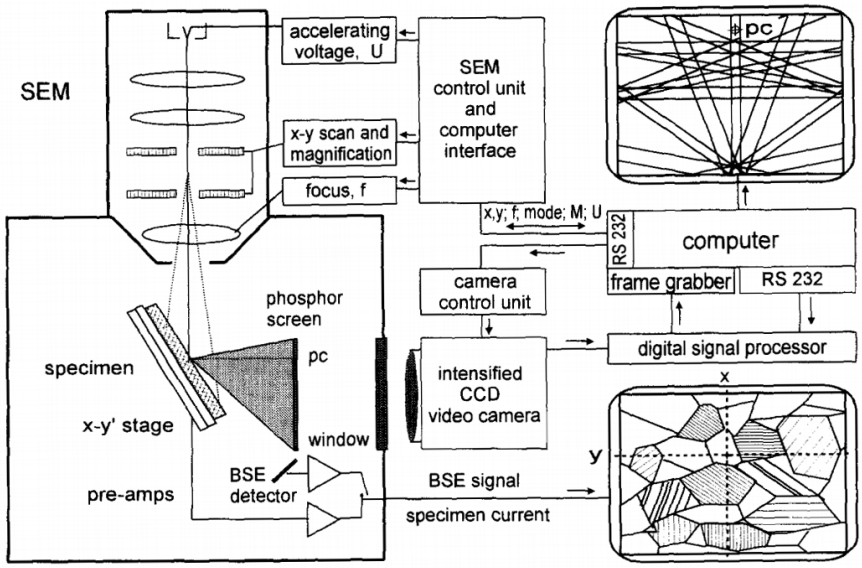

Figure 2.22 Schematic illustration of the components in a typical modern EBSD system [34].

2.4.1. Sample Preparation

As it was mentioned before the backscattered electrons are diffracted from the near sub-surface of the sample, within the top 50 nm or less. Therefore, it is essential that this top layer remains free from contamination and damage. The preparation of the sample surface is vital for capturing good quality patterns and a successful EBSD measurement. A careful polishing may transform a non-diffracting

sample into a high quality one, whereas neither the SEM adjustments nor the indexation parameters can do it.

> *"Optimum specimen preparation is a fundamental requirement for an EBSD experiment. Inadequate specimen preparation will result in degraded diffraction patterns which feed through to loss of data quality. Data clean-up routines can compensate in part for unsolved patterns but clean-up procedures should never be selected as an alternative to obtaining the best and most representative diffraction patterns." Randle, 2009, [35].*

Fortunately, the sample preparation for the EBSD is relatively easy (in comparison with the sample preparation for TEM). The important steps of a generic sample preparation suitable for metals are as follows [36, 37]:

- Grinding: Grinding is the first step of mechanical polishing and is carried out to remove the mechanically deformed layer developed during the cutting procedure. In order to make a planar flat surface, the grinding is usually started with a coarse grit (rough grinding) and then continues down to a finer grit (fine grinding). During grinding water is used to wash away waste material.
- Diamond Polishing: Diamond polishing is the second step of mechanical polishing and is done with finer abrasives in a diamond suspension or diamond paste. The finest grit size at this step is 0.25 μm.
- Oxide Polishing: Oxide polishing is the last step of the mechanical polishing which removes material by both mechanical and chemical means. The particles size of the oxide polishing media is generally 30 to 50nm diameter. After oxide polishing, a careful cleaning using alcohol and an ultrasonic bath is necessary to remove excess oxide particles.
  Table 2-6 shows the basic mechanical preparation method for ferrous metals recommended by Struers.
- Electropolishing: Although for many materials mechanical polishing will result in a good pattern quality, for some materials electropolishing is necessary to remove any remnant deformation and irregularities from the surface. Electropolishing is applied after conventional metallographic technique in an electrolytic solution where the sample acts as an anode in the electrolytic cell. The applied current dissolves the metal of the anode and deposits it on the cathode as a coating. There is no single electrolyte that works with all materials, and each material has a specific recipe which includes the electrolyte type, the operating voltage, the solution flow rate, the temperature of the electrolyte and the time of the electropolishing.
- Ion beam milling: In ion beam milling the surface of the material is bombarded by an ion beam and a layer is removed from the surface. This process may also cause some damage by ion implantation into the crystal lattice. Depending on the material, the size of the area, the ion gun current and the voltage, the process of ion milling may take 1 to 2 hours. Therefore, this method is limited to the preparation of very small areas. Ion milling can be also used for preparation of materials that are too soft for conventional preparation techniques.

Table 2-6 Basic mechanical preparation method for ferrous metals [38]

Step	Coarse Grinding	Fine Grinding	Diamond Polishing 1		Diamond Polishing 2	Oxide Polishing
Surface	SiC-Paper 320	MD-Largo	MD-Dur		MD-Nap	MD-Chem
Suspension		DiaPro Allegro 9µm	DiaPro Dur 3µm		DiaPro Nap 1µm	OP-S* 0.25µm
Lubricant	Water					
rpm	300	150	150		150	150
Force (N)	30	30	30	15		1100
Time (min)	1	5-10	5	5	5	1-5
*OP-S: Abrasive oxide polishing suspensions for polishing metallographic samples						

2.4.2. The Generation of EBSD patterns

Different interactions with a variety of signals occur when an electron beam is directed to the surface of a material. As the beam enters the surface (approximately 20nm deep) of a crystalline sample, diffuse and inelastic interactions lead to omni-directional scattering. As the electrons are arriving from all directions to the lattice planes, there must be always some electrons which fulfill the Bragg law (cf. **Equation 2.8**). These electrons can then undergo elastic scattering which results in a strong beam [39].

$$2d_{hkl}\sin\theta_{hkl} = n\lambda \qquad 2.8$$

where θ_{hkl} is the Bragg angle related to the interplanar spacing (d_{hkl}), n is the order of reflection and λ is the wavelength of the incident electron beam, which is dependent on the accelerating voltage (cf. **Figure 2.23**) [3].

The diffraction of electrons through the Bragg angle occurs in all directions, therefore, the locus of diffracted electrons is a pair of cones with a large opening angle of 180°-2θ. The axes of these cones (known as Kikuchi or Kossel cones) are perpendicular to the diffracting lattice planes (cf. **Figure 2.24**). These two cones of reflected electrons are symmetric with respect to the reflecting lattice plane and the separation angle between them is 2θ. For typical values of electron wavelength and interplanar spacing of lattice planes, the Bragg angle (θ) is about 0.5°. Consequently, the intersection of these cones with the phosphor screen of the EBSD camera is a pair of nearly straight parallel lines. These are Kikuchi lines and their spacing is 2θ which is inversely proportional to the lattice spacing (d) (cf. **Equation 2.8**) [39, 40].

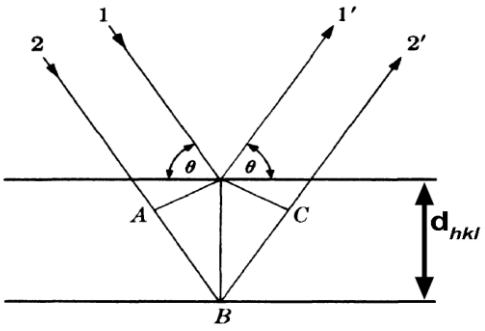

Figure 2.23 Diffraction from lattice planes, indicating the geometry which leads to the derivation of Bragg's law [3].

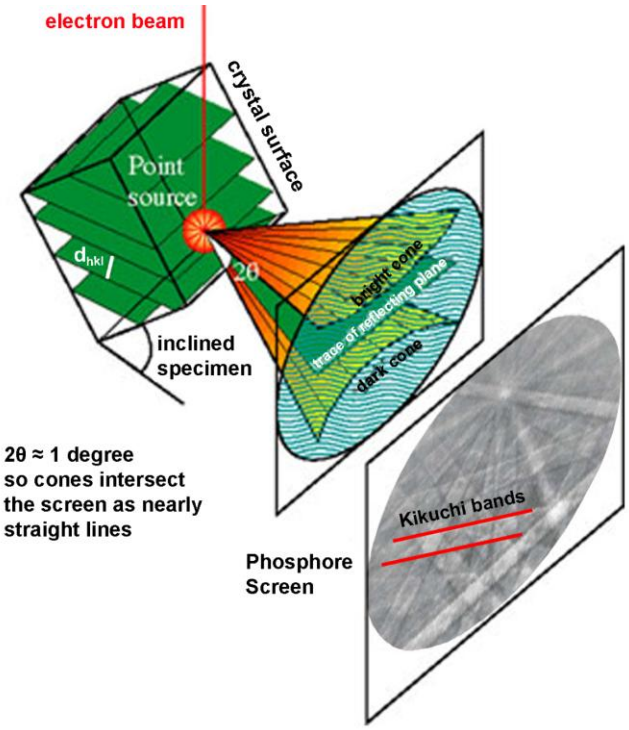

Figure 2.24 Schematic representation illustrating the generation of Kikuchi patterns in the SEM chamber with respect to the diffracting plane, the specimen, and the phosphor screen[41].

Each pair of parallel lines is called a band, and a set of several bands defines a Kikuchi pattern. The Kikuchi pattern is the first output of an EBSD analysis. Except of the Kikuchi bands, a Kikuchi pattern consists of a diffuse background of non-uniform intensity which is produced by inelastically scattered electrons. The intersection of bands corresponds to a zone axis or a pole, and major zone axes are recognized by the intersection of several bands. The Kikuchi pattern, therefore, contains angular crystallographic information (interplanar and interzonal) which enables the specification of the crystal symmetry. The crystal symmetry together with the interplanar and interzonal angular relationships are used to specify the crystallographic poles and the crystallographic indices of the Kikuchi bands [39].

2.4.3. Pattern Acquisition and Band Detection

The generated Kikuchi pattern is projected on a transparent phosphor screen which is in front of the specimen. The development of the EBSD camera was historically started by the work of Alam et al. [20] in which the Kikuchi patterns were directly recorded on a fluorescent screen. In 1984, Dingley et al. [22] used a low-light silicon-intensified target (SIT) video camera for imaging the patterns which had resulted in a reduction in the probe current (down to 0.5nA compared to 20nA).

The SIT video cameras were soon replaces by a charged couple device (CCD) video camera. With these CCD cameras there is no geometric distortion of the diffraction pattern, which was observed with the oldest techniques. Furthermore, the lifetime of a CCD camera is longer and they are smaller and lighter. However, to obtain EBSD patterns by a CCD camera, a higher probe current is necessary which does not have strong effect on the EBSD spatial resolution [42].

Most commercial systems now employ the CCD cameras which can fulfill both fast scan speed and high quality EBSD pattern collection. The practical indexation rate is currently in the range of 600–800 frames per second [43]. As it can be seen in **Figure 2.25**, since the development of the technique this rate has increased exponentially and will probably continue to increase with more powerful computers and optimized image processing algorithms.

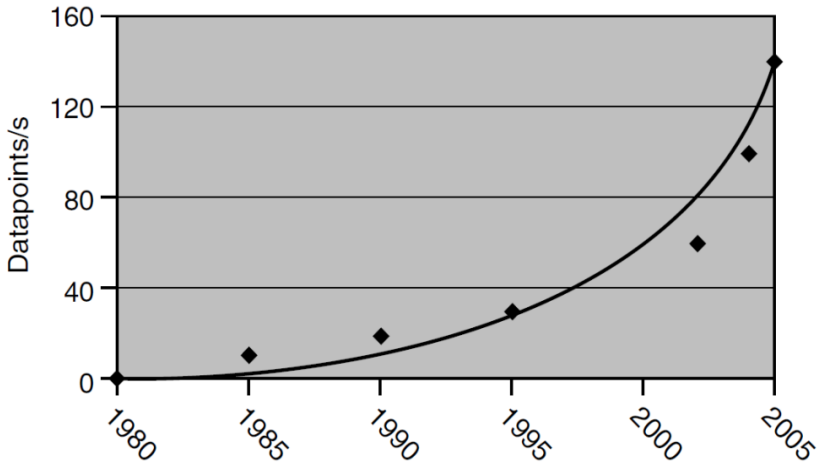

Figure 2.25 Evolution of EBSD pattern acquisition speed by year [2].

The next step after acquiring the Kikuchi pattern is the processing of this pattern which includes the detection of the Kikuchi bands. The main problem here is the recognition of the low contrast bands in the patterns. As the first approach, Wright et al. [26] tried to directly detect the positions of the zone axes which was carried out by convolution of the diffraction pattern with a filter to detect regions with a high intensity, i.e. the zone axes compared to their neighborhood.

Using a filter to detect the zone axes was very sensitive to the camera distortions

and calibration parameters, therefore another algorithms based on the detection of the bands position was developed. To this purpose, Wright et al. [27] adapted an edge detection algorithm called Burns algorithm [44] which extracts the edges by grouping pixels together into regions based on correlations of their gradient orientations. Their technique showed promising preliminary results and the Kikuchi patterns for silicon and stainless steel were correctly identified by the computer. However, significant increase in the speed of the procedure was required.

A different approach transforms the Kikuchi patterns by means of the Hough transform [45] to detect the bands location. In this method, straight lines in the original image are transformed to points, which can be detected more easily by computer codes. The equation governing the Hough transform is:

$$\rho = X \cdot cos\theta + Y \cdot sin\theta \qquad 2.9$$

where X and Y are the coordination of a set of pixels forming a band in the Kikuchi pattern (cf. **Figure 2.26a**). θ and ρ are the Hough transform parameters which transform each point of the Kikuchi pattern into a sinusoidal curve in the Hough space (cf. **Figure 2.26b**). The intersection point of the sinusoidal curves of all points belonging to the same band is a single point in the Hough space (point "H" in **Figure 2.26b**). This point which represent the Hough transform of a band has two parameters: the ρ value, which corresponds to the shortest distance between the band and a reference point in the Kikuchi pattern, and the θ value, which is the angle between ρ and the horizontal line. In order to perform the Hough transform, the Hough space is divided into discrete bins and the intensity at each X and Y pixel in the Kikuchi pattern is added into all corresponding bins on the curve defined by **Equation 2.9** [27-29, 46].

By applying a Hough transform on a Kikuchi pattern, the problem of detecting a band in the diffraction pattern is reduced to finding a peak of high intensity in the Hough space which is comparatively easier. **Figure 2.27** shows an EBSD pattern with its detected bands and the corresponding Hough transform, which was used to find the bands.

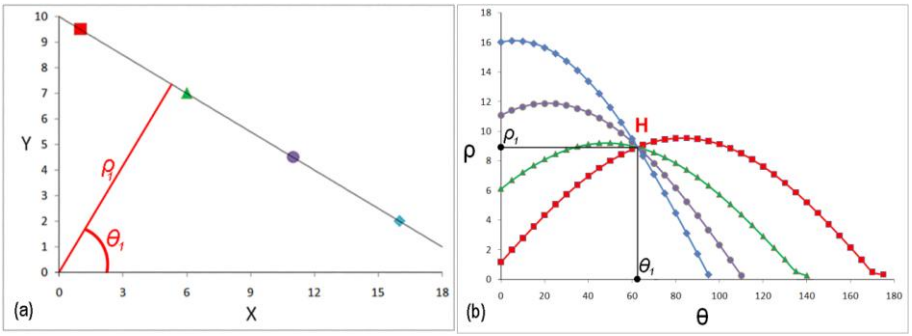

Figure 2.26 Schematic representation of Hough transform parameters, (a) X-Y space, (b) sinusoidal curves of different points from the same band in the Hough space.

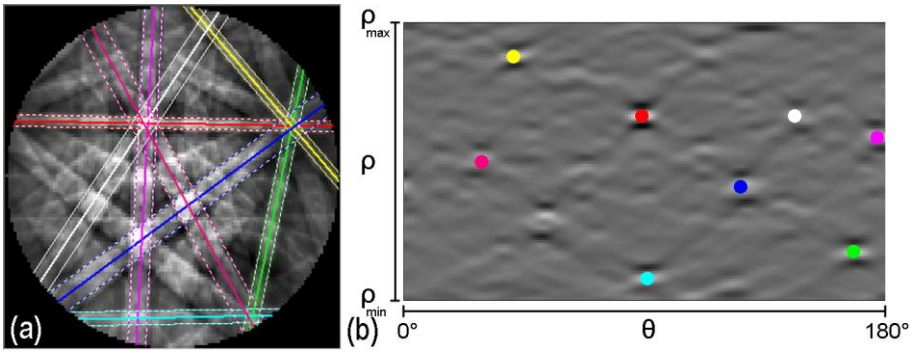

Figure 2.27 (a) A Kikuchi pattern with the detected bands, (b) the corresponding Hough transform.

2.4.4. SEM Specifications

In order to equip a SEM with an EBSD system, the SEM must meet a certain number of basic requirements. The microscope chamber should be large enough to accommodate the EBSD camera and the stage. The stage should have the freedom to be tilted 70° (or less in the case of using a pre-tilted sample holder) from the horizontal position to face the camera. When the sample stage is tilted, it should not touch any of the detectors and the pole piece. Furthermore, there are several parameters in the SEM which affect the EBSD analysis. These parameters and their effects are shortly described here:

- Probe current: Increasing the probe current will result in a stronger diffraction pattern signal, which increases the pattern quality. This will allow the pattern acquisition at a higher speed. However, since the diameter of the beam is proportional to the square root of the beam current, increasing the probe current will also increase the diameter of the electron beam which will results in a lower spatial resolution. Therefore, in the case of samples with very fine grains or in regions with a high dislocation density, a smaller probe current is preferred. A standard probe current for EBSD work is in the range of 1 to 5nA, although anything in the range of 0.25 to 50nA is commonplace [18, 36, 43].

- Lens aperture: As the aperture of the lens and therefore the probe current increases usually spatial resolution decreases. This has been attributed to the depth of focus because larger apertures give less depth of focus in the image. This effect is more important when the sample is titled and can be corrected by using the dynamic focus tool. Practically, the best aperture size is the smallest one that allows for the necessary probe current for EBSD, which is usually around 50 to 60µm diameter [36].

- Accelerating voltage: the Accelerating voltage is an important parameter for an EBSD measurement. In general, there is a direct relationship between the accelerating voltage and the interaction volume in the material. As the accelerating voltage increases, the spatial resolution decreases and the data

collection will be faster. Therefore, where good spatial resolution is required: e.g. for fine grained or deformed material, the smaller accelerating voltage is required [18].

On the other hand, by decreasing the accelerating voltage below 10kV, the phosphor screen will produce less light which results in a noisy and less visible pattern. Therefore, the accelerating voltage should be chosen considering a good compromise between the spatial resolution, the pattern quality and the speed of the measurement. The accelerating voltage is also dependent on the atomic number of the material. Materials with higher atomic number generate higher fraction of backscattered electrons which is advantageous for decreasing the accelerating voltage [36].

Generally the accelerating voltage is in the range of 10 to 30kV. However, in the early work of Dingley et al. [22] patterns have been viewed on the phosphor screen with accelerating voltage as low as 4kV.

- Working Distance: the Working Distance (WD) is the distance between the specimen and the bottom of the pole piece (cf. **Figure 2.28**). This optimum WD is dependent on the SEM type and the position of the EBSD detector. For standard SEM work the best resolution and minimized focusing distortions are obtained from a short working distance. However, for EBSD acquisition the limiting factors are the relative position of the sample with respect to the microscope hardware, i.e. collision with the pole piece and the phosphor screen should be avoided [18].

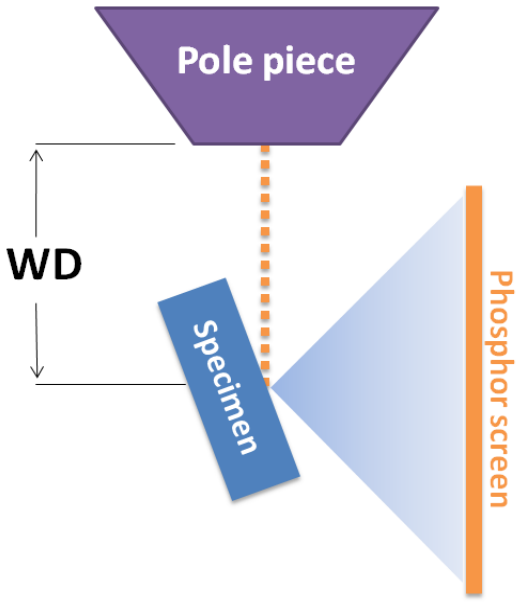

Figure 2.28 Schematic representation of the working distance (WD) in a scanning electron microscope.

- Tilt angle: The specimen in an EBSD measurement must be tilted to obtain a reasonably large fraction of backscattered electrons. Reducing the tilt angle improves the spatial resolution which is useful for the analysis of samples with considerable surface roughness [36]. Venables et al. [21] have observed patterns with tilt angles down to 45 °. They reported that the path length of the backscattered electrons decreases with increasing the tilt angle which leads to a better contrast in the EBSD pattern. Reasonable contrast can be obtained with the tilt angle over the range of 65-85 °. Above 85 ° the elongation of the probe along the specimen inclined surface results in a diffuse pattern [22]. Nowadays, most EBSD measurements are carried out with a tilt angle of 70°, which results in the best compromise between the strength of the diffraction pattern signal and the spatial resolution.

2.4.5. Mapping

Since the development of fully automated pattern acquisition and indexation, orientation mapping has been the most common way of using the EBSD technique. During orientation mapping, the diffraction patterns are collected point by point on a grid defined by the operator. The image is then reconstructed by assigning colors depending on the orientation or crystal phase of each pixel. Mapping is carried out by displacing the electron probe on the sample in the defined grid and can be done with two sample codes:

- Stage scanning mode, in which the sample is moved mechanically under the focused stationary electron beam by means of a computer controlled sample stage [28, 29].
- Beam scanning mode, in which the sample is fixed and the electron beam moves across the sample surface [43].

Stage scanning method is performed using a high-precision specimen stage which moves the sample relative to the electron beam. Nowadays a motorized sample motion is a standard feature in the SEMs and therefore the stage scanning mode does not need any additional hardware. By combining the stage scanning with an eucentric stage the working distance and other calibration parameters remain constant during scanning, i.e. the sample is always located at the position for which the calibration and focusing have been done and the measurement can be carried out without re-focusing or re-calibrating [18].

The stage scanning method can be used to scan a large area, whereby the limiting factor is the sample stage moving range. Furthermore, the diffraction geometry, i.e. pattern center position, specimen-to-screen distance and background intensity remain constant from point to point. In this method there is no geometric distortion resulting from the tilted specimen surface or beam deflection and focus settings remains constant. On the other hand, in the stage scanning mode the stage positioning resolution governs the minimum possible step size. Practically it is not possible to reach very small values of step size in the stage scanning mode. Moreover, because of the mechanical nature of the stage positioning this method is relatively slow [43].

Alternatively, in the beam scanning mode, the EBSD software controls the SEM deflection coils and the electron beam can be positioned much faster and more precisely than the stage scanning mode. With this method, relatively large areas can be scanned at low magnifications in which the electron beam should be largely deflected away from the image centre. Consequently the electron image of the sampling area may be distorted and the diffraction geometry and pattern center change at each point on the sample surface (cf. **Figure 2.29**). Therefore, an autocalibration must be applied to dynamically calibrate the system from point to point, otherwise, the errors in the calculated orientations may easily exceed several degrees [18, 43].

Considering the advantages and disadvantages of two techniques, accurate and fast EBSD mapping of large areas is possible with a combination of both methods. The sample is positioned at the region of interest by using the translation of the stage, and the orientations are scanned in the desired grid by beam control. The sample can mechanically move to the next position and the process can be repeated to cover a larger area [18].

2.4.6. Image Quality

The perfection of the crystal lattice affects the pattern quality. For example, if a lattice was elastically strained and the atomic plane is bended, then the plane would no longer exactly satisfy the Bragg condition which results in a more diffuse band within the pattern. Therefore, any distortions of the crystal lattice will reduce the quality of the diffracted patterns [47]. The image quality (IQ) is a parameter related to the crystallographic uniformity of the characterized volume and is extracted from the quality of Kikuchi bands, i.e. intensity, sharpness, contrast, noise level. High quality Kikuchi bands have intense Hough peaks and their average intensity (cf. **Equation2.10**) is greater than lower quality Kikuchi bands [32].

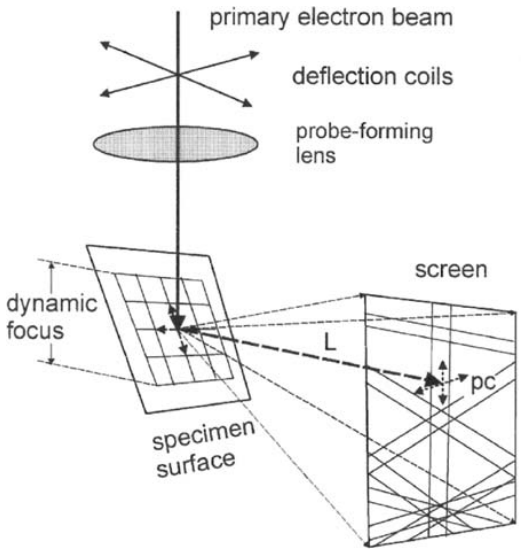

Figure 2.29 Raster grid on a tilted specimen surface with beam scanning mode [43].

$$IQ = \frac{1}{N}\sum_{i=1}^{N} I_i \qquad 2.10$$

Here , IQ is the average image quality, *N* is the number of identified Hough peaks, and I_i is the intensity of the peak *I [47]*.

The IQ parameter does not represent an absolute intrinsic material characteristic, but depends on the material and the measurement conditions, i.e. the sample preparation, technique and parameters used to index the pattern. Elements with higher atomic numbers produce stronger patterns due to higher scattering efficiency. Therefore EBSD on multiphase materials will show contrast in the IQ map due to the different phases present. The image quality is also slightly affected by the orientation but this impact is much smaller than the one due to phase, grain boundaries and strain. Thus, it cannot be used to distinguish small differences in the crystallographic orientation of grains [11].

Consequently, image quality provides complementary information to the indexed crystallographic orientations. For example, in deformed samples in which the dimensions of the crystal lattice are distorted, a greater angular distribution of diffracted crystallographic planes decreases the Kikuchi band sharpness and results in lower image quality [32].

2.4.7. Confidence Index

In order to determine the crystal lattice orientation, the measured interplanar angles of the diffracted patterns are compared with a computer-generated list of ideal angles between diffracting planes of the same crystal type. Usually, more than a unique solution is found for each three Kikuchi bands. The confidence in the final solution can be measured by a parameter which is determined from the number of similar orientations found for a given set of bands. This parameter which is called the confidence index (CI) is based on a voting scheme [48]. All possible sets of three bands are formed and a vote is assigned to a given orientation for each set of three bands satisfying the solution. The confidence index (CI) is defined by:

$$CI = \frac{V_1 - V_2}{V_{ideal}} \qquad 2.11$$

Where V_1 and V_2 are the number of votes for the first and second most likely solutions, respectively. V_{ideal} is the total possible number of votes for the detected bands. The confidence index ranges from 0 to 1. A CI of -1 is assigned to a pattern that cannot be analyzed. **Figure 2.30** shows a sample study of the confidence index on an FCC material. It has been reported that for images where at least six Kikuchi bands were identified (correctly or incorrectly), with a CI of 0.1 or greater, the solution was 95% correct. It should be noted that a confidence index of 0 is achieved when $V_1 = V_2$. In this case, the solution which has the smallest angular deviation from the theoretical value is chosen and the pattern may still be correctly indexed [48].

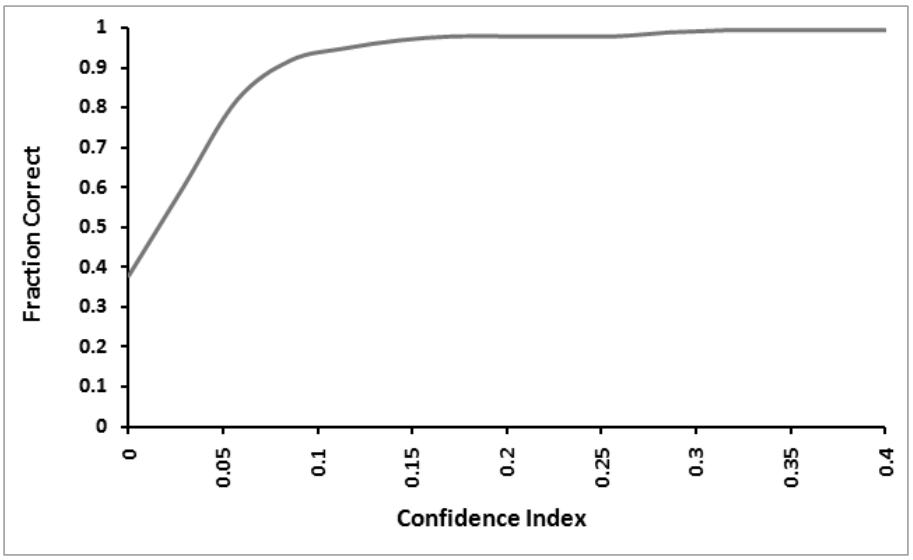

Figure 2.30 Confidence index versus fraction of correct solutions for an FCC material [48].

2.4.8. Spatial Resolution

If there is more than one crystallographic orientation in the diffracted area, the pattern solution may fail and the pattern will not be indexed. Therefore, in order to study fine grains and heavily deformed materials, a high spatial resolution in orientation measurement is required [43].

The spatial resolution of EBSD is influenced by the material and the microscope parameters, i.e. the atomic number, the specimen/microscope geometry, the accelerating voltage, the probe current and the diffraction pattern quality. The best spatial resolution for a material such as brass is 25–50 nm in a SEM with a tungsten filament. By using a field emission gun SEM (FEG-SEM) the spatial resolution of 9–22 nm was obtained for the same material [35]. It should be noted that due to the tilt of the sample, the spatial resolution parallel to the tilt axis (δ_x in **Figure 2.31**) is typically around three times better than the spatial resolution perpendicular to the tilt axis (δ_y) [17, 43].

Furthermore, there are other critical factors, which affect the spatial resolution. The optimization of focus and astigmatism and the stability of beam and sample stage are critical for achieving the best spatial resolution. The quality of the sample preparation is also very important, as any contamination and polishing-induced deformation will be detrimental to the spatial resolution [36].

It is worth to mention that EBSD software such as CHANNEL 5 developed by Oxford instruments is able to deconvolute patterns that have a signal coming from 2 grains. In fact the software chooses the pattern which has the stronger signal. With this, an effective spatial resolution less than 10 nm can be achieved, even though the absolute resolution may be in the range of 20-50 nm[36] .

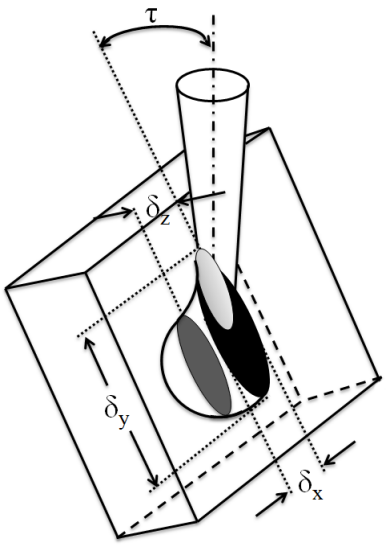

Figure 2.31 Schematic representation of spatial resolution in different directions for a tilted sample [43].

2.4.9. Angular Resolution

The angular resolution of EBSD represents the minimum misorientation between 2 neighboring crystals that still can be distinguished. The relative orientation of a crystal with respect to its neighbor is typically obtained with an accuracy of approximately 0.5° to 1.0° which depends on the resolution of the EBSD detector and its position with respect to the sample. This angular resolution is enough for most standard textural analyses, however, the need for improved angular resolution might be required for strain and small lattice rotation measurements.

The angular resolution also depends on the diffraction pattern quality (the sharpness of the pattern and the resolution of the Hough space) and the magnification of the diffraction pattern. With careful indexing of the influencing parameters, the angular resolution of less than 0.2° can be achieved [2, 36].

2.4.10. Phase Identification

The EBSD technique can also be used for phase verification and phase identification. In phase verification the present phases are preselected by the operator and the phase search is carried out only between these choices. To apply the phase verification the structural information of the crystal is extracted from the Kikuchi pattern. This procedure is on the basis of the early work of Dingley et al. [49] and it includes the determination of the crystal system from detection of the rotation axes in a diffraction pattern. The point group is determined from the observed combination of the mirror planes and the rotation axes. Finally the Bravais lattice and the space group are determined. This information is then compared with a small database which includes the ideal values for the preselected phases. The phase with a good match is then selected and a phase ID is assigned to that point [50, 51].

In phase identification, on the other hand, the phases are unknown and the entire database of crystalline phases should be searched for a good match which is practically impossible. To overcome this shortcoming, the qualitative chemistry of the phases present in material are obtained by chemical characterization and the search in the database is limited to the phases which are composed by the elements found in the material. Therefore, for comprehensive phase identification, two components of the phase, i.e. structure and chemistry must be taken into account. To this purpose, the EBSD needs to be supplemented by a chemical characterization technique. By simultaneous diffraction and compositional data collection with a technique such as energy dispersive X-ray spectroscopy (EDS), EBSD can be used for complete identification of unknown phases [51-53].

2.5. References

1. Dingley, D.J., *The development of automated diffraction in scanning and transmission electron microscopy*, in *Electron Backscatter Diffraction in Materials Science* A.J. Schwartz, M. Kumar, and B.L. Adams, Editors. 2000, Kluwer Academic/Plenum Publ. p. 1-18.
2. Maitland, T. and S. Sitzman, *Electron Backscatter Diffraction (EBSD) Technique and Materials Characterization Examples*, in *Scanning Microscopy for Nanotechnology: Techniques and Applications*, W. Zhou and Z.L. Wang, Editors. 2006, Springer: New York. p. 41-75.
3. Cullity, B.D., *Elements of x-ray diffraction*. Second ed. 1978: Addison-Wesley.
4. Szwacki, N.G. and T. Szwacka, *Basic Elements of Crystallography*. 2010: Pan Stanford Publishing.
5. De Graef, M. and M.E. McHenry, *Structure of Materials: An Introduction to Crystallography, Diffraction and Symmetry*. 2007: Cambridge University Press.
6. Woolfson, M.M., *An Introduction to X-ray Crystallography*. second ed. 1997: Cambridge University Press.
7. Chatterjee, S.K., *Crystallography and the World of Symmetry*. 2008: Springer Berlin Heidelberg.
8. Kocks, U.F., C.N. Tomé, and H.R. Wenk, *Texture and Anisotropy: Preferred Orientations in Polycrystals and Their Effect on Materials Properties*. 2000: Cambridge University Press.
9. Callister, W.D., *Fundamentals of materials science and engineering: an interactive e.text*. Fifth ed. 2000: John Wiley and Sons.
10. Hammond, C., *The Basics of Crystallography and Diffraction*. third ed. 2009: OUP Oxford.
11. *OIM ANALYSIS user manual* 2001, TexSEM Lab.
12. Bunge, H.J., *Texture analysis in materials science : mathematical methods; translated by Peter R. Morris*. 1982, London ; Boston: Butterworths.
13. Frank, F.C., *ORIENTATION MAPPING.* Metallurgical Transactions a-Physical Metallurgy and Materials Science, 1988. **19**(3): p. 403-408.
14. Randle, V., *Representation of grain misorientations (mesotexture) in Rodrigues-Frank space.* Proceedings of the Royal Society of London Series a-Mathematical Physical and Engineering Sciences, 1990. **431**(1881): p. 61-69.
15. Neumann, P., *Representation of Orientations of Symmetrical Objects by Rodrigues Vectors.* Textures and Microstructures, 1991. **14**: p. 53-58.
16. Mason, J.K. and C.A. Schuh, *Representations of Texture*, in *Electron Backscatter Diffraction in Materials Scince*, A.J. Schwartz, et al., Editors. 2000, Springer. p. 35-52.
17. Humphreys, F.J. and M. Hatherly, *Recrystallization and Related Annealing Phenomena*. Second ed. 2004: Elsevier Science.
18. Randle, V. and O. Engler, *Introduction to Texture Analysis: Macrotexture, Microtexture and Orientation Mapping*. 2000: Gordon and Breach Science Publishers.

19. Nishikawa, S. and S. Kikuchi, *Diffraction of cathode rays by calcite.* Nature, 1928. **122**.
20. Alam, M.N., M. Blackman, and D.W. Pashley, *High-angle Kikuchi patterns.* Proc. Royal Society of London, 1954. **221**: p. 224-242.
21. Venables, J.A. and C.J. Harland, *Electron Backscattering Patterns - New Technique for Obtaining Crystallographic Information in Scanning Electron-Microscope.* Philosophical Magazine, 1973. **27**(5): p. 1193-1200.
22. Dingley, D.J., *Diffraction from Sub-Micron Areas Using Electron Backscattering in a Scanning Electron-Microscope.* Scanning Electron Microscopy, 1984: p. 569-575.
23. Dingley, D.J., et al., *On-line analysis of electron backscatter diffraction patterns, texture analysis of polysilicon.* Electron Microscopy, 1987. **11**: p. 451-456.
24. Schmidt, N.H. and N.O. Olesen, *Computer-Aided Determination of Crystal-Lattice Orientation from Electron-Channeling Patterns in the Sem.* Canadian Mineralogist, 1989. **27**: p. 15-22.
25. *Channel 5 Users Manual*. 2006, Denmark: Oxford Instruments ®, HKL Technology.
26. Wright, S.I., J.W. Zhao, and B.L. Adams, *Automated-Determination of Lattice Orientation from Electron Backscattered Kikuchi Diffraction Patterns.* Textures and Microstructures, 1991. **13**(2-3): p. 123-131.
27. Wright, S.I. and B.L. Adams, *Automatic analysis of electron backscatter diffraction patterns.* Metallurgical Transactions a-Physical Metallurgy and Materials Science, 1992. **23**(3): p. 759-767.
28. Kunze, K., et al., *Advances in Automatic EBSP Single Orientation Measurements.* Textures and Microstructures, 1993. **20**(1-4): p. 41-54.
29. Adams, B.L., S.I. Wright, and K. Kunze, *Orientation Imaging - the Emergence of a New Microscopy.* Metallurgical Transactions a-Physical Metallurgy and Materials Science, 1993. **24**(4): p. 819-831.
30. *EDAX*. 2013; Available from: http://www.edax.com/EDAX/history.aspx.
31. Dingley, D. *Home for EBSD*. Available from: http://www.ebsd.org.uk/.
32. Stojakovic, D., *Electron backscatter diffraction in materials characterization.* Processing and Application of Ceramics, 2012. **6**(1): p. 1-13.
33. Wright, S.I. and D.P. Field, *Analysis of multiphase materials using electron backscatter diffraction.* MICROSCOPY AND MICROANALYSIS, 2000. **3**: p. 561-562.
34. Schwarzer, R.A., *Automated crystal lattice orientation mapping using a computer-controlled SEM.* Micron, 1997. **28**(3): p. 249-265.
35. Randle, V., *Electron backscatter diffraction: Strategies for reliable data acquisition and processing.* Materials Characterization, 2009. **60**(9): p. 913-922.
36. *Reference Manual and 3D-EBSD*. Oxford Instruments ®, HKL Technology.
37. *EBSD*. 2013; Available from: www.ebsd.com.
38. *Preparation of ferrous metals for Electron Backscatter Diffraction (EBSD) analysis*, in *Application Notes*. 2010, Struers.
39. Randle, V., *Theoretical Framework for Electron Backscatter Diffraction*, in *Electron Backscatter Diffraction in Materials Science*, A.J. Schwartz, M.

Kumar, and B.L. Adams, Editors. 2000, Kluwer Academic/Plenum Publ. p. 19-30.

40. Zaefferer, S., *On the formation mechanisms, spatial resolution and intensity of backscatter Kikuchi patterns.* Ultramicroscopy, 2007. **107**(2–3): p. 254-266.
41. *How EBSD measurements work*. Available from: http://www.gm.univ-montp2.fr/.
42. Hjelen, J., A.H. Qvale, and O. Gomo, *ELECTRON MICRODIFFRACTION (EBSP) IN THE SCANNING ELECTRON-MICROSCOPE (SEM) - FURTHER HARDWARE DEVELOPMENT TO IMPROVE PATTERN QUALITY*, in *Proceedings of the 10th International Conference on Textures of Materials, Pts 1 and 2 - Icotom-10*, H.J. Bunge, Editor. 1994. p. 137-142.
43. Schwarzer, R.A., et al., *Present State of Electron Backscatter Diffraction and Prospective Developments*, in *Electron Backscatter Diffraction in Materials Science* A.J. Schwartz, M. Kumar, and B.L. Adams, Editors. 2000, Kluwer Academic/Plenum Publ.
44. Burns, J.B., A.R. Hanson, and E.M. Riseman, *EXTRACTING STRAIGHT-LINES.* Ieee Transactions on Pattern Analysis and Machine Intelligence, 1986. **8**(4): p. 425-455.
45. Hough, P.V.C., *Methods and means for recognizing complex patterns*. 1962.
46. Wright, S.I., *Fundamentals of Automated EBSD*, in *Electron Backscatter Diffraction in Materials Science*, A.J. Schwartz, M. Kumar, and B.L. Adams, Editors. 2000, Kluwer Academic/Plenum Publ. p. 51-64.
47. Wright, S.I. and M.M. Nowell, *EBSD image quality mapping.* Microscopy and Microanalysis, 2006. **12**(1): p. 72-84.
48. Field, D.P., *Recent advances in the application of orientation imaging.* Ultramicroscopy, 1997. **67**(1-4): p. 1-9.
49. Dingley, D.J. and K. Babakishi, *Use of electron back scatter diffraction for determination of crystal symmetry elements.* Scanning Electron Microscopy, 1986: p. 383-391.
50. Baba-Kishi, K.Z., *Review - Electron backscatter Kikuchi diffraction in the scanning electron microscope for crystallographic analysis.* Journal of Materials Science, 2002. **37**(9): p. 1715-1746.
51. Goehner, R.P. and J.R. Michael, *Phase identification in a scanning electron microscope using backscattered electron Kikuchi patterns.* Journal of Research of the National Institute of Standards and Technology, 1996. **101**(3): p. 301-308.
52. El-Dasher, B. and A. Deal, *Application of Electron Backscatter Diffraction to Phase Identification*, in *Electron Backscatter Diffraction in Materials Scince*, A.J. Schwartz, et al., Editors. 2000, Springer. p. 81-95.
53. Dingley, D., *Progressive steps in the development of electron backscatter diffraction and orientation imaging microscopy.* Journal of Microscopy-Oxford, 2004. **213**: p. 214-224.

Chapter 3. Three-Dimensional Characterization Techniques

"Nature shows us only the tail of the lion. But I do not doubt that the lion belongs to it even though he cannot at once reveal himself because of his enormous size."

Albert Einstein
quoted by Abraham Pais in "Subtle is the Lord: The Science and Life of Albert Einstein" (1982), p. 235

3.1. Introduction

The microstructure of materials has a three dimensional nature. But, because the majority of the materials are opaque for either low energy electrons or photons, microstructural characterization is conventionally carried out in two-dimensions (2D). Although it is possible to readily characterize a vast number of microstructural features in 2D, there are still many features of the real three dimensional microstructure that can only be measured in three-dimension (3D). The number of features per volume, the true size and shape of microstructural elements, the connectivity between features, the grain boundary inclination and the interface morphology are examples of microstructural information that can be obtained only from 3D microscopy instrumentation. Therefore, the 3D description of the microstructure is of crucial importance for a better understanding of the structure-properties relationships in polycrystalline materials.

The techniques for 3D characterization of the microstructures are on the basis of two different approaches: (i) observation with high-energy radiation and (ii) by serial sectioning. Furthermore, some stereological methods have been proposed and employed to derive 3D information from 2D images. This chapter provides basic information about these techniques, their advantages, limitations and their applications. The above mentioned techniques will be compared with regard to their spatial resolution, width-of-field and speed of the measurement. As in this thesis serial sectioning technique is used for characterization of 3D microstructures, this technique will be studied in more details with some examples of senior researchers.

3.2. Stereological Techniques

Stereology is the quantitative estimation pertaining to the real shape of a feature (number, length, surface area and volume) within a volume. This quantification is obtained by recording the intersection of random "geometrical probes" with the features of interest. Depending on the dimension of the feature of interest, the probes may have various dimensions including 3D volumes, 2D planes (i.e. sections), lines and points. In classical stereology the geometrical probes are applied by cutting a 3D object into thin sections and then using a 2D grid on the sections. Estimations of volume, surface and length can be obtained depending on the dimensionality of the grid (points, lines and planes) [1].

The procedure of sectioning a 3D volume with a 2D plane is explained in **Figure 3.1**. The 3D volume of a solid apple after cutting with a plane is a 2D section, while its 2D surface will appear as a 1D boundary trace. A worm in the 3D space of the apple is shown as three small profiles in the 2D section. As it is summarized in **Table 3-1**, the dimensionality of a feature on a 2D section is equal to its dimensionality in 3D minus 1 [1]. In other words, sectioning an object causes losing one degree of its geometrical dimensionality, and stereology is used to estimate this lost dimensionality from 2D sections.

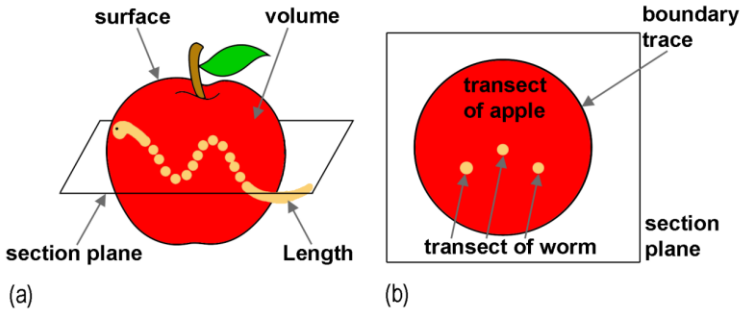

Figure 3.1 (a) The dimensions in the 3D world including volume (L^3), surface (L^2) and length (L), (b) Appearance of 3D objects on a 2D section as plane (L^2), boundary trace (L^1) and points (L^0), respectively.

Table 3-1 The relationship between dimensions in 3D and those seen on a 2D section [1]

3D	2D
Volume (L^3)	Profile (L^2)
Surface (L^2)	Boundary (L)
Length (L)	Countable event (L^0)

Classical stereology is widely used for estimating the volume, surface, length, curvature and number of spatial features from their 2D sections. Additionally, in materials science stereology has been extensively employed to estimate the volume fraction of different phases, the surface density of grain boundaries, the length density of triple lines, and to study the topological properties of porous networks [2].

Furthermore, stereological techniques have been used for describing the intercrystalline structure distribution on the basis of observations from a single planar section. It is well known that the orientation of the grain boundary plane is important for calculation and determination of grain boundary properties and energy. The conventional 2D EBSD reveals the misorientation between two adjacent grains and a trace of the grain boundary plane in a 2D section, i.e. four of the five parameters necessary to determine the complete distribution of grain boundary character. Some stereological methods have been proposed for a more complete characterization of the grain boundaries. For example, Larsen and Adams [3, 4] proposed a method to extract the grain-boundary area per unit volume (S_v) as a function of grain boundary plane orientation (n_A) and lattice misorientation across the grain boundary (Δg) (cf. **Equation 3.1**).

$$S_v = f(\Delta g, n_A) \qquad 3.1$$

It is required to express the distribution of grain boundary planes in a coordinate system embedded in the crystal lattice, which is called the misorientation frame and represents the misorientation located in the fundamental zone. To apply this method, it is necessary to measure many grain boundary trace angles and lengths, which may be observed from a single section plane. The collected traces should statistically represent the entire population of grain boundary planes, and should be randomly chosen with no orientation bias for each grain boundary type. In other words, this method is valid when no strong texture is present [3, 4].

When a single section plane is large enough to include multiple bi-crystals of misorientation Δg, then each observed boundary between two neighboring grains represents a unique trace of a grain boundary associated with Δg. The normal vector to the grain boundary plane must be perpendicular to the observed grain boundary trace. This provides partial information about the orientation of the grain boundary plane. The proposed stereology technique estimates the **Equation 3.1** by piecing together this partial information from numerous observed traces. For more detailed explanations about this technique, one may refer to the original papers [3-5].

In similar studies, it has been reported that a reasonable estimation of the grain boundary distribution as a function of five macroscopic parameters can be obtained by observations from single 2D section using the stereological technique in $SrTiO_3$ [6], alumina [7] and $MgAl_2O_4$ (spinel) [8]. **Figure 3.2** shows an example of the grain boundary plane distribution for Σ3 grain boundaries in a Ni based superalloy, determined from stereology and compared with the results determined from 3D analysis by serial sectioning technique [9].

3.3. Atom Probe Tomography

Atom Probe Tomography (APT), which is based on mass-spectroscopy, is a high resolution 3D characterization technique for identification of individual atoms. Historically, this technique was developed over 40 years ago and was mainly applied to high-conductivity specimens. However, advances in both sample preparation techniques and atom probe design have made it increasingly

applicable to lower-conductivity specimens. APT is also a chemical analysis tool which allows the detection of the chemical composition of each atom [10].

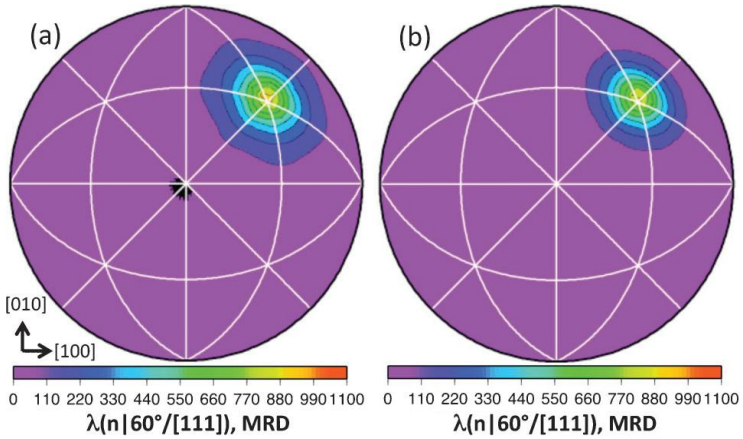

Figure 3.2 Grain boundary plane distribution for Σ3 grain boundaries plotted on a stereographic projection, (a) determined from stereology; (b) determined from three-dimensional analysis [9].

APT has evolved from an earlier technique known as Field Ion Microscopy (FIM), pioneered by Prof. E. W. Müller (1951). In the FIM a positive voltage is applied to the cryogenically cooled needle-shaped specimen in an ultra-high vacuum system. A trace of an imaging gas, typically 10^{-3} Pa of neon or helium, is introduced into the system with a base pressure of less than 2×10^{-8} Pa. When the high electric field is applied, the image gas atoms close to the tip of the specimen become polarized. These atoms are then attracted to the specimen while losing their kinetic energy by performing a series of collisions and finally become thermally accommodated to the cryogenic temperature. These image gas atoms are then ionized and the resulting positive ions are radially repelled from the positively-charged specimen towards the phosphor screen on which a highly magnified image of the tip of the specimen is formed (cf. **Figure 3.3**). This technique produced the first images of individual atoms in a tungsten specimen [10-12].

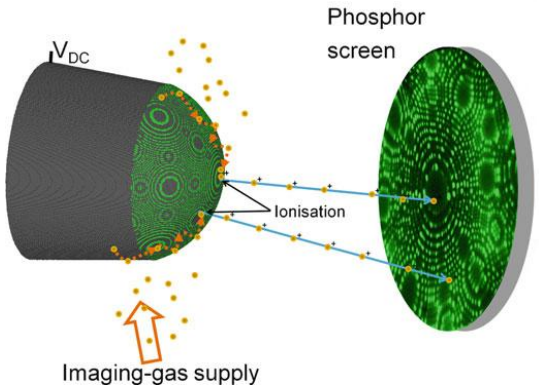

Figure 3.3 Schematic representation of the principles of the Filed Ion Microscope (FIM) [12].

The conventional Atom Probe Tomography (APT) is made when a mass spectrometer is integrated into the FIM. Similar to FIM, the sample for APT is prepared in the form of a very sharp needle with a tip radius of 20-100 nm. Fabrication of this needle-shaped specimen can be performed either by the traditional electropolishing or with the Focused Ion Beam (FIB) instruments, often combined with scanning electron microscope facilities in dual-beam systems. The tip is cooled down to 50-60 K and is biased at high DC voltage ranging from 5 to 20 kV [10].

The latest generation atom probes feature a local electrode (a funnel-shaped aperture) in close proximity to the standard needle-shaped specimen, as shown in **Figure 3.4**. Lower-amplitude standing and pulse voltages are the main advantages of the local electrode. This enables the use of voltage pulse generators with significantly higher pulse repetition rates (200 kHz) and faster position-sensitive detectors, which significantly reduces the data acquisition time. Typical acquisition rates in the local electrode atom probe are 5 to 10×10^6 ions per hour. The sample volume typically contains 10^6 to 3×10^7 atoms and datasets containing over 10^8 atoms have been collected [10, 13].

The atom probe tomography involves the controlled removal of atoms from the surface of the specimen by laser or voltage pulsing. The removal of the surface atoms due to the high electrostatic field is called field evaporation. These atoms are then imaged and analyzed with a time-of-flight (TOF) mass spectrometer, which provides their chemical identity. The extracted ions are projected onto a position-sensitive detector for recording their location, which enables the reconstruction of their original position on the tip. A 3D view of the sample can be reconstructed by repeating the sequence of progressively removing atoms from the surface and recording and analyzing them with the detector. An example of such a 3D microstructure is represented in **Figure 3.5**. [11, 12, 14, 15].

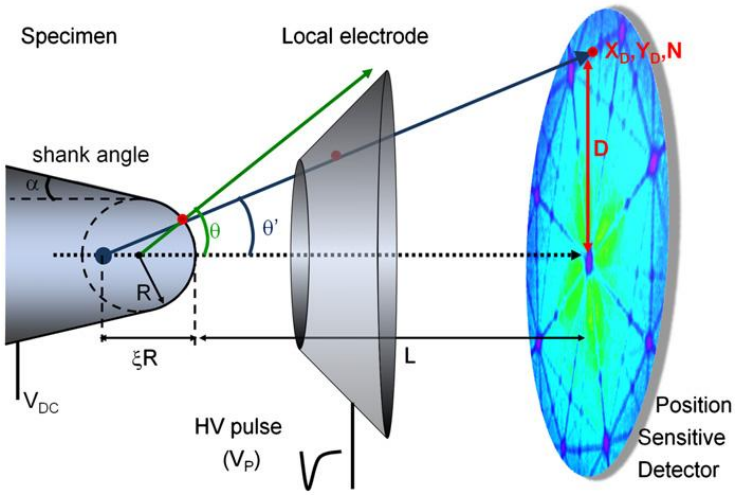

Figure 3.4 Schematic diagram of a Local Electrode Atom Probe (LEAP) with voltage pulsing mode of field evaporation [15].

Analyses of the resolution in atom probe tomography demonstrate that it is routinely below 0.2 nm in the lateral x-y direction. The spatial resolution in depth direction is estimated from the position in the evaporation sequence taking into account the detection efficiency of the mass spectrometer and the atomic density of the material under analysis. The spatial resolution in depth direction is below 0.05 nm for some materials. APT has the highest spatial resolution of any microanalysis technique which provides a unique opportunity to study the chemical clustering and 3D distributions of atoms with atomic resolution, although the resolution is not enough to obtain crystallographic information [10, 13].

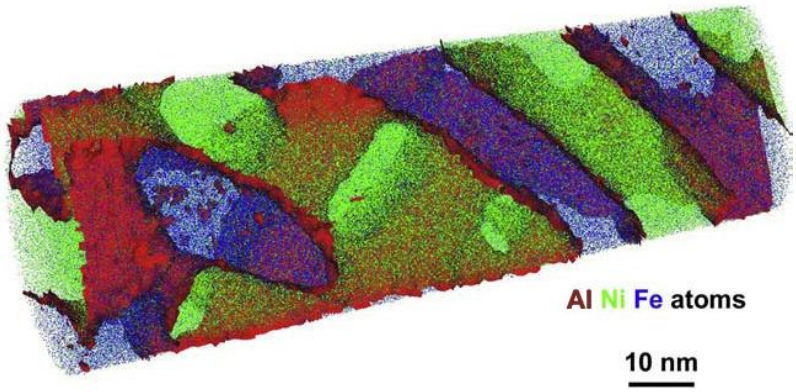

Figure 3.5 APT image of 26% Al in an iron-based superalloy [11].

3.4. X-Ray Tomography

X-ray tomography is a nondestructive technique, which produces 3D representations of the interior features of objects using x-ray irradiation. In traditional radiography, a huge amount of information is projected in a 2D plane which makes it very difficult to analyze the microstructural features along the thickness of the sample. X-ray tomography combines the information of many radiographs taken with different angles of the sample in front of the detector and reconstructs the 3D structure.

Figure 3.6 shows the basic principles of X-ray tomography, whereby the specimen is placed in the trajectory of an X-ray beam. When the X-rays hit the sample, depending on the absorption coefficient, part of the X-rays is absorbed and part of it is transmitted, which is then recorded by a detector. The absorption coefficient depends not only on the energy of the X-ray, but also on the density of the material and the atomic number. The difference of the X-ray absorption coefficients between the various microstructural features present in the material provides the contrast in the radiograph. During the measurement, the sample is rotated over 180° or 360° and several hundreds of radiographs are collected. If the angular step between the radiographs is small enough it is possible to reconstruct the 3D volume with an appropriate algorithm based on the filtered back-projection [16, 17].

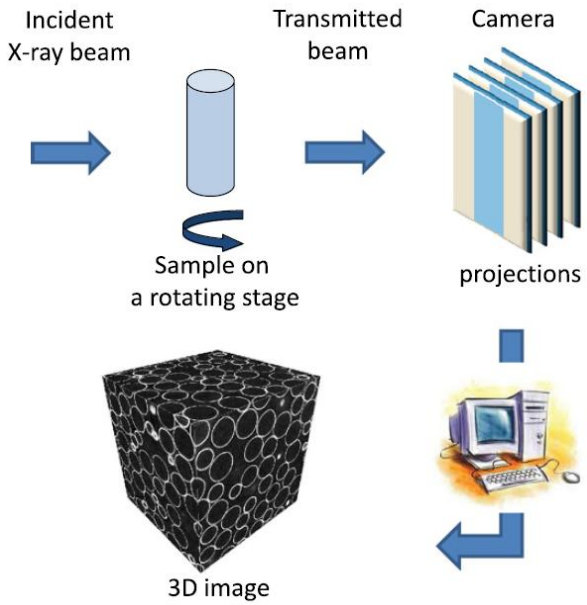

Figure 3.6 Basic principles of X-ray tomography technique [17].

There are two types of X-ray tomography: The laboratory tomography where the X-ray beam is divergent and the synchrotron tomography where the X-ray beam is parallel (cf. **Figure 3.7**). The difference in the X-ray geometry in these two techniques results in different resolutions. With the diverging X-ray geometry the spatial resolution varies from a few millimeters down to one micron, whereas for the synchrotron tomography the spatial resolution varies between 40 and 0.5 µm. The typical acquisition time to obtain a 3D volume of 1024 × 1024 × 1024 voxels with the laboratory technique is approximately 15 to 30 minutes. The required time to obtain the same 3D volume with the synchrotron technique is of the order of a few minutes or even less than 1 s with fast cameras [16].

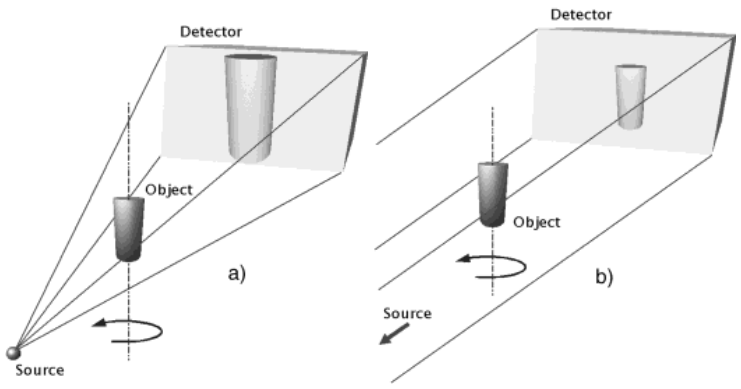

Figure 3.7 Schematic representation of the X-ray tomography techniques. (a) laboratory X-ray tomography with a diverging beam, and (b) synchrotron tomography with a parallel beam [16].

X-ray tomography is now a conventional characterization technique in material science, which allows better understanding of physical mechanisms for a variety of materials in various loading conditions or thermal history. Examples of applications of X-ray tomography are the 3D characterization of metallic foams and porous materials [18], 3D morphology of graphite in cast iron [19], 3D morphology of two phase materials [20] and grain boundary imaging [16]. Furthermore, X-ray tomography can be performed in situ when the materials are subjected to heat treatment or mechanical testing at room temperature or above. 3D characterization of the solidification process of different alloys, alloys in the semi-solid state (cf. **Figure 3.8**) and damage analysis during tensile test are examples of the in situ application of the technique [16, 17].

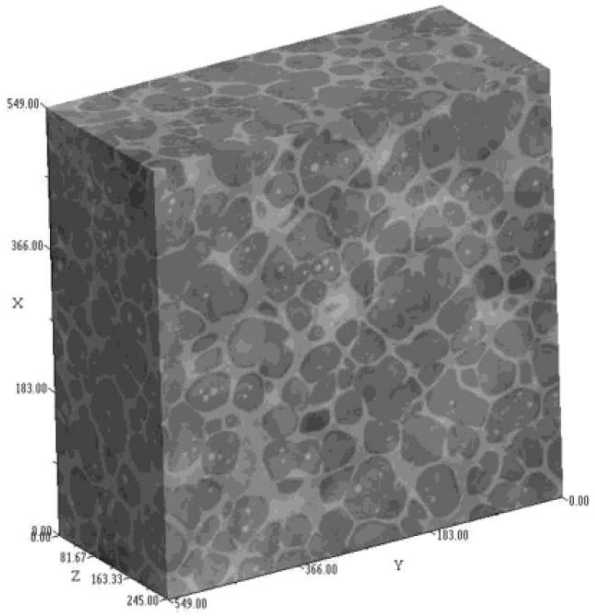

Figure 3.8 3D volume of a matrix and eutectic phase of A357 aluminum alloy, volume = 1mm × 1mm × 0.5 mm [16].

3.5. 3D X-Ray Diffraction

Three-Dimensional X-Ray Diffraction (3DXRD) is a nondestructive technique, which enables a fast acquisition of crystallographic orientation, morphology and phase information from individual elements within millimeter-sized polycrystalline specimens. This technique uses highly penetrating hard X-rays with energies in the range 50-100 keV from a synchrotron source and applies the tomographic reconstruction algorithm for further analysis [21].

Due to the need of a synchrotron source for 3DXRD characterization, there are only a few available 3DXRD set-ups around the word. Currently there are two permanent 3DXRD installations at beamline ID11 at the European Synchrotron Radiation Facility (ESRF) in Grenoble (France) and at beamline 1-ID at the Advanced

Photon Source (APS) in Chicago (USA). There is also one mobile set-up, which has been used at several beamlines at ESRF and the associated technique is known as Diffraction Contrast Tomography (DCT) [22, 23].

Figure 3.9 shows the sketch of the 3DXRD set-up at beamline ID11 at ESRF. The underlying physics of the 3DXRD technique is based on Bragg diffraction. The X-ray energy and sample diameter are chosen so that the incident beam penetrates through the entire sample thickness. Therefore, when the incoming monochromatic beam impinges on the sample, all microstructural elements in the sample volume that fulfill the Bragg condition will generate diffracted beams. During the measurement, the sample is rotated (ω) around the vertical axis (perpendicular to the incoming beam) to probe all the crystallites within the gauge volume [21].

To position the diffracting element within the gauge volume, the diffraction pattern is recorded at a set of semi-transparent 2D detector(s) (L1, L2 in **Figure 3.9**) placed at different distances to the sample. Previously the information was obtained by translating a detector with one screen at different positions. This has recently changed to a so-called 3D detector with 2 screens. The screen near to the sample collects the spatial crystallite shape and orientational information, whereas the screen far away from the sample gives precise orientation and stress information. In order to determine the crystallographic orientation, the position of the spots recorded on the detector from all the ω settings is used [21, 24].

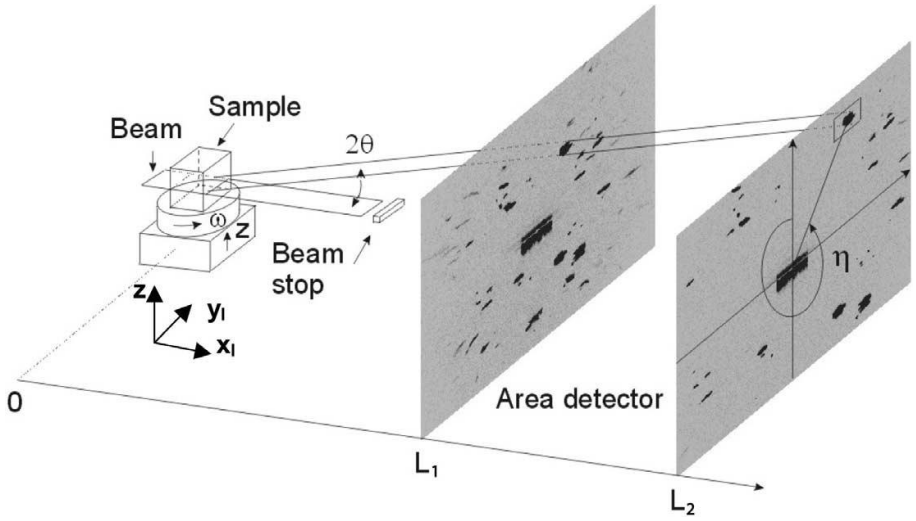

Figure 3.9 Sketch of 3DXRD set-up at ID11 ESRF. Diffraction patterns are acquired on a high-resolution two-dimensional detector positioned at minimum two distances from the sample [21].

Another specialized instrumentation has been developed at the Advanced Photon Source 1-ID beamline of the High-Energy Diffraction Microscopy (HEDM) project [25, 26]. HEDM is based on the 3DXRD diffraction technique and aims at the

structural characterization of polycrystalline bulk materials during thermo mechanical processing. Due to the increasing spread in lattice orientation during deformation, which results in diffraction spot overlap, the area beam of 3DXRD is replaced by a line (flat) beam that illuminates a single sample layer and allows an analysis to be done on a layer-by-layer basis. The HEDM approach features a forward modeling reconstruction, which takes as input the diffraction images, the sample crystallography, the x-ray energy, and a set of geometrical parameters describing the experiment (e.g. the rotation axis-to-detector distances). Each layer in the sample is divided up into a grid composed of equilateral triangles. Diffraction from each grid element is used to generate simulated diffractograms that are compared with the experimental data. Correct orientations will generate many Bragg peaks that pass through experimentally observed diffraction spots. Numerical techniques and a Monte Carlo algorithm are used to determine a best-fit orientation for each grid element and to obtain precise localization of features such as grain boundaries [25-27].

The experimental set-up of X-ray Diffraction Contrast Tomography (DCT) is basically the same as the 3DXRD, however, the DCT only uses the near field detector and the incident beam is limited to only illuminate the central ~10% of the detector. Thereby X-ray tomography (cf. Section 3.4) is observed in a small central part of the detector, whereas the outer regions are used to record the diffracted beams (cf. **Figure 3.10**). Consequently, the DCT enables simultaneous reconstruction of the 3D microstructure using both x-ray tomography and diffraction. Compared to the permanent 3DXRD instruments, the DCT set-up is more robust and currently 3D maps of grain structures with the highest spatial resolution are made in this way [24, 28].

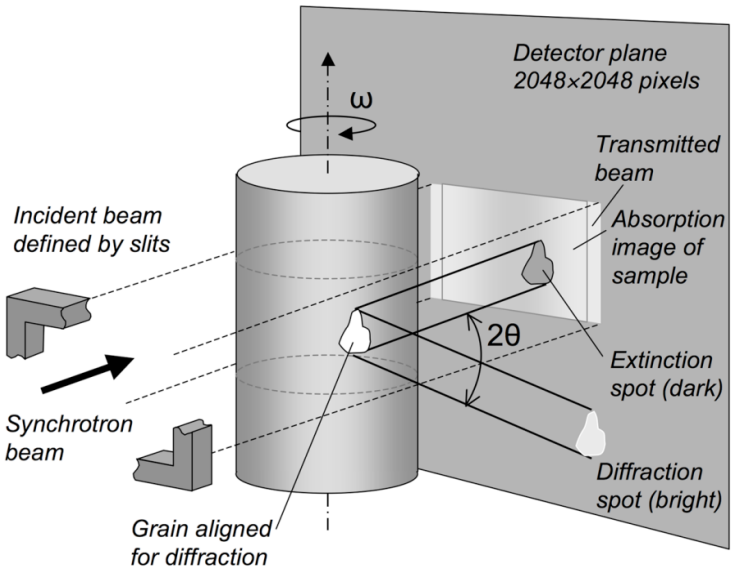

Figure 3.10 Experimental setup for Diffraction Contrast Tomography (DCT) [29].

There are several 3DXRD modes with different time, spatial and angular resolution. Two well-known standard methods are grain center mapping and complete 3D mapping. In the first method, a fast measurement is performed to analyze the average characteristics of each grain such as the center of mass position, volume, average orientation, and an average strain tensor. In contrast, a complete 3D mapping is a slower measurement which provides the exact location of the grain boundaries and the local orientations (like an EBSD map but in 3D) [24].

The ultimate spatial resolution of 3DXRD technique is limited by the X-ray imaging detector resolution to values of about 1 µm. With a high flux beamline a full scan, comprising typically 3600 images and covering a volume of approximately 400^3 voxels (up to 1000 grains) can be acquired in less than 10 minutes [28]. For studies in which capturing the details of the 3D volume is necessary, it is possible to improve the spatial resolution by switching to a modified acquisition geometry, known as topotomography [21]. This technique enables fast imaging of one individual grain with a detector resolution that can be adjusted according to the dimensions of the grain. In this case, diffraction spots from individual grains as small as 70 nm can be detected [21, 29].

The 3DXRD technique is used for different applications. The main static and dynamic applications are listed in **Figure 3.11**. As it can be seen, this method has a wide range of application and can be used for a simple measurement of grains orientation which provides the 3D orientation map (cf. **Figure 3.12**). The other examples of the applications of this technique are the monitoring of dynamics of the individual elements during thermally activated phenomena (e.g. recovery, recrystallization, phase transformation, etc).

The in situ investigation of the diffracted intensity from grains as a function of time while the sample is exposed to stress or temperature provides information of the kinetics of individual structural elements with the highest possible time resolution of seconds or subseconds. A complete three-dimensional microstructural map is obtained with typical time resolutions of tens of minutes or even hours [21].

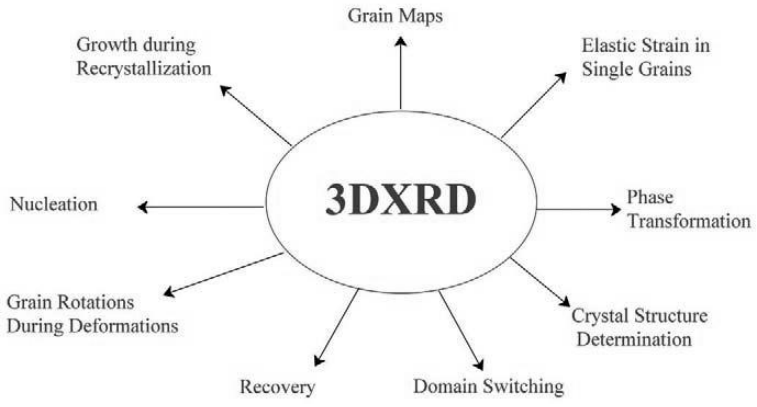

Figure 3.11 Examples of various phenomena in which the 3DXRD technique is used as a characterization technique [24].

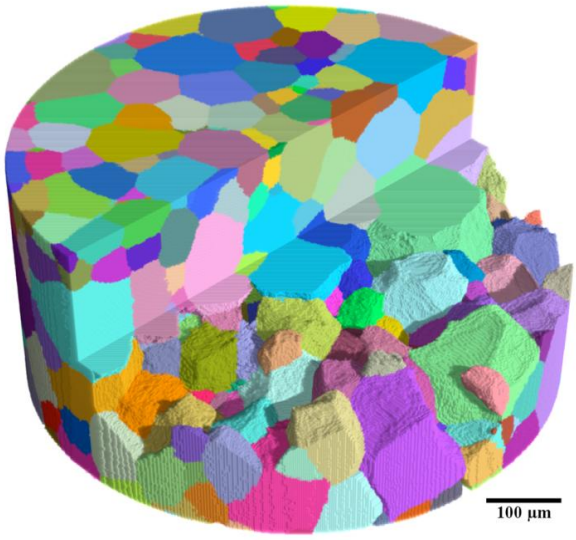

Figure 3.12 Reconstructed microstructure of a beta Ti sample containing 1000 grains collected by the set-up presented in Figure 3.10 [28].

3.6. Serial Sectioning

Serial sectioning has been the most widely used method to acquire three-dimensional data at the macro/microscale of opaque materials. Application of this technique for the evaluation of metallic microstructures was first proposed by DeHoff in 1983 [30]. The serial sectioning technique provides the microstructural parameters that can only be obtained from a three-dimensional representation of the microstructure and not from two-dimensional observations. The number of features per unit volume, connectivity of features, size and spatial distribution information, and the detailed shape of an element of the microstructure are examples of these microstructural parameters [30, 31].

In the serial sectioning technique, the sample is not a representative two-dimensional section, but a series of closely spaced parallel sections, which reveal the third dimension of the microstructure. The usual method for serial sectioning involves the cyclic removal of parallel layers of the sample and then EBSD or imaging of the planar sections [30-32].

The removal of the material for serial sectioning can be performed with different methods: e.g., mechanical polishing, chemical polishing, Focused Ion Beam (FIB) tomography and laser or electrical discharge ablation [33]. Among these method, FIB tomography and manual serial sectioning are the most frequently used techniques, which have been extensively used to generate 3D microstructures of metals. This section provides an overview of the current state-of-the-art for collection of 3D microstructural data with the serial sectioning technique using FIB and mechanical polishing methods.

3.6.1. Focused Ion Beam (FIB) Tomography

This technique is a combination of serial sectioning with a focused ion beam (FIB) and orientation microscopy in a DualBeam™ system, which includes both an electron column and a Ga^+ ion column (cf. **Figure 3.13**). These two independent beams can be focused on one coincident point in space and the sample's surface of interest is positioned at this point. The impact of the ion beam which usually consists of 30 kV ions with the surface of the sample leads to localized sputtering of the target material and can be used to mill into the surface and to remove the atoms by energy and momentum transfer of the ion to the substrate material [34].

Due to the capability of the FIB column to focus highly energetic ions to small spot sizes (5–20 nm) and to perform cuts into the material with a few nanometers width, This technique has been extensively used for the preparation of TEM samples and flat surfaces for two-dimensional microscopic investigations. Furthermore, by cross-section milling with extremely fine resolution, the FIB microscopes can provide serial sections with a precise distance of approximately 10–15nm up to several micrometers [33, 35].

Ion milling is a universally applicable method for creating planar surfaces and has been extensively applied to different metallic alloys, ceramics, polymers, and biological materials. It has been reported that in comparison with most polishing or cutting methods, ion milling is a relatively low damage process. Furthermore, the depth of the damage layer is very small which permits the usage of surface-damage sensitive techniques like EBSD. However, for materials with metastable microstructure both low beam currents and sample cooling are required to prevent modification of the starting microstructure [35-37].

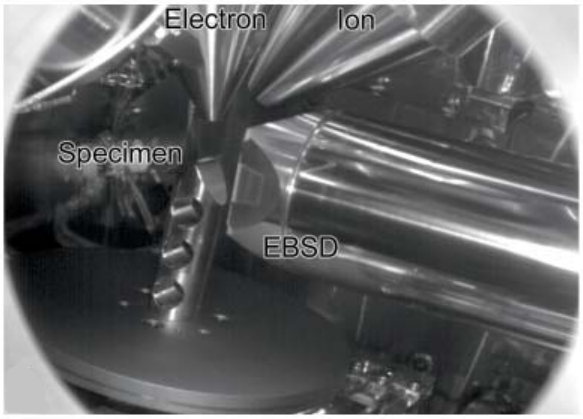

Figure 3.13 Actual view of a DualBeam system showing the sample in the EBSD position, the inserted EBSD detector, the electron beam and the ion beam source [34].

During serial sectioning in a DualBeam microscope, the surface of interest is rotated between the FIB milling and EBSD mapping positions. Schematic representation of this procedure is depicted in **Figure 3.14**. The repetitive movement of the sample between FIB and EBSD positions during serial sectioning is

controlled by a fully automated procedure using the appropriate software control scripts [38]. **Figure 3.15** shows the geometrical relationships between the sample, the electron and the ion beams in a DualBeam microscope. The ion beam is used to prepare the imaging planes (x–y sections) and the images are collected with the scanning electron beam. During the automated serial sectioning procedure, thin layers of the x–y planes are milled with the ion beam and imaged with the electron beam in an alternating process [39].

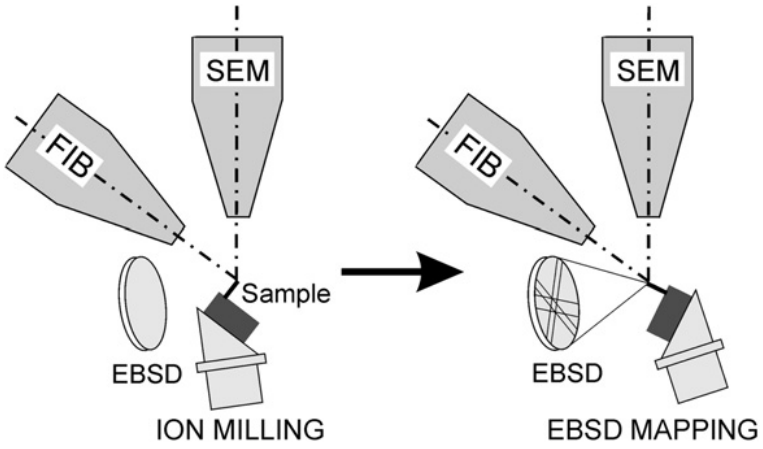

Figure 3.14 Schematic representation of the sample setup in the EBSD-FIB tomography configuration with respect to the FIB/SEM beam directions and phosphor screen [38].

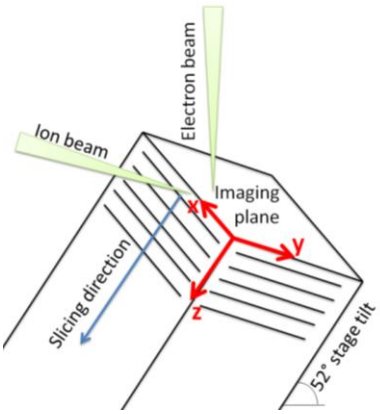

Figure 3.15 The standard sample geometry and its orientation within a DualBeam microscope for a typical serial sectioning experiment.

Serial sectioning by FIB tomography is known as a time consuming operation. For example, using the above mentioned fully operated technique, serial sectioning of a 20×20×20 μm^3 volume of material using a 0.1 µm EBSD step size with a pattern solution rate of 50 frame per second and with 0.1 µm slice thickness (200 slices) requires at least 100 hours of acquisition time [38]. Nevertheless, this combination

of field width and resolution cannot be achieved with any other tomographic instrument [35].

FIB tomography has become very popular in recent years to visualize and to characterize the three-dimensional microstructures. This is mainly because of the capability of this technique to characterize small-scale microstructural features, e.g. subgrains, precipitate structures and multiple-phase microstructures (cf. **Figure 3.16a**), which have a characteristic dimension of approximately 10 µm or smaller, and also the ability to observe grain-level microstructures including the automated collection of crystallographic orientations (cf. **Figure 3.16b**) [35].

3.6.2. Mechanical Polishing

The limited material removal rate by FIB milling has restricted the role of serial sectioning by FIB tomography to the study of nano- and micrometer-scale features in volumes that have dimensions on the order of units-of-micrometers. Serial section by mechanical polishing addresses the issue of volumetric coverage by replacing ion-beam sectioning with mechanical polishing [40].

Serial sectioning by mechanical polishing is performed by two different methods, i.e. semi-automated (also known as manual) [41-43] and fully automated [40, 44, 45]. Obtaining three-dimensional images of the microstructures by the manual serial sectioning technique generally includes the following sequential steps [32]:

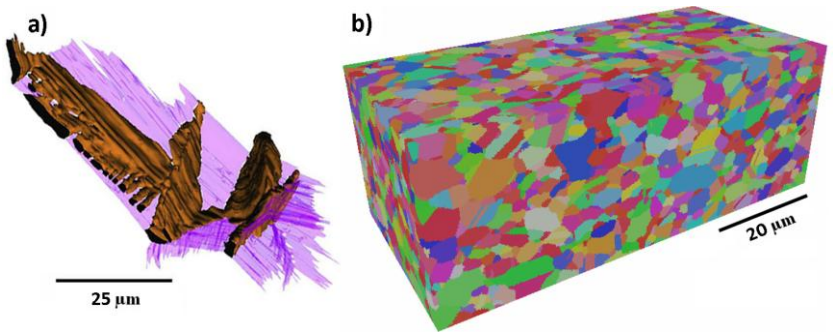

Figure 3.16 Examples of 3D microstructures that have been collected using FIB tomography. a) 3D microstructure of α grain (orange) at the β-β grain boundary (purple) in Ti–4.3Fe–6.7Mo–1.5Al titanium alloy [46], b) 3D reconstruction of IN100 Ni-based superalloy [47].

i) The surface of the sample is prepared with the standard metallographic techniques (i.e. grinding and polishing). One important issue during the serial sectioning by mechanical polishing is to maintain the plan-parallelity of the sections. For this reason and to avoid the inclination of the surface of the material during polishing, an automatic polishing machine is used to polish the samples [48].
ii) Fiducial marks are applied on the surface of the specimen either as indentations (cf. **Figure 3.17**) made by a micro-hardness tester, or fiducial channels (cf. **Figure 3.18**) which are milled into the side of the sample

perpendicular to the sectioning plane using a focused ion beam. These fiducial marks serve two purposes: identification of locations for successive aligning of the sections, and measurement of the thickness of the removed layer in each step. The fiducial channels applied by FIB have the following advantages compared to micro-hardness indentations: (i) the channel has to be applied only once while the indentations should be repeated after several sections, (ii) channels preserve the long-range alignment and the last section can be aligned with the first one while with the indentations each section is aligned with respect to the neighboring section, and (iii) with the channels, depth calibrations can be used for removal of either small or large amounts of material while micro-hardness indentations are limited to the depth of the indent [43, 48, 49].

iii) In the next step the sample is polished to remove the plastically deformed material produced by the hardness indentations and depending on the type of the investigation (optical microscopy, SEM or EBSD) the sample might be etched to reveal the microstructure. It has been reported that filling the fiducial marks with a Ni-Cr coating before this polishing step will considerably preserve the fiducial marks from section to section, and the edges of the fiducial marks maintain sharp for the following measurements [43].

iv) The diagonal lengths of the micro-hardness indentations or the distance between the fiducial channels are measured and recorded for measurement of the thickness of the removed layer.

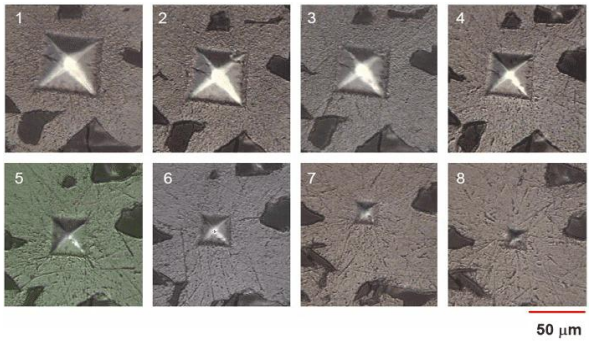

Figure 3.17 Micro-hardness indentations and the progression of their diminishing size with polishing [50].

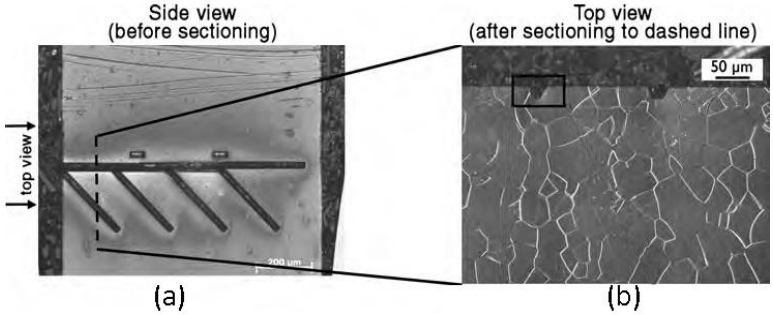

Figure 3.18 Optical micrograph of the fiducial channels made by FIB milling. (a) Side view of the specimen, (b) Normal to the sectioning plane. These channels are used to measure the amount of material removed in each section and to align the sections [49].

v) The next step is to record the two-dimensional microstructure and store it for further reconstruction. The 2D microstructure can be a micrograph captured with an optical microscope or an orientation map obtained via EBSD in a SEM or a combination of both types of images [51]. In the manual method of serial sectioning by mechanical polishing this step is accomplished manually by an operator.
vi) The sample is then polished again to remove the desired thickness from the surface. The amount of the material removed from the surface depends on the microstructural features of interest. With mechanical polishing it is possible to remove approximately between 1 and 5 µm per section. The rate of the removal is a function of the material and polishing parameters (e.g. rotational speed, force and time) [49].
vii) Depending on the desired 3D volume depth, steps IV to VI are repeated. The total number of sections required is defined by the length scale of the features to be reconstructed in 3D. For each section the fiducial marks are used for alignment of the individual 2D images in the stack (cf. **Figure 3.19**) and new fiducial marks are made and recalibrated if the existing ones become too small [32, 49].

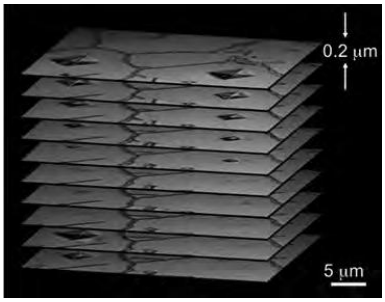

Figure 3.19 Stack of optical micrograph serial sections with the micro-hardness indentations as the fiducial marks [49].

The general procedure of the serial sectioning technique discussed above is depicted in **Figure 3.20**. It is obvious that the rate at which the serial sections can be produced is very low (as low as 10 per day [31]) and a large amount of labor is required to produce a three-dimensional view of part of the microstructure. Moreover, the accuracy to which layer removal can be measured and controlled is typically around 1 µm [44].

Several automated serial sectioning instruments have been developed to address the limitations of the manual serial sectioning technique by increasing the accuracy and the sectioning rate. The first instrument was developed by Alkemper and Voorhees [31, 52, 53] in 2000, which enables the quantification of materials microstructure in 3D using a microtome milling. The microtome blade which is a rotating diamond knife is able to remove sections with the thickness between 1 and 20 μm. The milled surface is an optical-quality surface in soft ductile metals and noncarbon containing materials (carbon will degrade the diamond cutting tool) which do not react adversely with the diamond blade, such as Pb, Sn, Al and Cu alloys [54].

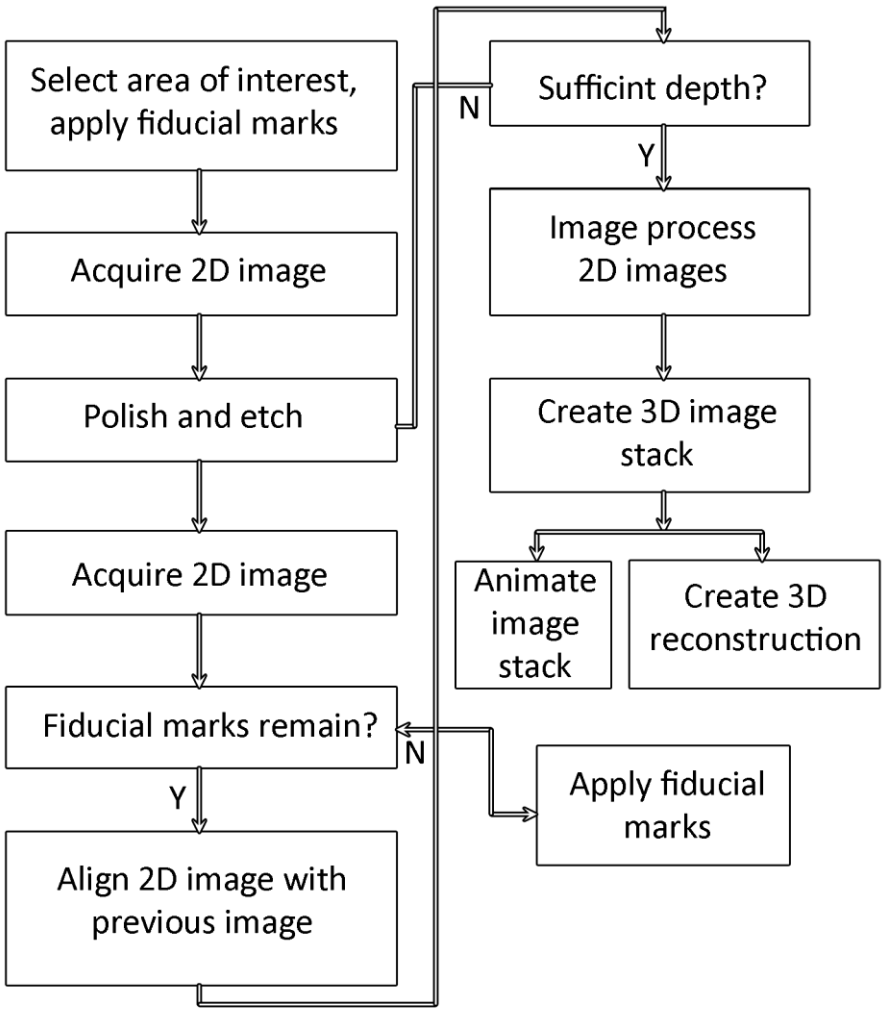

Figure 3.20 General procedure of serial sectioning by mechanical polishing [55].

Figure 3.21 shows the automated serial sectioning instrument developed by Alkemper and Voorhees. The sectioning part of this device is a commercial Reichert-Jung Polycut E micromiller system modified to clean the sample after the micromilling operation. After milling the sample is translated to the microscope which is directly attached to the milling machine. If needed, the sample can be etched in a position between the milling area and the microscope. Movement of the sample and subsequent alignment is accomplished by a single-axis linear translation stage controlled by a linear variable differential transformer (LVDT) to obtain the necessary alignment information [31, 52, 54].

The device of Alkemper and Voorhees measures the thickness of the sections through careful specimen height adjustment with measurement error less than 100 nm for a 5 μm milled surface on an aluminum sample. This set-up allows one to take about 20 sections per hour [31].

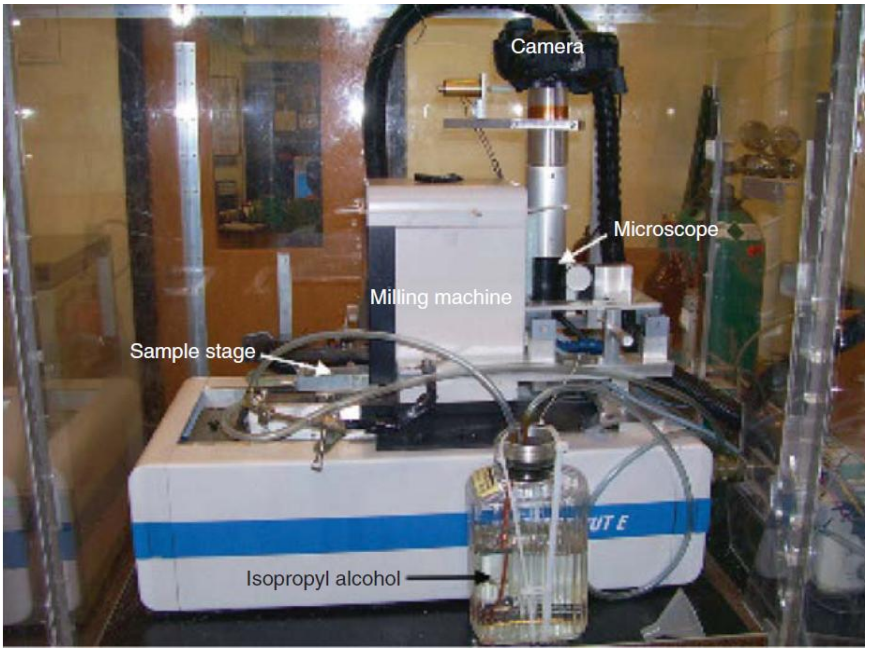

Figure 3.21 General view of the automated serial sectioning device developed by Alkemper and Voorhees [53].

Another automated serial sectioning instrument which is called RoboMet.3D® was developed by Spowart and Mullens [44, 45]. This device is basically composed of three stations, i.e. sectioning, etching/washing/drying, and optical imaging (cf. **Figure 3.22**). A big difference between RoboMet.3D and the micromiller system discussed earlier is the use of a precision mechanical polishing system for removing the material in the RoboMet.3D which makes it applicable for a much broader range of materials. On the other hand and in spite of the micromiller, the stations in RoboMet.3D are physically separated and consequently a six-axis robot arm is required to move the sample between the various stations, and also to hold it during washing, etching, and drying. For a complete automation of the procedure, RoboMet.3D is equipped with a fully automated inverted optical microscope, which performs autofocus and auto-contrast adjustments without human intervention [40, 44, 45].

To minimize the rotational movement of the sample between polishing and imaging steps, the sample is mounted on a custom sample holder. The material removal and the accuracy of section depth in RoboMet.3D are carefully controlled by keeping the variables of the polishing process fixed from section to section. These variables are the polishing time, applied load and rotational speed. It has been claimed that RoboMet.3D can create sections thickness of 0.8 µm with a repeatability as good as 0.03 µm. This device can remove ~0.1 to 10 µm form the material in each section with a sectioning speed up to 20 sections per hour [44]. Although RoboMet.3D was initially developed to reconstruct 3D microstructures base on optical micrographs, it has been also used to collect 3D EBSD information by replacing the inverted optical microscope with a SEM [40].

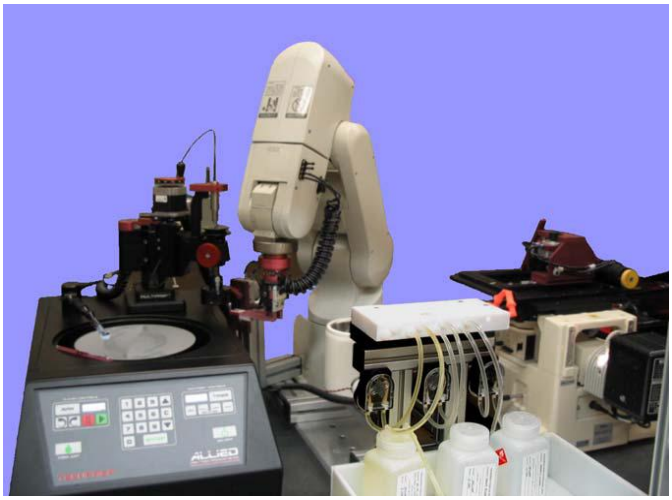

Figure 3.22 Major components of the automated serial sectioning device Robo-Met.3D: precision metallographic polisher (left), six-axis robot arm (center), automatic etching/washing/drying station (lower center) and motorized inverted optical microscope (right) [44].

When the serial sectioning experiment is completed and the stack of 2D data are created using either manual or automated methods the data need to be processed. The main steps of serial sectioning data processing are data registration and segmentation. Data registration (also known as alignment) means to ensure that the spatial registry of each 2D data file is accurate. Considering the fact that the 2D data have been collected from different physical locations, each data file may have to be translated, stretched and rotated. The data alignment is common for most tomographic experiments; however, manually performed experiments usually need more alignment [35].

To perform the data alignment different methods have been proposed. The first method is to align the sections through the use of fiducial marks. These marks not only provide a reference to adjust for any in-plane alignment of the data, but also the relative change of the diagonal of the indent from section to section provides the sectioning depth which is used to correct for the position of the data along the sectioning direction [35, 47, 56]. In a different approach, the internal features of the microstructure are used for the data alignment. For example, Lee et al. [57] have proposed an algorithm to perform the alignment on the serial sectioning data based on the minimization of the average disorientation calculated in the EBSD maps between adjacent layers. Newer techniques employ the mutual information of the neighboring sections for the alignment [58]. It should be noted that the above mentioned techniques are applicable only when the microstructure is relatively isotropic otherwise these methods can introduce systematic errors [35].

When the data alignment is completed and the serial sections are registered, all of the voxels in the 3D volume associated with the specific objects, i.e. grain, precipitate, crack and so on should be identified. This step is referred to as data segmentation and the quantification of the microstructural features is possible only

when this step is done [35]. Additionally, identifying and separating the microstructural features provides the ability to investigate features removed from their surroundings. Grain segmentation is aided by the quantitative orientation information provided by the EBSD maps, i.e. grains are identified as groups of voxels that share a similar orientation. Data processing may be followed by a clean-up procedure to remove the incorrect orientations as well other microstructural features that cannot be correctly identified [59].

Figure 3.23 shows examples of 3D data that have been collected with the techniques mentioned here, i.e. manual serial sectioning, micromiller and Robo-Met3D. **Figure 3.23a** is a 3D reconstructed volume of β-grains in Ti-21S alloy. This volume is 130 × 130 × 140 μm^3, and was produced from 95 serial sections which were collected manually [56]. **Figure 3.23b** shows the grains that are completely contained within the analyzed volume and do not intersect the edges of the box. **Figure 3.23c** represents the reconstructed microstructure of dendrite arms based upon 60 sections spaced 2 µm apart from each other collected using the micromiller device developed by Alkemper and Voorhees [60]. A unique grain color map of the 3D microstructure of an IN100 superalloy reconstructed from the serial sections collected by the Robo-Met.3D [40] is shown in **Figure 3.23c**. This data set contains 15 sections that have an average spacing of approximately 1 µm.

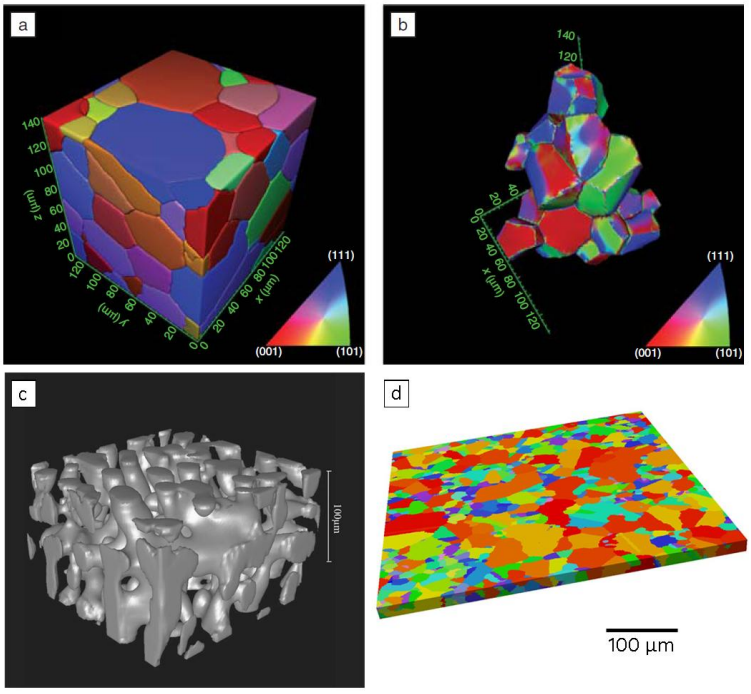

Figure 3.23 Examples of 3D reconstructed microstructures, (a) 3D reconstructed volume of β-grains in Ti-21S alloy from 95 serial sections that were collected manually, (b) the grains which are completely contained within the analyzed volume [56], (c) Reconstructed dendritic structure [60], and (d) Unique grain color map of the 3D microstructure of IN100 superalloy reconstructed from the serial sections collected by the Robo-Met.3Dsystem [40].

Figure 3.24 and **Figure 3.25** summarize and compare the length scale application and the spatial resolution of the 3D characterization techniques mentioned in this chapter. The Transmission Electron Microscopy (TEM) tomography technique [61], also appearing in **Figure 3.25**, is another 3D characterization technique, which has not been used as much as the other techniques. In TEM tomography a series of 2D TEM images are recorded to compute the 3D reconstruction of the object under investigation. The 2D images are recorded at different tilt angles over a wide angular range (±70°) with small angular increments. With an appropriate algorithm, the 2D projections at different tilt angles are used to reconstruct the 3D volume with nanometer scale resolution [62].

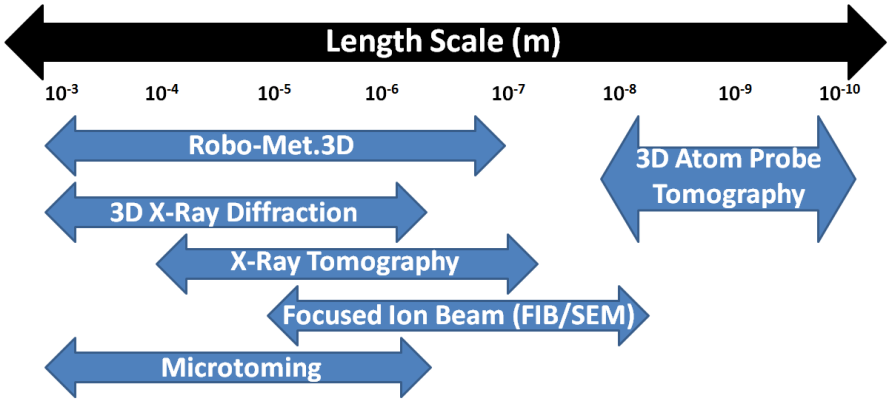

Figure 3.24 Characterization techniques discussed in this chapter as a function of length scale.

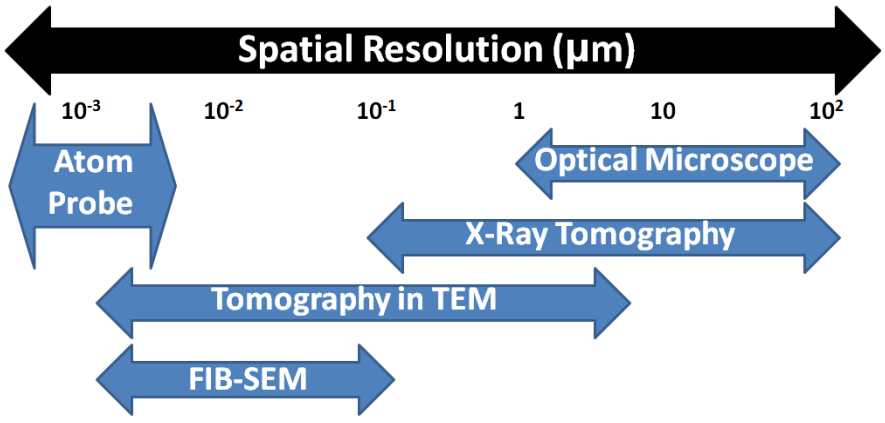

Figure 3.25 Approximate spatial resolution of some 3D characterization techniques discussed in this chapter.

3.7. References

1. Howard, V. and M. Reed, *Unbiased Stereology: Three-Dimensional Measurement in Microscopy*. Second ed. 2005: Taylor & Francis.
2. Liu, G., *Stereology in Materials Science.* Chinese Journal of Metal Science and Technology, 1990. **6**: p. 244-249.
3. Larsen, R.J. and B.L. Adams, *New stereology for the recovery of grain-boundary plane distributions in the crystal frame.* Metallurgical and Materials Transactions a-Physical Metallurgy and Materials Science, 2004. **35A**(7): p. 1991-1998.
4. Larsen, R.J. and B.L. Adams, *Stereology for recovering grain boundary plane distributions in the crystal frame*, in *Textures of Materials, Pts 1 and 2*, D.N. Lee, Editor. 2002. p. 125-129.
5. Adams, B.L., *DESCRIPTION OF THE INTERCRYSTALLINE STRUCTURE DISTRIBUTION IN POLYCRYSTALLINE MATERIALS.* Metallurgical Transactions a-Physical Metallurgy and Materials Science, 1986. **17**(12): p. 2199-2207.
6. Saylor, D.M., et al., *Measuring the five-parameter grain-boundary distribution from observations of planar sections.* Metallurgical and Materials Transactions a-Physical Metallurgy and Materials Science, 2004. **35A**(7): p. 1981-1989.
7. Saylor, D.M., et al., *Distribution of grain boundaries in aluminum as a function of five macroscopic parameters.* Acta Materialia, 2004. **52**(12): p. 3649-3655.
8. Miller, H.M., et al., *Crystallographic distribution of internal interfaces in spinel polycrystals*, in *Recrystallization and Grain Growth, Pts 1 and 2*, B. Bacroix, et al., Editors. 2004. p. 783-788.
9. Rohrer, G.S., et al., *Deriving grain boundary character distributions and relative grain boundary energies from three-dimensional EBSD data.* Materials Science and Technology, 2010. **26**(6): p. 661-669.
10. Miller, M.K., *Atom Probe Tomography*, in *Handbook of Microscopy for Nanotechnology*, N. Yao and Z.L. Wang, Editors. 2005, Kluwer Academic Publisher. p. 227-246.
11. Miller, M.K. and R.G. Forbes, *Atom probe tomography.* Materials Characterization, 2009. **60**(6): p. 461-469.
12. Gault, B., et al., *Atom Probe Microscopy*. 2012: Springer.
13. Miller, M.K., et al., *The future of atom probe tomography.* Materials Today, 2012. **15**(4): p. 158-165.
14. Cerezo, A., et al., *Atom probe tomography today.* Materials Today, 2007. **10**(12): p. 36-42.
15. Gault, B., et al., *Dynamic reconstruction for atom probe tomography.* Ultramicroscopy, 2011. **111**(11): p. 1619-1624.
16. Maire, E., et al., *On the application of X-ray microtomography in the field of materials science.* Advanced Engineering Materials, 2001. **3**(8): p. 539-546.
17. Salvo, L., et al., *3D imaging in material science: Application of X-ray tomography.* Comptes Rendus Physique, 2010. **11**(9-10): p. 641-649.

18. Bock, J. and A.M. Jacobi, *Geometric classification of open-cell metal foams using X-ray micro-computed tomography.* Materials Characterization, 2013. **75**(0): p. 35-43.
19. Ghodrat, S., *Thermo-Mechanical Fatigue of Compacted Graphite Iron in Diesel Engine Components*. 2013.
20. Yazzie, K.E., et al., *Multiscale microstructural characterization of Sn-rich alloys by three dimensional (3D) X-ray synchrotron tomography and focused ion beam (FIB) tomography.* Materials Characterization, 2012. **70**(0): p. 33-41.
21. Jensen, D.J., et al., *X-ray microscopy in four dimensions.* Materials Today, 2006. **9**(1–2): p. 18-25.
22. Liu, W.J., et al., *The three-dimensional X-ray crystal microscope: A new tool for materials characterization.* Metallurgical and Materials Transactions a-Physical Metallurgy and Materials Science, 2004. **35A**(7): p. 1963-1967.
23. Poulsen, H.F., et al., *4D characterization od metals by 3DXRD*, in *The 31st Risø International Symposium on Materials Science: Challenges in materials science and possibilities in 3D and 4D characterization techniques*, N. Hansen, et al., Editors. 2010: Risø National Laboratory for Sustainable Energy, Technical University of Denmark, 2010. p. 101-119.
24. Jensen, D.J. and H.F. Poulsen, *The three dimensional X-ray diffraction technique.* Materials Characterization, 2012. **72**(0): p. 1-7.
25. Suter, R.M., et al., *Forward modeling method for microstructure reconstruction using x-ray diffraction microscopy: Single-crystal verification.* Review of Scientific Instruments, 2006. **77**(12): p. 123905.
26. Hefferan, C.M., et al., *Tests of microstructure reconstruction by forward modeling of high energy X-ray diffraction microscopy data.* Powder Diffraction, 2010. **25**(Special Issue 02): p. 132-137.
27. Rollett, A.D. and K. Barmak, *Orientation Mapping*, in *Physical Metallurgy (Fifth Edition)*, D.E.L. Hono, Editor. 2014, Elsevier: Oxford. p. 1113-1141.
28. Ludwig, W., et al., *Characterization of Polycrystalline Materials Using Synchrotron X-ray Imaging and Diffraction Techniques.* Jom, 2010. **62**(12): p. 22-28.
29. Ludwig, W., et al., *New opportunities for 3D materials science of polycrystalline materials at the micrometre lengthscale by combined use of X-ray diffraction and X-ray imaging.* Materials Science and Engineering a-Structural Materials Properties Microstructure and Processing, 2009. **524**(1-2): p. 69-76.
30. DeHoff, R.T., *Quantitative serial sectioning analysis: preview.* Journal of Microscopy, 1983. **131**: p. 259-263.
31. Alkemper, J. and P.W. Voorhees, *Quantitative serial sectioning analysis.* Journal of Microscopy-Oxford, 2001. **201**: p. 388-394.
32. Dinnis, C.M., A.K. Dahle, and J.A. Taylor, *Three-dimensional analysis of eutectic grains in hypoeutectic Al-Si alloys.* Materials Science and Engineering a-Structural Materials Properties Microstructure and Processing, 2005. **392**(1-2): p. 440-448.
33. Zaefferer, S. and S. Wright, *Three-Dimensional Orientation Microscopy by Serial Sectioning and EBSD-Based Orientation Mapping in a FIB-SEM*, in *Electron Backscatter Diffraction in Materials Science*, A.J. Schwartz, et al.,

Editors. 2009, Springer US. p. 109-122.
34. Mulders, J.J.L. and A. Gholinia, *Three-Dimensional Crystallographic Analysis Beyond EBSD Mapping: The Next Dimension.* Microscopy Today, 2006: p. 34-37.
35. Uchic, M.D., *Serial Sectioning Methods for Generating 3D Characterization Data of Grainand Precipitate-Scale Microstructures*, in *Computational Methods for Microstructure-Property Relationships*, S. Ghosh and D. Dimiduk, Editors. 2011, Springer US. p. 31-52.
36. Zaefferer, S., S.I. Wright, and D. Raabe, *Three-dimensional orientation microscopy in a focused ion beam-scanning electron microscope: A new dimension of microstructure characterization.* Metallurgical and Materials Transactions a-Physical Metallurgy and Materials Science, 2008. **39A**(2): p. 374-389.
37. Groeber, M.A., et al., *3D reconstruction and characterization of polycrystalline microstructures using a FIB–SEM system.* Materials Characterization, 2006. **57**(4–5): p. 259-273.
38. Xu, W., et al., *Techniques for generating 3-D EBSD microstructures by FIB tomography.* Materials Characterization, 2007. **58**(10): p. 961-967.
39. Holzer, L., et al., *FIB-Nanotomography of particulate systems - Part I: Particle shape and topology of interfaces.* Journal of the American Ceramic Society, 2006. **89**(8): p. 2577-2585.
40. Uchic, M., et al., *An Automated Multi-Modal Serial Sectioning System for Characterization of Grain-Scale Microstructures in Engineering Materials*. Proceedings of the 1st International Conference on 3d Materials Science, ed. M. DeGraef, et al. 2012. 195-202.
41. Kral, M.V., et al., *Three-dimensional analysis of microstructures.* Materials Characterization, 2000. **45**(1): p. 17-23.
42. Mangan, M.A., P.D. Lauren, and G.J. Shiflet, *Three-dimensional reconstruction of Widmanstatten plates in Fe-12.3Mn-0.8C.* Journal of Microscopy-Oxford, 1997. **188**: p. 36-41.
43. Spanos, G., et al., *3D characterization of microstructures in metallic systems by serial sectioning*, in *The 31st Risø International Symposium on Materials Science: Challenges in materials science and possibilities in 3D and 4D characterization techniques*, N. Hansen, et al., Editors. 2010: Risø National Laboratory for Sustainable Energy, Technical University of Denmark, 2010. p. 159-170.
44. Spowart, J.E., *Automated serial sectioning for 3-D analysis of microstructures.* Scripta Materialia, 2006. **55**(1): p. 5-10.
45. Spowart, J.E., H.M. Mullens, and B.T. Puchala, *Collecting and analyzing microstructures in three dimensions: A fully automated approach.* Jom-Journal of the Minerals Metals & Materials Society, 2003. **55**(10): p. 35-37.
46. Sharma, H., et al., *Three-dimensional analysis of microstructures in titanium.* Acta Materialia, 2010. **58**(7): p. 2399-2407.
47. Groeber, M., et al., *A framework for automated analysis and simulation of 3D polycrystalline microstructures.: Part 1: Statistical characterization.* Acta Materialia, 2008. **56**(6): p. 1257-1273.
48. Li, M.S., et al., *Serial sectioning method in the construction of 3-D microstructures for particle-reinforced MMCs.* Materials Characterization,

1998. **41**(2-3): p. 81-95.
49. Spanos, G., et al., *Three-Dimensional Microstructure Representation*, in *ASM Handbook, Volume 22B, Metals Process Simulation*, D.U. Furrer and S.L. Semiatin, Editors. 2010, ASM International. p. 100-114.
50. Wunsch, B. and N. Chawla, *Serial sectioning for 3D visualization and modeling of SiC particle reinforced aluminum composites.* TMS Outstanding Student Paper Contest Winner, 2003.
51. Deal, A., et al., *3D Investigation of Cracking Behavior in a Ni Superalloy*. Proceedings of the 1st International Conference on 3d Materials Science, ed. M. DeGraef, et al. 2012, Chichester: John Wiley & Sons. 13-18.
52. Alkemper, J. and P. Voorhees, *3D Material analysis*. 2002, Google Patents.
53. Kammer, D., *Three-Dimensional Analysis and Morphological Characterization of Coarsened Dendritic Microstructures*. 2006, NORTHWESTERN UNIVERSITY.
54. Kammer, D. and P.W. Voorhees, *Analysis of complex microstructures: Serial sectioning and phase-field simulations.* Mrs Bulletin, 2008. **33**(6): p. 603-610.
55. Kral, M.V., et al., *Three-Dimensional Microscopy*, in *ASM Handbook, Volume 9, Metallugraphy and Microstructures*, G.F. VanderVoort, Editor. 2004, Asm International.
56. Spanos, G., et al., *Combining serial sectioning, EBSD analysis, and image-based finite element modeling.* Mrs Bulletin, 2008. **33**(6): p. 597-602.
57. Lee, S.B., A.D. Rollett, and G.S. Rohrer, *Three-dimensional microstructure reconstruction using FIB-OIM*, in *Recrystallization and Grain Growth III, Pts 1 and 2*, S.J.L. Kang, et al., Editors. 2007. p. 915-920.
58. Gulsoy, E.B., J.P. Simmons, and M. De Graef, *Application of joint histogram and mutual information to registration and data fusion problems in serial sectioning microstructure studies.* Scripta Materialia, 2009. **60**(6): p. 381-384.
59. Groeber, M., D. Rowenhorst, and M. Uchic, *Collection, Processing, and Analysis of Three-Dimensional EBSD Data Sets*, in *Electron Backscatter Diffraction in Materials Science*, A.J. Schwartz, et al., Editors. 2009, Springer US. p. 123-137.
60. Alkemper, J. and P.W. Voorhees, *Three-dimensional characterization of dendritic microstructures.* Acta Materialia, 2001. **49**(5): p. 897-902.
61. Liu, H.H., et al., *Three-Dimensional Orientation Mapping in the Transmission Electron Microscope.* Science, 2011. **332**(6031): p. 833-834.
62. Koster, A.J., et al., *Three-dimensional transmission electron microscopy: A novel imaging and characterization technique with nanometer scale resolution for materials science.* Journal of Physical Chemistry B, 2000. **104**(40): p. 9368-9370.

Chapter 4. General Experimental Procedures and Data Processing Techniques

"The best way to show that a stick is crooked is not to argue about it or to spend time denouncing it, but to lay a straight stick alongside it."

Dwight Lyman Moody
quoted by William Backus and Marie Chapian in "Telling Yourself the Truth" (2000), p. 31

4.1. Introduction

This chapter deals with the common experimental procedures employed to reconstruct the three-dimensional microstructure of materials used in the chapters 5 to 7. The experimental procedures explained here include the sample preparation techniques and the details of the EBSD measurements including microscope settings and data collecting parameters. The chemical composition of the materials of this research together with further necessary details about the experimental and processing techniques is explained in the experimental sections of chapter 5 to 7.

The next section of this chapter provides explanation of detailed data processing techniques and algorithms developed to reconstruct the 3D microstructure pertaining to section alignment and data segmentation. Furthermore, the method employed to visualize the 3D data is explained. Verification of the alignment procedure is the subject that will be discussed at the end of this chapter.

4.2. Experimental Procedures

Serial sectioning by mechanical polishing is the general method employed in this work to collect the 2D sections and consequently reconstruct the 3D microstructure. The serial sectioning technique includes consecutive steps of sample preparation and EBSD measurements, which are explained in detail in this section.

4.2.1. Sample Preparation

4.2.1.1. Sample Holder

In order to be able to handle the small samples with dimensions of less than 1 cm, the samples where permanently mounted in a semi-circular steel clamp (**cf. Figure 4.1**). Two holes drilled on the clamp are used to fix the clamp on the pre-tilted EBSD specimen holder. Two removable minor circle segments are used to complete the circular shape of the clamp, which is required to support it in the polishing sample holder during mechanical polishing.

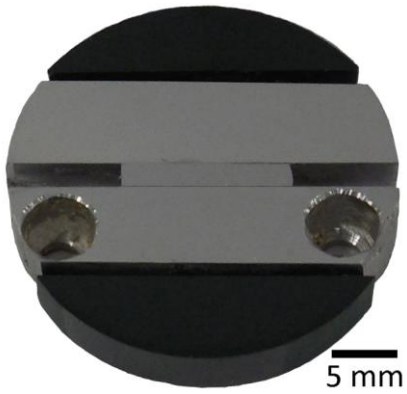

Figure 4.1 A sample mounted in a steel clamp is ready for mechanical polishing followed by EBSD measurement. The circular shape of the clamp is necessary for fitting it in the polisher sample holder.

4.2.1.2. Grinding and Polishing

To prepare the surface of the sample for the first section, the conventional metallographic sample preparation techniques, which include grinding and polishing, were performed. The grinding was carried out using SiC abrasive papers with grit sizes increasing from 80 to 1200. The grinding was followed by 3 and 1 μm diamond suspension polishing. The final step of sample preparation was a fine polishing with OPS solution. OPS (Oxide Polishing Suspension) is a colloidal suspension with colloidal silica particles of approximately 0.04 µm size, as abrasive agent. Long time OPS polishing (approximately 40 minutes) was performed to produce a scratch-free and deformation-free surface ready for EBSD measurement. To remove the colloidal silica particles from the surface, the sample was cleaned in an ultrasonic cleaner with ethanol as the solvent for about 3 minutes.

After each EBSD measurement, the mechanical polishing was performed to remove the desired thickness of the material from the surface of the specimen. This step was carried out only with OPS polishing. As it is crucial to maintain the planparalellity of the specimen surface of two consecutive sections, the polishing was carried out by an automated polishing machine (cf. **Figure 4.2**).

Figure 4.2 The automated polishing machine used for sample preparation. The sample is located in the polishing holder, which rotates in the opposite direction of the rotating disk.

The removal rate of the material was found to be highly dependent on the applied load and rotational speed of the polishing machine. For example with the applied load of 50 kN and rotational speeds of 150 and 200 rpm of sample holder and rotating disk, respectively, a removal rate of approximately 1 μm per minute was obtained.

4.2.1.3. Fiducial Marking

As it was mentioned before, the removal rate of the material from the surface was controlled by polishing parameters, i.e. applied load, rotational speed and polishing time. The precise measurement, however, was carried out using fiducial markers. The fiducial markers were made with a micro-Vickers hardness tester (cf. **Figure 4.3a**) on the surface of the samples. The Vickers indenter has a square-based pyramidal shape with an angle of 136° between opposite faces. Therefore, the indentation depth (H) is equal to one seventh of the average diagonal (D) left by the indenter. The thickness of the removed layer was determined by measuring the precise indent diagonal after each polishing step (cf. **Figure 4.3b**). As the number of the collected sections increases, the size of the indents on the surface continuously decreases. For this reason and before the indents completely disappear, they were renewed by new indentations.

The micro-Vickers indentations were also used to meticulously fix the scan area on subsequent layers for EBSD measurements. Eight indentations on top, bottom, left, right and corners of the scan area were used to mark a grid on the surface of the sample. The center of this zone was considered as the center of the scan area. **Figure 4.4a)** and **b** show a subset of a stack of 17 consecutive sections including 3 indentions at the bottom-right corner of the scan area. **Figure 4.4c** represents the cross-sectional view of the reconstructed volume, which includes the triangular shape of the indentations profile.

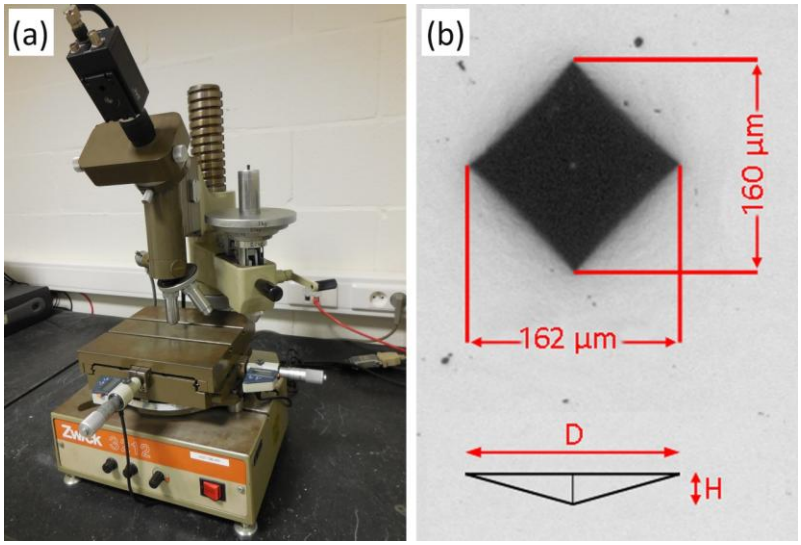

Figure 4.3 (a) The micro-Vickers tester used to mark the fiducial indentations on the surface of the specimens. (b) An example of the indents made on the surface of the samples. Regarding the geometry of the Vickers indenter, the depth of the indentation (H) is equal to D/7, where D is the diagonal of the indent.

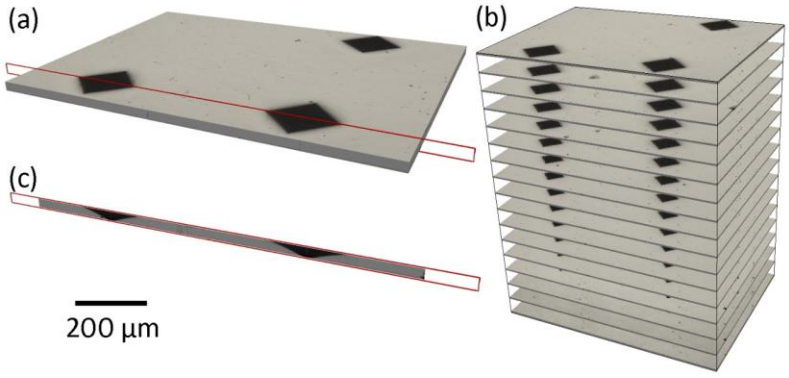

Figure 4.4 (a) Stack of 17 consecutive sections with interlayer distance of 1.5 µm along the Z direction. (b) Same as (a) with expanded distance between the sections for a better visualization of the descending size of the indentations. (c) The cross-sectional view representing the triangular shape of the indentations profile after reconstruction of the volume.

4.2.2. EBSD Measurement

To perform the EBSD measurement the sample was mounted on a 54° pre-tilted specimen holder made of aluminum (cf. **Figure 4.5**). Two screws were used to fix the position of the sample on the holder and to prevent any sliding during the measurement. With a 16° degree tilt of the microscope specimen stage, a total tilt of 70° degree was obtained, which is optimum for the EBSD measurement.

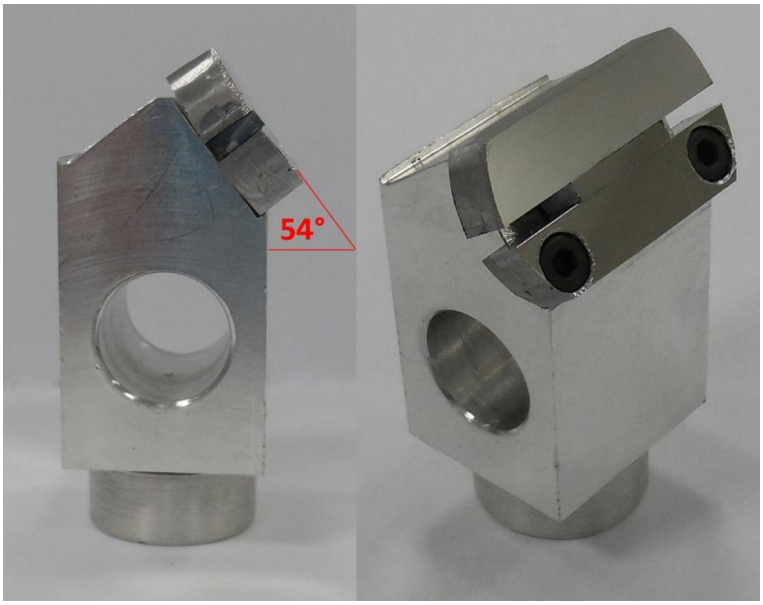

Figure 4.5 The pre-tilted specimen holder for the EBSD measurements. The sample is fixed on the holder with two screws, which prevent any sliding during the measurement.

4.2.2.1. Microscope Settings

A high resolution FEI Quanta^{TM} 450 FEG-SEM (Field Emission Gun-Scanning Electron Microscope) equipped with TSL EBSD camera was employed to perform the EBSD measurements. The microscope was operated in high vacuum mode (chamber pressure = 5.5 e^{-6} Torr) at an accelerating voltage of 20 kV and with electron beam spot size of 5. The EBSD measurements were carried out at a working distance of 16 mm, which was found to be the optimum working distance of the microscope employed in this study. The optimum working distance was experimentally found by capturing the EBSD pattern of a single crystal nickel sample at different working distances, and the one with the best illumination across the whole phosphor screen was selected (cf. **Figure 4.6**). With these adjustments, in the mentioned SEM and EBSD system, an excellent angular resolution of the crystallographic orientation (~ 0.7°) is expected.

The main objective of this research was to reconstruct the 3D microstructure from areas with dimensions of the order of millimeters (e.g. 3×3 mm^2), therefore to cover the largest possible area for the EBSD measurement the SEM was adjusted at low magnifications of 40 or 50 times. It is worth mentioning that due to the steep specimen tilt, the quality of the patterns at the top and bottom of the EBSD map is relatively lower than at the center of the map (i.e. the focal point). Dynamic focus setting has been developed to automatically adjust the focus over the scanning area. However, with such a low magnification and large scanning area, the functionality of the dynamic focusing is limited, which may cause wrong or failed indexation, in particular when the material is deformed or has fine grains. For the studied materials in this work, because of the large grained recrystallized structures, the limit of dynamic focusing did not pose difficulties in indexation.

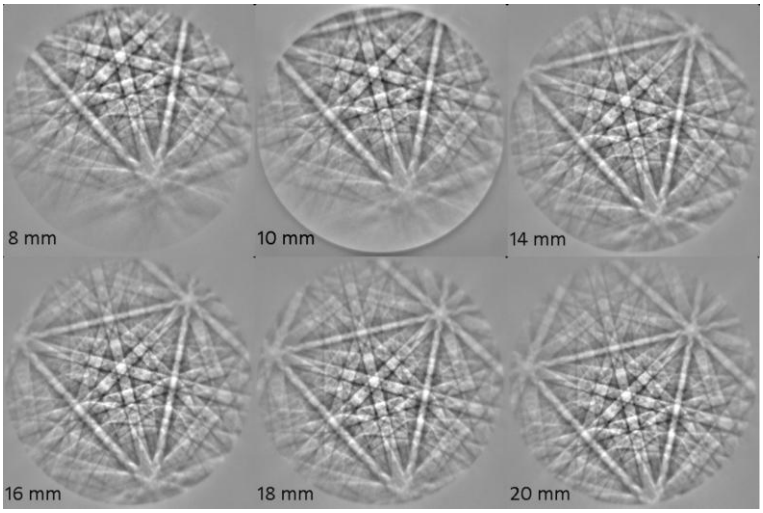

Figure 4.6 EBSD patterns of a single crystal nickel captured at different working distances.

4.2.2.2. Data Collecting Parameters

OIM™ Data Collection software was employed to capture and collect the EBSD patterns. As most of the samples in this study were in a fully recrystallized state, a 4 by 4 binning was found to be the best adjustment of the camera control functions, which ensure both fast and reliable pattern acquisition (with a confidence index (CI) of more than 0.7). By adjusting the other standard camera control functions, i.e. gain, black level and exposure time, a fast pattern acquisition speed of 150-200 fps was reached. The EBSD scans were carried out on a square grid over a large area with a typical dimension of 3 by 3 mm^2. As it was very important to derive the correct curvature of the grain boundary planes in 3D, approximately 10 % of the average grain size of the specimen was selected as the step size of the EBSD scan.

As the materials in this study were single phase iron and nickel with BCC and FCC cubic crystal symmetry, respectively, only one phase was defined as the available phase in each specimen (one of the materials in this research was compacted graphite iron which consists of vermicular graphite particles in a pearlitic matrix, but the crystallography of graphite was not the purpose of this work and it was excluded from the list of the available phases). In order to detect the diffraction bands, a convolution mask of 9 by 9 was selected in the hough transform interface with maximum and minimum number of peaks equal to 7 and 3, respectively. With all the mentioned settings, an EBSD scan of 360,000 pixels on an area of 3 by 3 mm^2, with step size of 5 μm and the pattern acquisition speed of 150 fps, lasted 40 minutes.

4.3. Data Processing

After collecting the required numbers of the 2D EBSD sections, the data were processed by different codes written in MATLAB®. However, preceding this, a cleanup procedure was carried out by the TSL OIM Analysis software. This cleanup method (known as grain dilation) removes the pixel or group of pixels having fewer

members than a Minimum Grain Size (2 pixels in most cases of this research) and replaces their orientation with the orientation of the majority of neighbors that belong to the same grain [1]. After applying the appropriate cleanup method, the scan data was exported as an *ANG* type file, which is in ASCII format and contains the basic data produced during an EBSD scan. The most important information in ANG files used for further data processing are the Euler angles in Bunge notation, the horizontal and vertical coordinates of the pixels in the scan, the image quality parameter (IQ), the confidence index (CI) and Phase ID, which identifies the material phase.

4.3.1. Sections Alignment

In spite of mechanically aligning the specimen before each EBSD scan by the micro-Vickers indentations, the maps may still be slightly misaligned. As explained in the previous chapter (page 68), different methods have been proposed to further optimize the alignment of the serial sectioning data. One generally accepted method is proposed by Lee et al. [2], which is based on the minimization of the average disorientation calculated in the EBSD maps between adjacent layers. This method is generally employed in this work to accurately align the 2D sections and to register them in a global reference frame. To this purpose, it is first assumed that the sections are parallel to each other and there is no rotational misalignment. An iterative algorithm was used to find the location of the minimum misorientation between each two neighboring sections which consists of the following steps:

i- The lower section was kept fixed and the upper section was translated in X and Y directions in a 21 by 21 grid as follows:

x_o - (i×step size) < X < x_o + (i×step size)

y_o - (i×step size) < Y < y_o + (i×step size)
with i = 10

where (x_o , y_o) is the position of the center of the grid. The initial values of (0 , 0) were selected for (x_o , y_o).

ii- For each out of the 21^2 = 441 positions, the average misorientation angle ($\bar{\omega}_{xy}$) between two sections was calculated by averaging out the misorientation angle (ω_i) between each pixel in the upper section and its neighboring pixel in the lower section (cf. **Equation 4.1**).

$$\bar{\omega}_{xy} = \frac{1}{N}\sum_{i=1}^{N} \omega_i \qquad 4.1$$

Where N is the number of pixel pairs in two consecutive sections (only well-indexed pixels with a CI higher than 0.1 are taken into account). The misorientation ω_i between two orientations was calculated according to the well-known method, cf. **Equation 4.2.**

$$\omega = min\left(\cos^{-1}\left(\frac{trace(Sg_1 g_2^{-1}) - 1}{2}\right)\right) \qquad 4.2$$

Where *S* is the crystal symmetry operator (cf. **Table 2.4** in chapter 2) and g_i is the matrix representation of the orientation *i* (cf. **Equation 2.2** in chapter 2).

iii- The position with the minimum average misorientation $\bar{\omega}$ in the 21 × 21 grid (x_{min} , y_{min}) was determined and chosen as the new (x_o , y_o)

iv- The steps i to iii are repeated until the position with the minimum average misorientation was found at the center of the grid. This position was recorded in a table as the displacement to be applied on the upper section.

The above mentioned procedure was performed for each pair of two consecutive sections. **Figure 4.7a** represents the average misorientation between two adjacent sections as a function of their relative position. As it can be seen, there is a well-defined minimum, which is employed to align the sections. **Figure 4.7b** shows the alignment parameters (x and y) for 50 consecutive sections. It was found that the spread in the X direction is 0.35 times less than the spread in the Y direction. These results can be explained by taking into account that the sample for the EBSD measurement is placed in a 70° tilted position (*cos70° = 0.34*). As the tilt axis is parallel to the X direction, it does not influence the resolution in the X direction but decreases the accuracy of positioning the sample in the Y direction. Similar observations have been reported for the alignment of the serial sectioning data obtained by FIB tomography [3].

As the displacement values were calculated with respect to the previous section, they all need to be recalculated with respect to a global reference frame, which was chosen to be the one of the first section. This was done for each section by adding the displacement values of the previous sections to the values of the current section. Finally all the sections were cropped and only the common area of all of them was used for further processing and reconstruction.

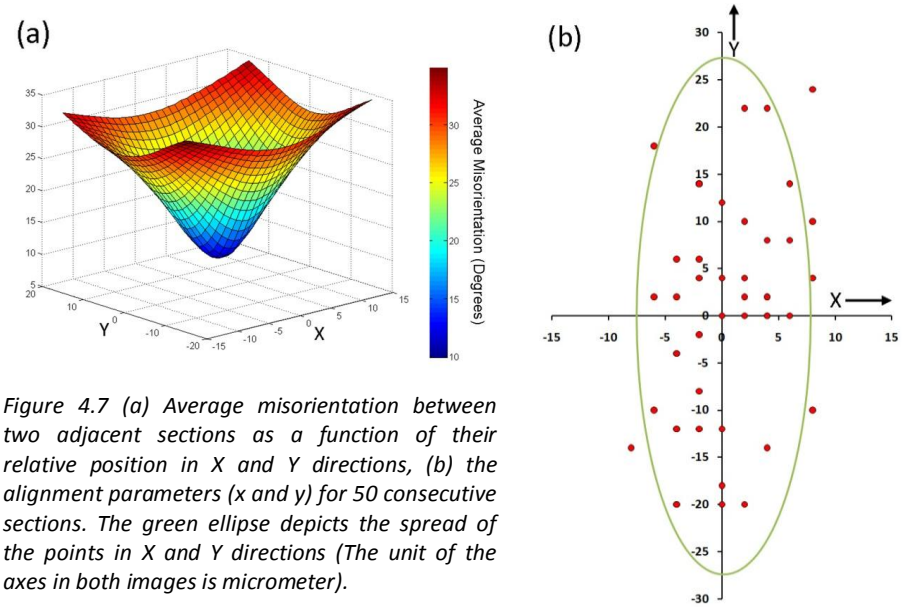

Figure 4.7 (a) Average misorientation between two adjacent sections as a function of their relative position in X and Y directions, (b) the alignment parameters (x and y) for 50 consecutive sections. The green ellipse depicts the spread of the points in X and Y directions (The unit of the axes in both images is micrometer).

4.3.2. Microstructure Reconstruction

To reconstruct and represent the 3D microstructure, it was assumed that each scan point in the 3D volume (henceforth called voxel) is located at the center of a cuboid cell. The borders of the cell are precisely on the half distance between two neighboring voxels. All the voxels are represented in a rectilinear grid in a way that X, Y and Z axis of the grid correspond to the sample axis (RD, TD and ND, respectively), cf. **Figure 4.8**. Microstructural parameters such as IQ and CI, which were directly derived from ANG files were assigned to each cell. Furthermore, integer values representing the grain ID and scalar values for inverse pole figure map colors were calculated for each voxel and were attributed to its corresponding cell. These calculations are explained in the next two sections of this chapter. This information was then written in a file that can be visualized by Paraview® software.

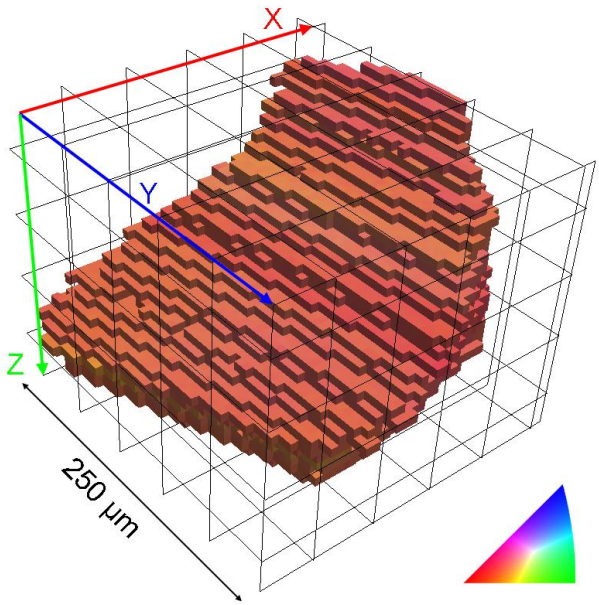

Figure 4.8 Example of a reconstructed grain in 3D. The represented color is based on the ND inverse pole figure colors and the gradient is a result of the orientation gradient inside the grain.

4.3.2.1. Grains Segmentation

After applying the precise alignment on all 2D EBSD sections, another algorithm was employed to identify the grains in the 3D microstructure. The basic principle of the grain segmentation procedure is to merge the voxels, which belong to the same grain and giving them a unique *Grain ID*. To this purpose, the following steps were programmed in a MATLAB® code:

i- The first grain ID is assigned to the first voxel of the 3D volume. This voxel is now called the *Pac-Man* voxel.

ii- The misorientation between the Pac-Man and all surrounding voxels in the 3D volume which do not already have a grain ID is calculated. In general a voxel has 26 surrounding voxels (9 on each of the neighboring sections and 8 in the

same section). However, depending on the position of the voxel in the volume, it may have 7, 11 or 17 surroundings when it is located on the corners, the edges or the faces of the volume, respectively.

iii- If the misorientation angle of a surrounding voxel and the Pac-Man is less than a threshold, that voxel becomes a Pac-Man and receives the same grain ID. As most of the materials in this study were in fully recrystallized state, a threshold of 15° fulfilled the grain segmentation.

iv- Steps ii and iii are repeated for all new Pac-Mans(s) and continued until no more voxel can be joined to the grain.

v- A new grain ID is assigned to another voxel in the volume which does not yet have a grain ID and the steps are repeated from the beginning until all the voxels have a grain ID.

The grouping of neighboring voxels with misorientation less than the threshold makes it possible to consider orientation gradients inside grains. Furthermore, by including the grain ID number in the cells properties of the 3D volume, it is easily possible to select grains and investigate them individually (cf. **Figure 4.8**).

4.3.2.2. IPF Colors Assignment

Inverse Pole Figure (IPF) colors are very good tool to visualize the correlation between crystallographic directions and sample reference directions. The IPF colors were included in the properties of each voxel in the 3D volume based on the RGB color system which consists of three scalar values between 0 and 1. In this system, for example, $(100)^*$ is red, $(010)^*$ is green, $(001)^*$ is blue and $(000)^*$ and $(111)^*$ are black and white, respectively. In order to calculate the IPF color for each voxel, first the orientation matrix (cf. **Equation 2.2**) was derived from its Euler angles. The columns in the orientation matrix represent the directions in the crystal reference frame which are parallel to sample reference directions, RD, TD and ND, respectively. Therefore, to plot a RD-IPF, TD-IPF or ND-IPF map the first, second and third column of the matrix, respectively, is taken into account. Next step is to calculate all 24 symmetric equivalent directions. To this purpose, the desired direction was multiplied by the 24 symmetry operators (cf. **Figure 4.9a**). Among all the 24 equivalent poles, only the one within the fundamental zone (i.e. the pole with its stereographic projection inside the (001), (101) and (111) triangle) (cf. **Figure 4.9b**) is selected for further calculations.

To calculate the RGB color of the selected pole, first the common planes between each two directions of the corners of the fundamental zone are specified. The common plane between (001) and (101), between (101) and (111), and between (111) and (001) were calculated and for simplicity are called plane B, R and G, respectively. The angle between the selected pole and these three planes is called θ_B, θ_R and θ_G, respectively (cf. **Figure 4.10a**). Now, between these three angles if – for example- θ_R has the maximum value, then R=1, G= θ_G/θ_R , B= θ_B/θ_R . The result of this color coding system together with some arbitrary directions is presented in **Figure 4.10b**.

* These brackets do not have a crystallographic meaning.

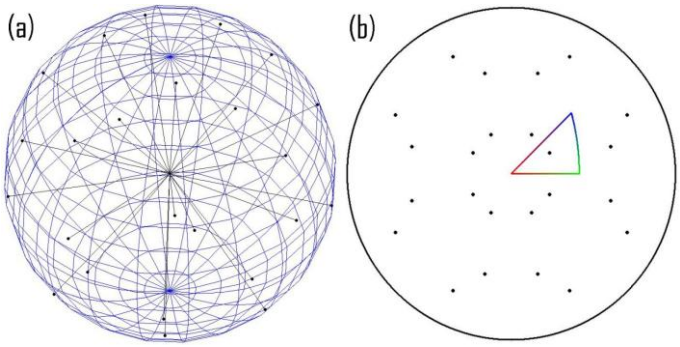

Figure 4.9 (a) 24 symmetric equivalents of an arbitrary pole, (b) the corresponding stereographic projections of the 24 equivalent poles.

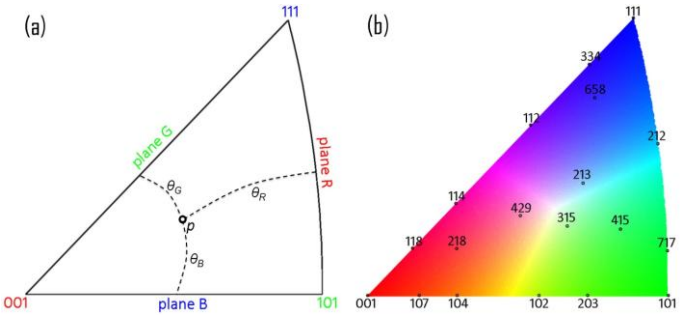

Figure 4.10 (a) Planes and angles used for calculation of RGB colors for an inverse pole figure map representation, (b) The resulting IPF colors with some arbitrary directions.

4.3.2.3. Triangulation (GB fitting)

To extract grain boundary information, the first step was to find the coordinates of the points that are located on the grain boundary plane. In a 2D EBSD map (cf. **Figure 4.11a**), the misorientation angle of each two neighboring pixels (the black dots in **Figure 4.11a**) was used as the criteria to separate low from high angle grain boundaries. In this research grain boundaries are considered as low angle grain boundaries (LAGBs) and high angle grain boundaries (HAGBs) when the misorientation angle across two sides is less vs more than 15 degrees, respectively. If the misorientation between two neighboring pixels (either vertical or horizontal) is more than 15 degrees, a line (which is in fact the trace of the grain boundary plane) is plotted between the two pixels. It is obvious that in this case the grain boundary will be presented by a set of vertical and horizontal lines (cf. **Figure 4.11b**), which is far from the reality. Therefore, a fitting algorithm was used to fit a polynomial function through the points, which are assumed to belong to the same grain boundary. These points (so called grain boundary points) are the midpoint between two pixels with misorientation angle exceeding 15 degrees (red dots in **Figure 4.11a**). To this purpose, a polynomial function was fitted on all grain boundary points between two corresponding triple junctions (the red dots in **Figure 4.11a**). The coordinates of the triple junctions were obtained by the OIM analysis software. The triple junctions were considered as reference points for the fitting algorithm. To have the best fitted curve and specially to avoid the oscillation problem, which may happens with higher order polynomials, the curve fitting was

started with a polynomial of second order (n=2). If the R^2 of fitting was less than 0.95 (after trying different thresholds, this value was found to be the best threshold which results in the best fitted curves on grain boundaries for the recrystallized grains investigated in this study) the curve fitting was repeated with order of n+1, otherwise the polynomial fitting was considered as acceptable. The polynomial between two triple junctions was then sub-divided with specific segment size (usually the same as EBSD step size). The resulting points were considered as new grain boundary points and the connecting lines between them defined the grain boundary trace (cf. **Figure 4.11c**).

Figure 4.12 shows the fitted curves on the all grain boundaries (including LAGBs) of the EBSD map with step size of 10 µm of a silicon steel sample. It can be seen that this curve fitting successfully represents the grain boundary traces.

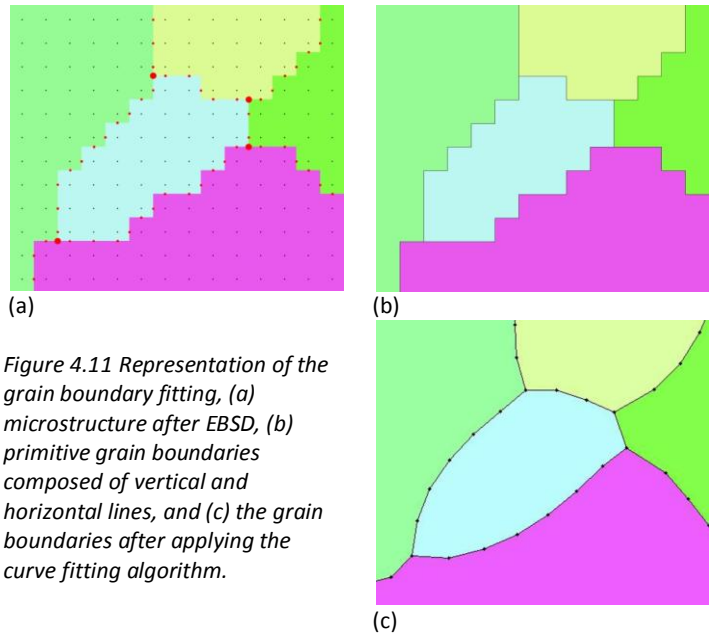

Figure 4.11 Representation of the grain boundary fitting, (a) microstructure after EBSD, (b) primitive grain boundaries composed of vertical and horizontal lines, and (c) the grain boundaries after applying the curve fitting algorithm.

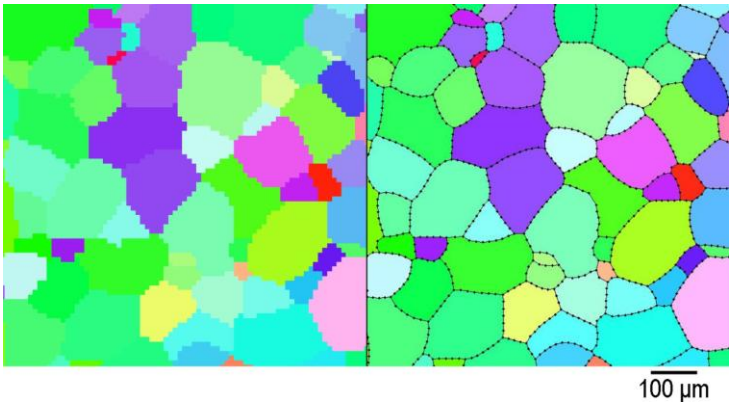

Figure 4.12 Grain boundary curve fitting on the EBSD map of a silicon steel sample. The black dots delineate segments of the polynomial function used for further triangulation.

In order to reconstruct the grain boundary plane, the first step is to match the corresponding triple junctions of two adjacent sections. To this purpose, the three adjacent orientations of a triple junction in one section are compared with the orientations of the triple junctions in the neighboring section. A misorientation threshold of 5° was found to be enough to avoid mis-matching of the triple junctions. In some cases in which more than one potential candidate is found for a triple junction, the one with the minimum lateral distance is selected. Only the boundary segments of which the end point triple junctions are matched are considered for further grain boundary reconstruction. This procedure typically resulted in more than 60% matched grain boundary segments.

Another algorithm was used to connect the grain boundary segments of two adjacent sections. Grain boundary triangulation was carried out based on an algorithm proposed by Saylor et al [4]. The triangulation started from the first set of triple junctions whereby points from two consecutive layers are connected to each other according to the schedule shown in **Figure 4.13a**, which defines the length d. Next, for two consecutive layers the closest neighbor vertex points are determined, defining the lengths d1 and d2 (cf. **Figure 4.13a**). The shortest length d1 is chosen to close the loop of the first triangle (cf. **Figure 4.13b**). This procedure is repeated recurrently to expand the entire triangulation mesh between two pairs of triple junctions (cf. **Figure 4.13c**).

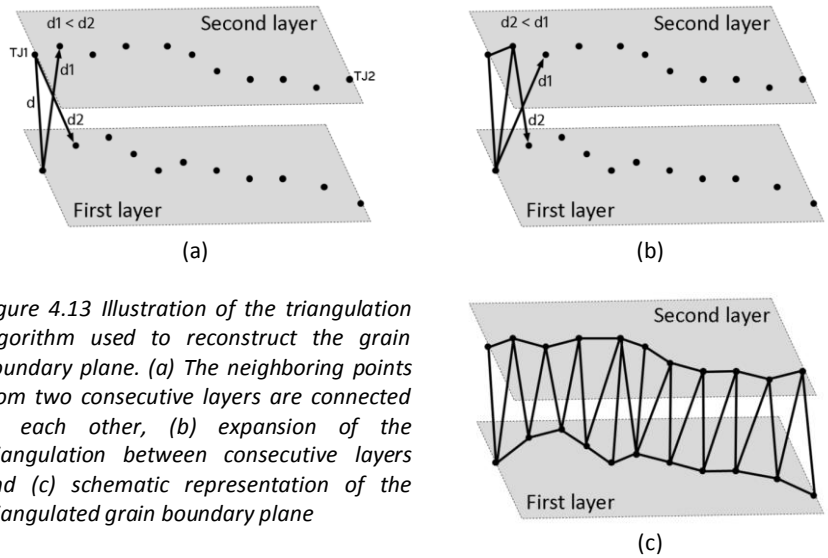

Figure 4.13 Illustration of the triangulation algorithm used to reconstruct the grain boundary plane. (a) The neighboring points from two consecutive layers are connected to each other, (b) expansion of the triangulation between consecutive layers and (c) schematic representation of the triangulated grain boundary plane

4.4. Discussion

4.4.1. Verifying the Alignment Procedure

To verify the hypothesis behind the alignment procedure employed in this study, i.e. the minimization of the average misorientation calculated in the EBSD maps

between adjacent layers, a two dimensional EBSD map was considered. Considering that all the rows of an EBSD map are precisely aligned (neglecting the drift which may happen during 2D EBSD measurements), two consecutive scanned lines (cf. **Figure 4.14**) were randomly chosen and the above mentioned alignment algorithm was applied (only in x direction) on the second line to align it with the first scanned line.

It is expected that as these two scan lines are well aligned, the minimum average misorientation should appear at the initial position, corresponding to X = 0. As it can be seen in **Figure 4.15**, the minimum misorientation between two adjacent scan lines is located precisely at x=0 with respect to the center of the map. By displacing the second scan line the average misorientation increases. This result verifies the precision of the employed alignment algorithm for the present microstructure, which contains around 20 morphologically uniform grains in the cross section.

On the other hand, if the microstructure contains features, which are elongated along a specific direction, this alignment technique cannot be used anymore. **Figure 4.16a** represents a schematic microstructure with elongated grains inclined to the horizontal direction (e.g. a sheared microstructure). As it can be seen in **Figure 4.16b**, by applying the alignment algorithm between each pair of adjacent scanned lines, the microstructure is modified to a columnar structure. The reason is that for this non-uniform microstructure, the minimum average misorientation between two consecutive sections is not located at x=0 (cf. **Figure 4.16c**), even the microstructure contains the same number of orientations as the microstructure presented in **Figure 4.14**.

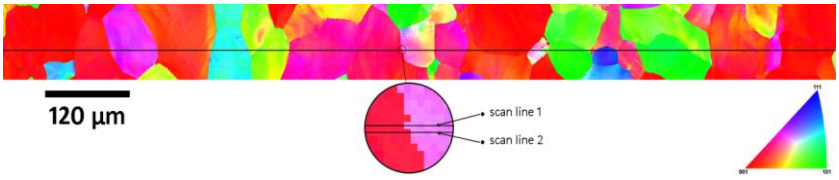

Figure 4.14 The EBSD map used for verification of the alignment algorithm.

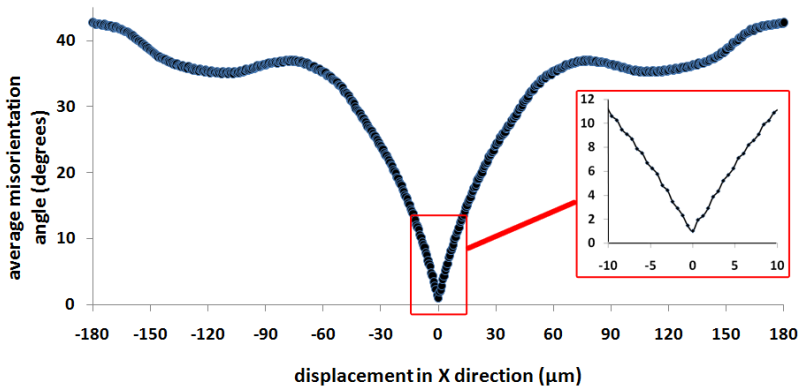

Figure 4.15 Average misorientation angle vs displacement in x direction for scan line 2 with respect to the scan line 1. The minimum average misorientation is located at x=0.

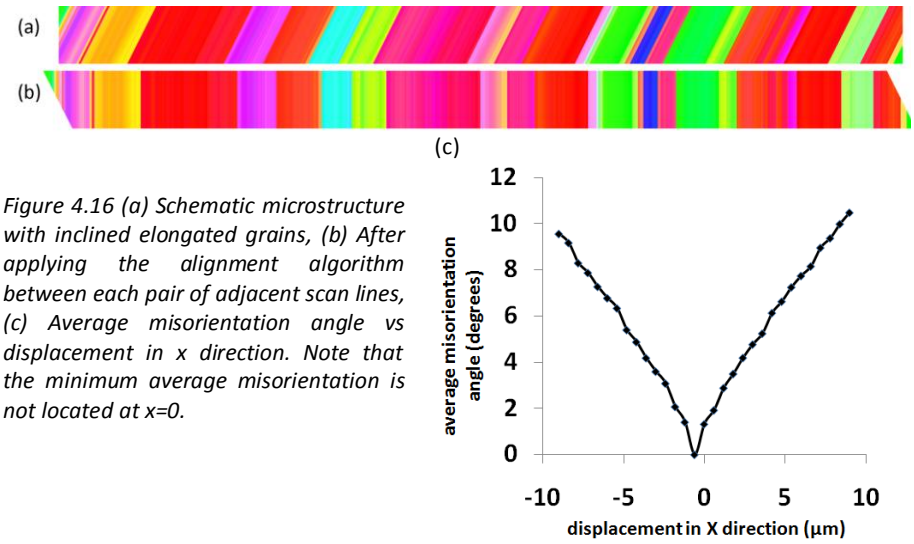

Figure 4.16 (a) Schematic microstructure with inclined elongated grains, (b) After applying the alignment algorithm between each pair of adjacent scan lines, (c) Average misorientation angle vs displacement in x direction. Note that the minimum average misorientation is not located at x=0.

4.5. References

1. *OIM ANALYSIS user manual* 2001, TexSEM Lab.
2. Lee, S.B., A.D. Rollett, and G.S. Rohrer, *Three-dimensional microstructure reconstruction using FIB-OIM*, in *Recrystallization and Grain Growth III, Pts 1 and 2*, S.J.L. Kang, et al., Editors. 2007. p. 915-920.
3. Rohrer, G.S., et al., *Deriving grain boundary character distributions and relative grain boundary energies from three-dimensional EBSD data.* Materials Science and Technology, 2010. **26**(6): p. 661-669.
4. Saylor, D.M., A. Morawiec, and G.S. Rohrer, *Distribution of grain boundaries in magnesia as a function of five macroscopic parameters.* Acta Materialia, 2003. **51**(13): p. 3663-3674.

Chapter 5. Grain Boundary-Magnetic Domain Interaction: a 3D investigation

"Knowing is not enough; we must apply. Willing is not enough; we must do."

Johann Wolfgang von Goethe
quoted by Wayne W. Dyer in "Inspiration: Your Ultimate Calling" (2008), p. 246

5.1. Introduction

In this chapter and the two next chapters, different applications of the 3D EBSD technique will be addressed as specific case studies. The first one presented in this chapter, is a 3D investigation of the interaction between magnetic domains in electrical steels and grain boundaries with a focus on grain boundary curvature derived from 3D experiments. To this purpose, the effort was made to model/predict the magnetic behavior of electrical steels based on their chemical composition and the microstructural variables such as grain size, crystallographic orientation and grain boundary inclination. In view of the main subject of this thesis, the focus of this chapter is on the effect of the grain boundary curvature and the interaction between magnetic domains and grain boundaries.

5.2. Electrical Steels: An Overview

5.2.1. Magnetic Domains and Magnetization Process

Electrical steels are the most important ferromagnetic materials and are mainly employed as magnetic cores for electromagnetic devices. In ferromagnetic materials, the atoms have a relatively large magnetic moment, which line up in parallel over regions containing a large number of atoms. Such a region is called a magnetic domain. Each magnetic domain is magnetized to its saturation value and neighboring domains are separated by domain boundaries or walls. Across a domain wall the direction of magnetization gradually changes. In a polycrystalline specimen, each grain may consist of several domains with different magnetization

directions (cf. **Figure 5.1**).

The magnitude of the magnetization vector (M) for the entire solid is the vector sum of the magnetizations of all the domains, and for an unmagnetized specimen, this vector sum is zero. However, when a ferromagnetic solid is magnetized in an externally applied magnetic field, the domains which are aligned parallel (or close) to the applied field will expand at the expense of the other domains. This expansion is done by the movement of domain walls. In the early stage of magnetization the movement of the domain walls is reversible; i.e. the walls will tend to move back towards the original position when the field is reduced. Crystal imperfections may act as barriers to the movement of domain walls. Therefore, in the later stages of magnetization, only the wall segments that have acquired enough energy from the field can overcome the barriers and continue the movement. This movement of domain walls is irreversible and the nonuniform type of movement gives rise to the Barkhausen effect. As the applied field increases further, the magnetic moments rotate and align with the orientation of the applied magnetic field. The crystal eventually attains saturation magnetization when all domains have rotated parallel to the field direction [1]. The domain configuration at different magnetization stages are illustrated schematically in **Figure 5.2** .

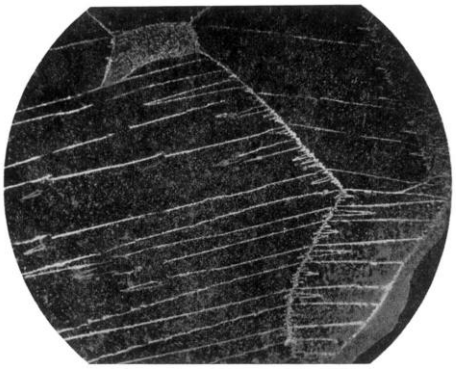

Figure 5.1 Domain structure in a polycrystalline grain oriented Fe-Si alloy (X500) [2].

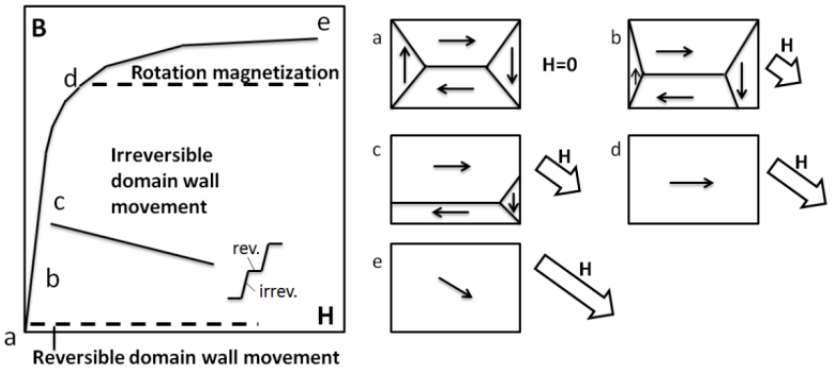

Figure 5.2 Schematic representation of the magnetization mechanism in ferromagnetic materials [3].

5.2.2. Losses and Permeability

The most important magnetic properties of soft magnetic materials such as electrical steels are high permeability and low core losses. The permeability (μ) indicates how much magnetic induction (B) is generated in an applied magnetic field (H). The permeability in vacuum (μ_0) is $4\pi\ 10^{-7}$ (H/m) [4, 5]:

$$\mu_0 = \frac{B}{H} \qquad 5.1$$

In the presence of a solid, **Equation 5.1** changes as follows:

$$B = \mu H = \mu_0 \mu_r H = \mu_0 H + J \qquad 5.2$$

where J is the magnetic polarization. For the magnetic fields applied in practice; i.e. $H<10^4$ A/m, the difference between B and J is very small (≤0.01T) and both of them are often used [6].

When a steel sheet is subjected to an alternating magnetic field, part of the energy used to magnetize the material is lost through the generation of heat in the core, which is commonly referred to as *core loss* (P_t). Traditionally, core loss is separated into *hysteresis loss* (P_h) and *eddy current* (P_e) loss. Hysteresis loss results from irreversible jumps of moving domain walls during magnetization. In other words, it is the energy dissipated in moving the domain walls through the material and for this reason this loss is sensitive to structural defects such as impurities, grain boundaries, strain regions and dislocations. The magnitude of hysteresis loss is proportional to the area enclosed by the B-H loop of the material during magnetization (cf. **Figure 5.3**) [1, 5-7].

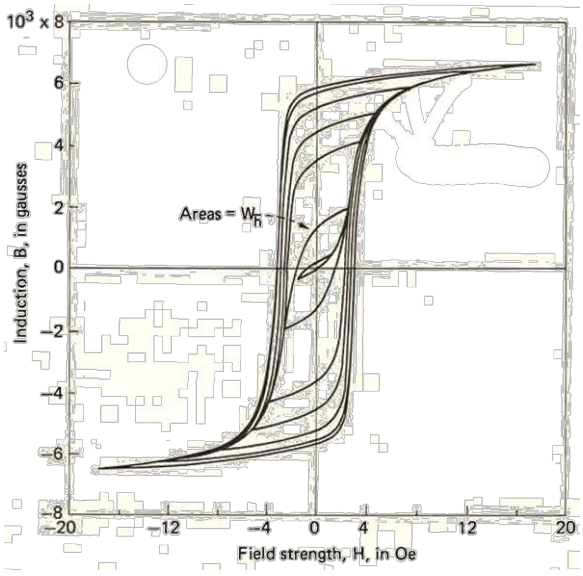

Figure 5.3 Family of hysteresis (B-H) loops in Permalloy. The area enclosed by each loop represents the hysteresis loss [6].

The eddy current loss (P_e) is a result of the eddy currents generated in the material which generate a magnetic field in the opposite direction to the field induced by the magnetizing current. The eddy current loss for thin steel sheets is dependent on the sample geometry and the frequency of the penetrating flux:

$$P_e = \frac{\pi^2 d^2 {B_{max}}^2 f^2}{6\rho\delta} \qquad 5.3$$

whereby the thickness d is in meter, the peak flux density B_{max} in Tesla, the frequency f in Hz, the density δ in kg/m^3, and the resistivity ρ in Ωm [4, 6]. Based on this equation, the eddy current loss can be reduced by increasing resistivity and decreasing the thickness of the material.

The sum of the estimated hysteresis and the calculated eddy current losses is significantly less than the measured losses. This difference is called the anomalous loss or excess loss (P_a), and may be as large as or larger than the calculated eddy current loss (cf. **Figure 5.4**). The anomalous losses have been linked to continuous rearrangements of domain configurations. In fact it appears only because the classical calculation of eddy current loss ignores the presence of domains and domain wall motion [4]. **Table 5-1** gives some representative values of core loss (measured at 60 Hz) in electrical steels.

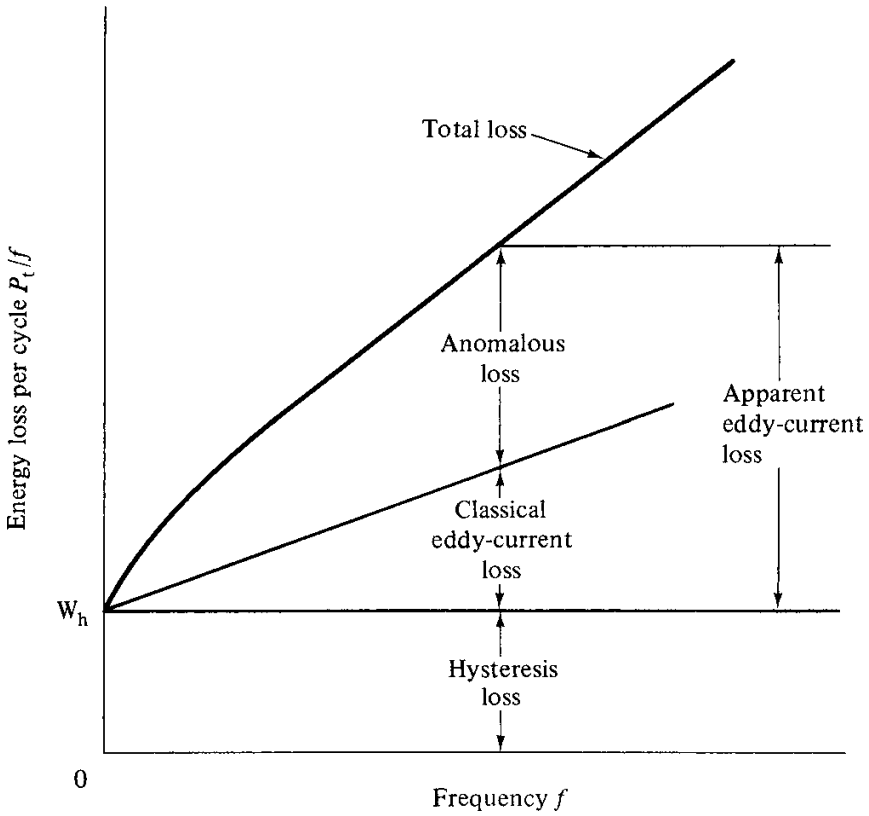

Figure 5.4 Conventional separation of losses in ferromagnetic materials [4].

Table 5-1 Properties of some electrical steels at 60 Hz [4]

Category	ASTM no.	Thickness, mm	Maximum B, kG	Loss W/kg
Lamination steel	47D175	0.47	15	3.85
	79D610	0.79	15	13.4
Grain-oriented (GO) electrical steel	18G041	0.18	15	0.90
	35G066	0.35	15	1.46
GO high permeability electrical steel	23P060	0.23	17	1.32
	27P066	0.27	17	1.46
GO high permeability laser-scribed electrical steel	23Q054	0.23	17	1.19
	27Q057	0.27	17	1.28

5.2.3. Classification of Electrical Steels

Electrical steels are essentially high purity Fe-Si alloys that can be divided in two groups depending on their application: (i) grain-oriented electrical steels, and (ii) non-oriented electrical steels. The grain-oriented electrical steels contain about 3% Si and have a very low C content. In these steels, the marked influence of crystallographic orientation on magnetic properties is utilized. In BCC iron, the magnetization process occurs most readily in the <100> direction, followed by the <110>, and least readily in the <111> direction (cf. **Figure 5.5**). <100> is the easy magnetization direction in BCC iron as it is the direction of spontaneous domain magnetization in the demagnetized state. Thermomechanical processes during steel making produce a highly textured material with the direction of easy magnetization <100> laying in the plane of the sheet, parallel to the rolling direction. Therefore, the grain-oriented electrical steels have superior magnetic properties in the rolling direction, which make them very suitable for application as a core material for static equipments such as transformers [1, 4].

Non-oriented electrical steels generally contain less than 4% silicon and aluminum and have relatively uniform magnetic properties in the rolling plane. Therefore, they are typically used as a core material for rotating machines where the direction of the applied field is not constant (e.g. motors and generators). Although the favorable texture in non-oriented electrical steels is significantly less pronounced, concentrated efforts are made to minimize the incidence of {111} planes and maximize the incidence of {100} planes (the cube fiber) parallel to the plane of the sheet. This steel grade is made by hot rolling to near-final thickness followed by pickling in acid to remove the oxide scale and cold rolling to final thickness, which gives the best surface finish and sheet flatness [1, 4, 6].

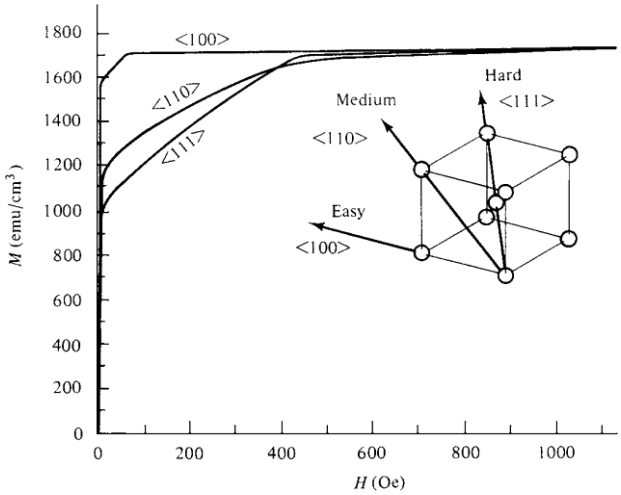

Figure 5.5 Magnetization curves for single crystals of iron [4].

5.3. Physical Metallurgy of Non-Oriented Electrical Steels

Magnetic properties of electrical steels such as magnetic permeability and electrical losses are mainly related to chemical composition, crystallographic orientation, microstructure and the mechanical conditions of the laminations in the core (e. g. stresses). In this part some influencing factors of the affecting parameters will be briefly discussed.

5.3.1. Precipitates and Inclusions

From a magnetic point of view, precipitates and inclusions in a magnetic field exhibit a different spontaneous magnetization from the surrounding material or, more likely, no magnetization at all due to the non-magnetic nature of the second phases. Domain walls tend to cling to the inclusions in order to decrease the domain wall surfaces (cf. **Figure 5.6**) and consequently also to reduce the domain wall energy, which is composed of exchange energy (due to the gradual change of neighboring magnetic spins inside the domain wall) and of anisotropy energy (due to the deviation of the wall magnetic spins from the easy magnetization directions). On the other hand, when an inclusion is intersected by a domain wall, its magnetostatic energy reduces too. The magnetostatic energy is a result of the presence of magnetic free poles at the surface of precipitates and inclusions. When a non-magnetic particle is inserted in a domain wall, the distance between the free magnetic poles and thus the magnetostatic energy is smaller as compared to the particle in the bulk of a domain (cf. **Figure 5.6**). The higher the energy reduction the higher is the pinning force of the precipitates and the inclusions. By hindering the movement of domain walls, precipitates and inclusions increase the hysteresis loss and are known to be detrimental to the magnetic properties. The particle volume influences its pinning effect. By increasing the particle volume, the presence of free poles on the surface of particle and consequently the pinning force increases. However, at a critical volume, secondary or closure domains are formed around the particle. By formation of the closure domains, the free magnetic poles are

redistributed over a larger area and the magnetostatic energy decreases and the pinning force decreases [1, 4].

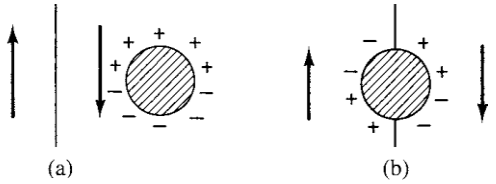

Figure 5.6 Interaction between a domain wall and an inclusion. When an inclusion is inserted in a domain wall (b), the magnetostatic energy and the wall surface energy is less than for the inclusion in a domain (a) [4].

5.3.2. Dislocations and Stresses

Plastic deformation deteriorates the magnetic properties of electrical steels. Interaction between regions of heterogonous stresses and magnetic domains results in local energy barriers for moving domain walls. These local energy barriers are of a magnetoelastic nature and are the result of magnetostrictive coupling, i.e. coupling between magnetization and deformation in case of misalignment of the magnetic spins with the main direction of tensile stress. The stress regions can have either macroscopic (e.g. stress heterogeneities due to non-uniform plastic deformation) or microscopic (stress field around dislocations) nature. Furthermore, the stress field of dislocations and specially dislocation clusters and cell boundaries act as strong pinning points for moving domain walls during the magnetization process [3, 4, 8].

5.3.3. Alloying Elements

Dissolving a small amount of alloying elements in iron increases the electrical resistivity (cf. **Figure 5.7**), and thus decreases the eddy current and total loss (cf. **Equation 5.3**). For this purpose, silicon and aluminum are the most effective alloying element to decrease the losses. Furthermore, an increase of the silicon content up to 6.5% reduces the magnetostriction to zero. On the other hand, the addition of these elements to steel reduces the number of ferromagnetic iron atoms present per unit volume and consequently reduces the saturation induction and thus the working induction. Addition of silicon has another drawback, i.e. it makes the alloy very brittle and difficult to roll (cf. **Figure 5.8**). Replacing part of the silicon by aluminum has been shown to reduce the brittleness of highly alloyed steels. Aluminum is also added to create a favorable texture [6, 9].

Silicon, aluminum and phosphorus are known as ferrite stabilizing elements and their addition to steel increases the γ/α transformation temperature or even eliminates the austenite domain all together. This is advantageous for electrical steels, because it allows annealing at high temperature without phase transformation, which deteriorates the texture [3, 6].

The addition of elements such as B and Zr to semi-processed non-oriented steels promotes the precipitation of nitrides (BN, and ZrN) during cooling to room

temperature, which improves the texture and therefore is beneficial for magnetic properties. In electrical steels a very low level of carbon is required to avoid precipitation of carbides which –as explained before- are detrimental for the magnetic properties since they hinder the movement of domain walls [3].

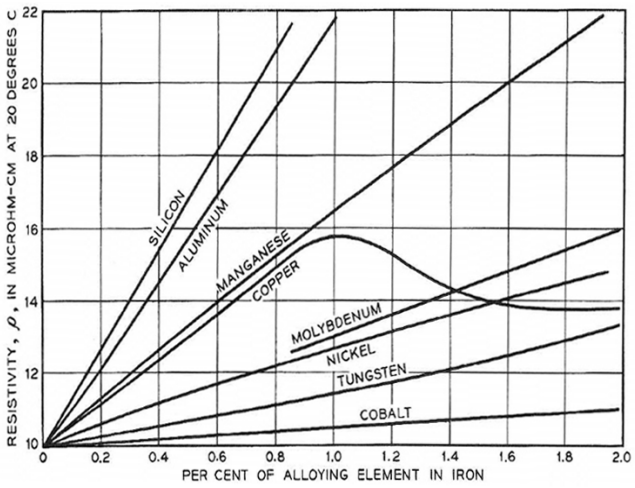

Figure 5.7 Effect of addition of small amounts of alloying elements to the resistivity of iron [6].

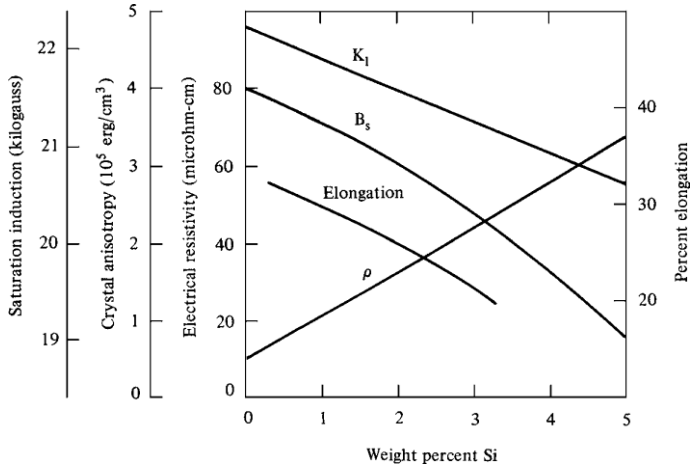

Figure 5.8 Variation of important magnetic parameters with silicon content for non-oriented electrical steels: magnetocrystalline anisotropy constant K_1, saturation induction B_S, electrical resistivity ρ and elongation [4].

5.3.4. Crystallographic Texture

The crystallographic texture is an important controlling parameter for the magnetic properties of electrical steels because the magnetic permeability of iron alloys is strongly orientation dependent. As it was mentioned earlier, the <100> directions in iron are the most easy to magnetize (easy magnetization direction), whereas

magnetization in the <111> directions is the most difficult. In other words, magnetization saturation can be reached at lower applied magnetic fields when the direction of the applied field is parallel to the easy magnetization direction. **Equation 5.4** exhibits the well-known expression for the magnetocrystalline anisotropy energy E_a. The anisotropy energy is the amount of energy (J/m^3), which is required to turn the local magnetization vector away from the easy magnetization directions [1, 4, 6]:

$$E_a = K_1(\gamma_1^2\gamma_2^2 + \gamma_2^2\gamma_3^2 + \gamma_3^2\gamma_1^2) + K_2(\gamma_1^2\gamma_2^2\gamma_3^2) \qquad 5.4$$

With γ_i the direction cosines between the magnetization vector and the 3 easy magnetization directions and K_1 and K_2 the anisotropy constants. For pure iron, the magnetocrystalline anisotropy constant K_1 is 48 kJ/m^3 and K_2 is 5 kJ/m^3. Additions of silicon and aluminum affect the anisotropy constant according to **Equation 5.5** [10]:

$$K_1 = (47.7 - 2.12 \text{ at\% Si} - 0.38 \text{ at\% Al}) \text{ KJ/m}^3 \qquad 5.5$$

Figure 5.9 represents the orientation dependence of the magnetocrystalline anisotropy energy for section φ_2=45 of the orientation distribution function. It has been shown that the average magnetocrystalline anisotropy energy for a measured texture can be calculated by integrating the E_a over all orientations of the orientation distribution function (ODF) [11].

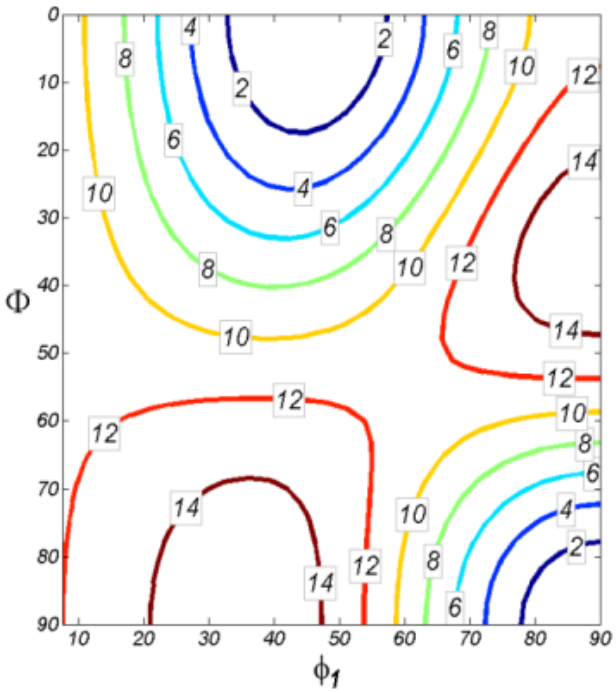

Figure 5.9 Magnetocrystalline anisotropy energy for orientations located in the φ_2=45° section of the orientation distribution function. The contours show the magnitude of E_a for pure iron.

5.3.5. Grain Boundaries

It is well known that grain boundaries can hinder the movement of magnetic domain walls due to presence of precipitates, inclusions and segregated atoms in the boundaries. Furthermore, the grain boundaries can deteriorate the magnetic properties because of the orientation difference on both sides of the boundary. Direct observations of domain structures at grain boundaries show that the domain structure at grain boundaries depends not only on the misorientation between the adjacent grains, but also on the angle made by the grain boundary plane with the grain magnetizations, i.e. the grain boundary inclination [12].

Misorientation across a grain boundary implies that the easy magnetization directions of two grains meeting at a grain boundary are not necessarily parallel. If the applied field is not sufficiently high to rotate the magnetization vectors out of their easy magnetization direction, there will be a discontinuity in the component of the magnetization vector normal to the grain boundary and the grain boundary supports a layer of (fictitious) free magnetic poles [13, 14]. Therefore, the free magnetic pole density produced at a boundary is proportional to the discontinuity in the normal component of magnetization vector at that boundary and represents the internal magnetostatic energy. If θ_1 and θ_2 are the angles between the magnetization vector of two grains and the normal to the grain boundary (cf. **Figure 5.10**), the free pole density at the grain boundary can be expressed by the following correspondence [4, 14, 15]:

$$\omega = I_s (\cos \theta_1 - \cos \theta_2) \qquad 5.6$$

where ω is the free pole density and I_s is the saturation induction (both in Tesla).

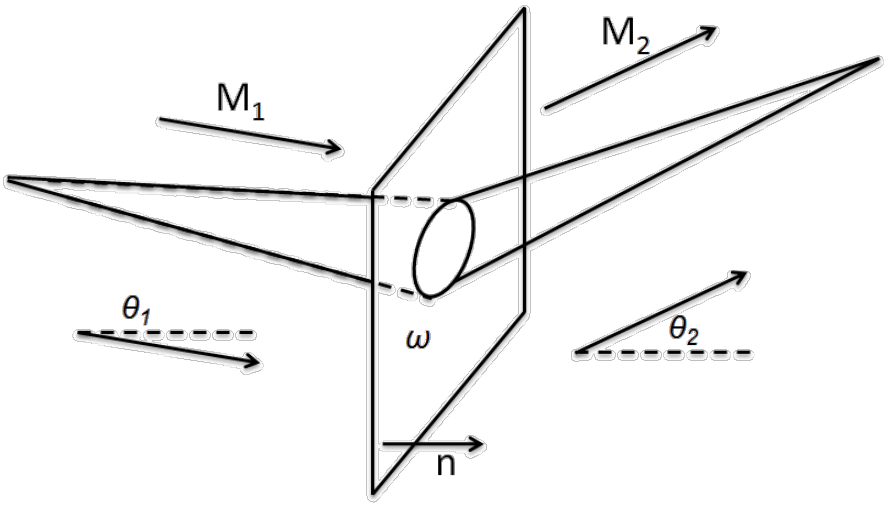

Figure 5.10 Schematic representation of nucleation of domains of reverse magnetization at a grain boundary [13].

According to Goodenough [13], the magnitude of the free magnetic pole density and the resulting magnetostatic energy plays an important role in the interaction between the magnetic domains and the grain boundaries. This magnetostatic energy is reported to be responsible for nucleation of magnetic domains at grain boundaries during reversal magnetization. Tobin and Paul [15] have shown that different types of domains may nucleate at the grain boundaries and the stability of various domain configurations may be determined by the balance between the reduction of free magnetic pole density at grain boundaries and the increase in energy associated with the formation of the domains themselves (cf. **Figure 5.11**). It has been reported that at the lowest pole densities no interaction happens between magnetic domains and grain boundaries. By increasing the magnetic pole density, double-spike configurations, single-spike and echelon structures, and finally closure domains appear as the results of the interaction between magnetic domains and grain boundaries. Although, the presence of magnetic free poles is eliminated by the creation of new domain structures at grain boundaries, these new domains may reduce the magnetic permeability and increase the hysteresis loss by the pinning effect [13].

In this research we aim to obtain a better understanding of the correlation between magnetic properties and microstructural parameters, by studying the interaction between magnetic domains and grain boundaries.

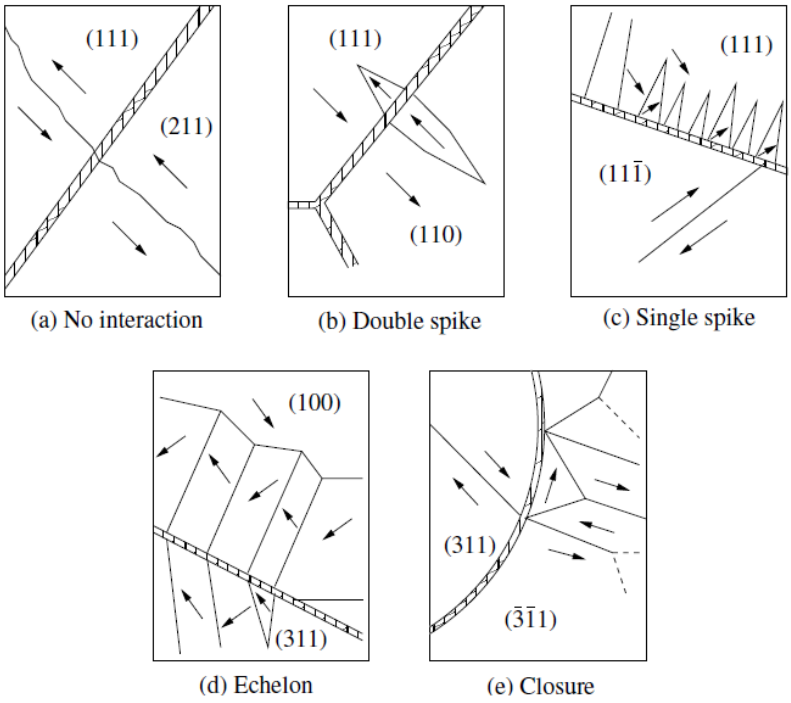

Figure 5.11 Different types of interaction between grain boundaries and domain walls shown in order of increasing magnetic free pole density [15].

5.4. Experimental procedures

5.4.1. Materials

In order to have statistically relevant results, 15 different chemical compositions containing low, medium and high alloying elements were provided for this study. The samples were produced at 2 different continuous annealing temperatures, which resulted in different grain sizes. In total 28 samples were prepared (2 samples were annealed at one temperature, only) of fully finished non-oriented electrical steels with a wide range of silicon (0.75-3.6 wt%), aluminum (0.004-1.7 wt%) and manganese (0.18-0.84 wt%) content. The samples had a thickness of 0.5 mm and different average grain diameter in the range of 40 to 300 µm (cf. **Table 5-2**).

Table 5-2 Summary of the materials used in this study

Alloying	Si (wt%)	Al (wt%)	Mn (wt%)	Si_{eq}	Continuous annealing temp. (°C)		Grain diameter (µm)	
Low	1.3	0.09	0.31	1.54	880	950	46	71
	0.99	0.52	0.29	1.73	880	950	74	82
	0.75	0.8	0.3	1.83	880	950	66	134
	1.4	0.11	0.54	1.74	880	950	41	65
	1.3	0.11	0.83	1.76	880	950	61	61
Medium	2.4	0.004	0.31	2.52	1020	----	183	----
	2.3	0.11	0.31	2.55	950	1020	86	219
	1.9	0.56	0.3	2.69	1020	1020	111	179
	1.5	1.1	0.31	2.94	950	1020	126	279
	1.9	0.34	0.49	2.50	950	1020	151	218
	1.9	0.1	0.84	2.35	950	1020	136	151
High	3.3	1	0.18	4.57	950	1020	142	291
	3.1	1.3	0.2	4.74	1020	----	192	----
	3.4	0.79	0.5	4.54	950	1020	129	318
	3.3	0.49	0.83	4.22	950	1020	140	296

5.4.2. Magnetic Measurements

The AC magnetic induction of the samples was investigated using the single sheet test method. The magnetic measurements on square-sized samples with dimension of 5 by 5 cm^2 and were carried out in two directions, parallel and perpendicular to the rolling direction of the samples. For each chemical composition and annealing condition, three different samples were measured and the average value was recorded. Considering the twenty eight samples in this study, the resulting data base consists of 56 data points. As a measure for the permeability the magnetic induction was considered at different magnetic fields (1000, 2500 and 5000 A/m or

B10, B25 and B50, respectively) at a frequency of 50 Hz.

5.4.3. Microstructural Characterization

In this section, a brief explanation about the microstructural characterization techniques is presented. More detailed explanation can be found in chapter 3.

5.4.3.1. Sample Preparation and EBSD measurements

For all 28 samples, Electron Backscatter Diffraction (EBSD) measurements were performed in the RD-TD plane with a high resolution FEI Quanta^{TM} 450 FEG-SEM. Depending on the average grain size, the step size of the EBSD measurements was chosen in the range of 2 to 10 µm. In the same way, the area of the EBSD scan was in the range of 1000^2 to 3000^2 µm^2. The anisotropy constant (K_1) was calculated by using **Equation 5.5** and the average anisotropy energy was calculated from all indexed point (>95%) in the whole scanned area.

In order to measure the normal to the grain boundaries and calculate the magnetic free pole parameter, *three-dimensional* EBSD was carried out on all 28 samples using the manual serial sectioning technique which includes consecutive steps of sample preparation and EBSD measurements. After each EBSD scan, the samples were finely polished with OP-S (Oxide Polishing Suspension with colloidal silica as abrasive particles) solution in an automatic polishing machine (the removal rate of each layer was approximately 1 µm / minute). In order to meticulously fix the scan area on subsequent layers for EBSD measurements, micro-Vickers indentations were used to mark a grid on the samples (cf. **Figure 5.12**). These indentations were also used to measure the thickness of each removed layer which was fixed to 10% of the average grain size of the sample. At least three consecutive sections were collected for each sample which allows us to precisely calculate the grain boundary curvature and its corresponding normal.

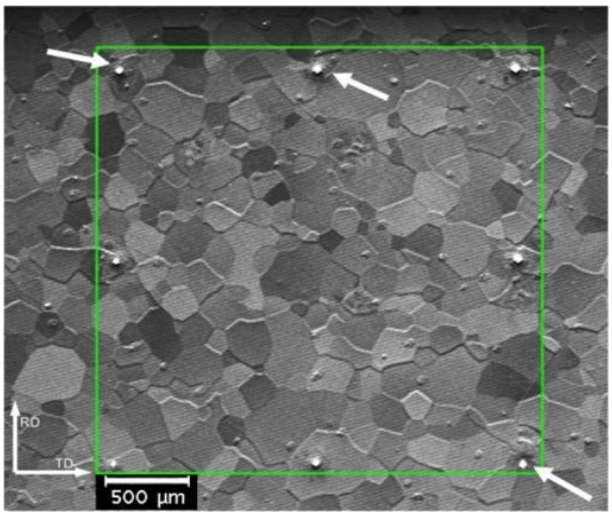

Figure 5.12 SEM image of the rolling plane. The green square shows the scanned area. White arrows show the micro-Vickers indentations that were used to identify the area after polishing.

5.4.3.2. Post Processing Analysis

To calculate the anisotropy energy from the EBSD data it was assumed that all the local magnetizations vectors are aligned parallel to the applied magnetic field, i.e. the saturation state. Therefore, no magnetic domain structure is present and the anisotropy energy associated with the magnetic domain walls is omitted. Considering these assumptions, the calculated anisotropy energy represents the energy that is required to rotate the local magnetization vectors (in a demagnetized state) away from the <100> directions towards the direction parallel to the applied field. The Euler angles of each scan point were used to derive the orientation matrix (cf. **Equation 2.2** in **chapter 2**). The anisotropy energy for each point was calculated using **Equation 5.4**. The direction cosines in this equation are the first and the second column of the orientation matrix when the applied field is parallel to RD and TD, respectively. For example, if g is the orientation matrix of a scan point and the applied magnetic field is parallel to RD, then:

$$E_{a,RD} = K_1(g_{11}^2 g_{21}^2 + g_{21}^2 g_{31}^2 + g_{31}^2 g_{11}^2) + K_2(g_{11}^2 g_{21}^2 g_{31}^2) \qquad 5.7$$

The anisotropy constant (K_1) was calculated according to **Equation 5.5** and (K_2) was assumed to be 0 because the second term in the **Equation 5.7** is significantly smaller compared to the first one.

To reconstruct the grain boundary plane and derive the normal to the grain boundary, consecutive sections need to be accurately aligned. An alignment algorithm proposed by Lee et al. [16], which is based on the minimization of the average disorientation between two adjacent layers, was applied to align the sections before reconstructing the microstructure. According to this method, it was observed that for a particular alignment of two neighboring sections there always exists a well defined minimum disorientation and the alignment corresponding to this minimum is considered as the exact alignment position (a more detailed explanation about the alignment procedure was given in **Section 4.3.1**).

5.5. Results

5.5.1. Anisotropy Energy

Figure 5.13 represents the magnetocrystalline anisotropy energy (E_a) maps and the corresponding inverse pole figure maps for two selected samples with low and high values of E_a. The anisotropy energy in these maps was calculated using **Equation 5.7** and by integrating the E_a over all indexed points inside each grain. As it can be seen, the magnitude of E_a changes from zero, for orientations in which the <100> direction is parallel to the applied magnetic field (rolling direction in this case), to ~16 kJ/m^3 for orientations in which the <111> direction is parallel to the applied magnetic field. These maps allow obtaining a visual comparison of the anisotropy energy of the samples.

Figure 5.14 shows the distribution of E_a for the samples shown in **Figure 5.13**. As it can be seen, the anisotropy energy distribution for the sample with the lower average E_a is much closer to the random distribution. The random distribution in this curve represents the distribution of E_a for a set of random orientations. According to this graph, the sample with lower average anisotropy energy exhibits the higher fraction at lower values of E_a (<11 KJ/m^3).

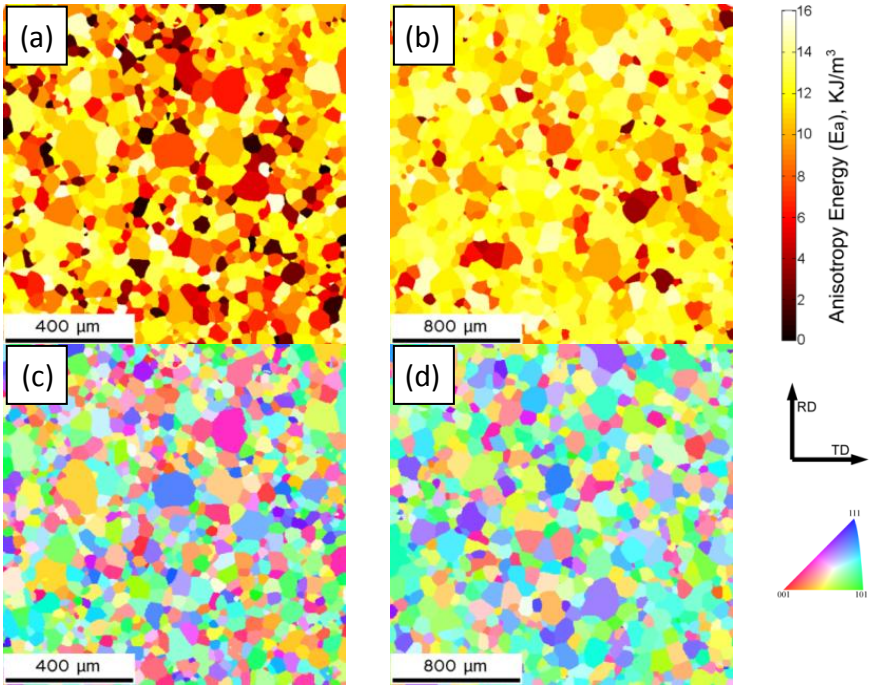

Figure 5.13 (a) and (b) magnetocrystalline anisotropy energy maps of samples with low and high average Ea values. The magnetization direction is parallel to RD. (c) and (d) corresponding ND inverse pole figure maps.

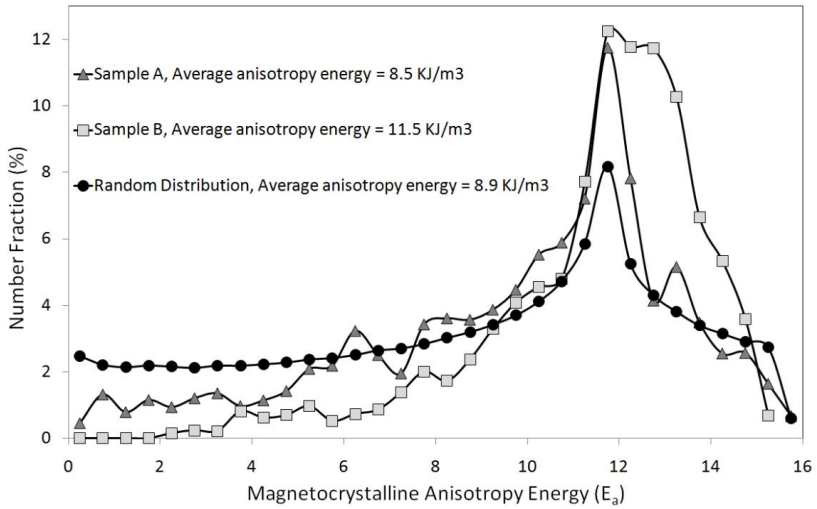

Figure 5.14 Distribution of magnetocrystalline anisotropy energy for the samples with low and high average anisotropy energy Ea. The random distribution curve shows the distribution of Ea for a set of random orientations.

5.5.2. Reconstructed Grain Boundaries

To reconstruct the grain boundary planes, the surface meshing algorithm presented in **Section 4.3.2.3** was applied on the consecutive 2D EBSD maps of each sample. An example of the 3-Dimensional microstructure reconstructed in this study to calculate the normal to the grain boundaries is depicted in **Figure 5.15a**. The size of this volume is 2,500×2,500×250 μm^3 (i.e. half of the total thickness of the sheet), and the number of slices is 10 with a thickness of 25 µm for each slice. From the 3-D microstructures it could be seen that the samples exhibit a recrystallized equiaxed grain structure. **Figure 5.15b** represents the reconstructed (triangulated) grain boundary planes of this sample. The vector perpendicular to the surface of each triangle is considered as the local normal to the grain boundary plane.

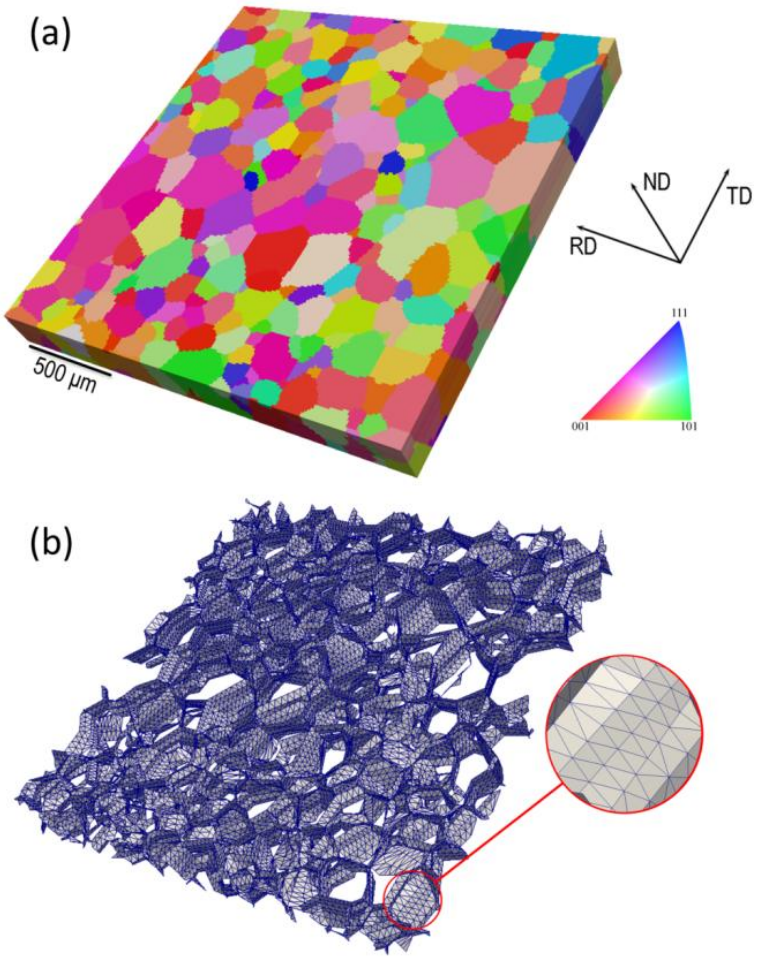

Figure 5.15 (a) Reconstructed 3-D microstructure resulting from aligning the slices based on the minimum average disorientation criterion between neighboring points in adjacent layers. The size of the volume is 2,500×2,500×250 μm^3. (b) The triangular mesh of the grain boundary planes.

The local grain boundary normal was determined by calculating the normal to each triangle in the sample coordinate system. The magnetic free pole density was then calculated by considering the angles between the easy magnetization direction and normal to the grain boundary in the two adjacent grains (cf. **Equation 5.6**). There are three symmetrically equivalent directions of easy magnetization in each grain, however -and as proposed by Knowles [14] - the local easy axis, which is nearest to the direction of the applied field is taken into account for this calculations.

After measuring the normals to the grain boundaries the frequency distribution of magnetic free pole density ($\omega^* = \omega/l_s$) was derived according to **Equation 5.6**, cf. **Figure 5.16**. This figure represents the ω^* distribution for the samples with low (sample A) and high (sample B) values of the magnetocrystalline anisotropy energy. The same plot also exhibits the ω^* distribution corresponding to a sample with random distribution of grain boundary poles. The random distribution was calculated based on 50,000 pairs of random orientations separated by a grain boundary with a randomly oriented normal. It can be seen that sample A with the lower average ω^* has the higher fraction of low ω^* values (<0.2) and lower fraction of high ω^* values (>0.2). As mentioned earlier, the higher values of ω^* is indicative for an increased discontinuity of the component of magnetization vector perpendicular to the grain boundary, in other words, the higher the value of ω^*, the more magnetostatic energy at the grain boundary. The sample with higher ω^* is supposed to develop more subsidiary domains at the grain boundaries during magnetization, which may hinder the movement of main domain walls resulting in worse magnetic induction.

5.5.3. Modeling the Magnetic Properties

The aim of this section is to correlate the magnetic induction with the chemical composition and the microstructural state-variables under consideration, i.e. grain size, anisotropy energy and free pole density. To this purpose, the average magnetic free pole density together with magnetocrystalline anisotropy energy, grain size, and silicon equivalent were included in a model to predict the magnetic induction. The average value of magnetic free pole density was calculated for all triangulated grain boundary planes with considering the area of each triangle as a weight factor. After trying different types of equations, **Equation 5.8** was found to deliver the best representation of the effect of the above mentioned parameters on magnetic induction. To have a better understanding of the effect of magnetic free pole density on the interaction between grain boundaries and magnetic domains, a similar equation was considered in which the free pole density term was omitted, cf. **Equation 5.9**.

$$B_H = C_0 + C_1.Si_{eq} + C_2.E_a + C_3/D + C_4.\omega^* \qquad 5.8$$

$$B_H = C_0 + C_1.Si_{eq} + C_2.E_a + C_3/D \qquad 5.9$$

Whereby C_i are the constants, E_a and ω^* are the average anisotropy energy and the average magnetic free pole density, respectively. D is the average grain size and Si_{eq} is the silicon equivalent.

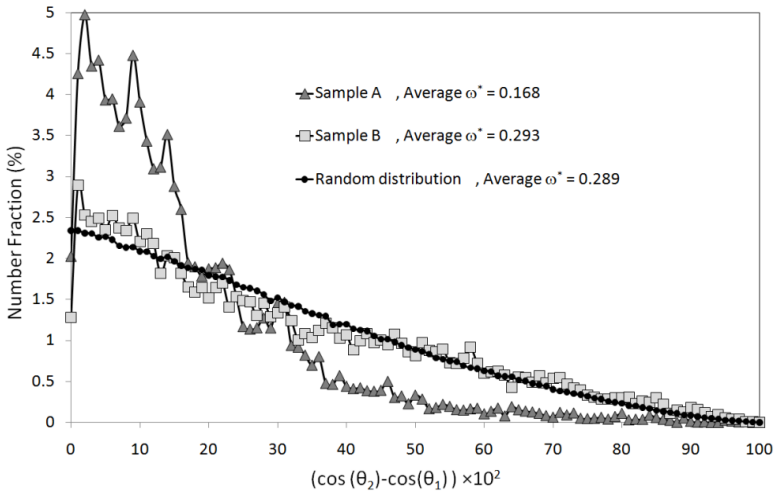

Figure 5.16 Distribution of ω for the samples with low and high ω* together with the random distribution.*

Table 5-3 summarizes the C_i constants and the corresponding R^2 values for both **Equation 5.8 and 5.9** at different applied magnetic fields. Comparison between R^2 values shows that a much better fitting is obtained when the magnetic free pole density is included in the model. This observation is independent of the level of the applied field and the magnetization behavior can be more accurately predicted at different external magnetic fields. **Figure 5.17** shows the experimental values of magnetic induction at low, medium and high applied magnetic fields versus the values predicted by **Equation 5.8 and 5.9**. It can be noticed also by visual inspection that the model with the ω^* parameter produces a better fit to the experimental values as compared to the model that ignores the presence of free magnetic poles at GBs.

*Table 5-3 Values of the constants of **Equations 5.8** and **5.9** for magnetic induction (B) at different applied magnetic field*

	C_0 (constant)	C_1 (Si_{eq})	C_2 (E_a)	C_3 (1/D)	C_4 (ω*)	R^2
B10	1.863	-0.0438	-0.0351	2.8677	---	0.7084
B10	1.909	-0.0402	-0.0295	1.3597	-0.39	0.9197
B25	1.946	-0.0259	-0.0354	2.7197	---	0.7392
B25	1.950	-0.0209	-0.0267	1.4743	-0.35	0.8872
B50	2.007	-0.0218	-0.0323	2.2195	---	0.7083
B50	2.006	-0.0159	-0.0240	1.1679	-0.33	0.8605

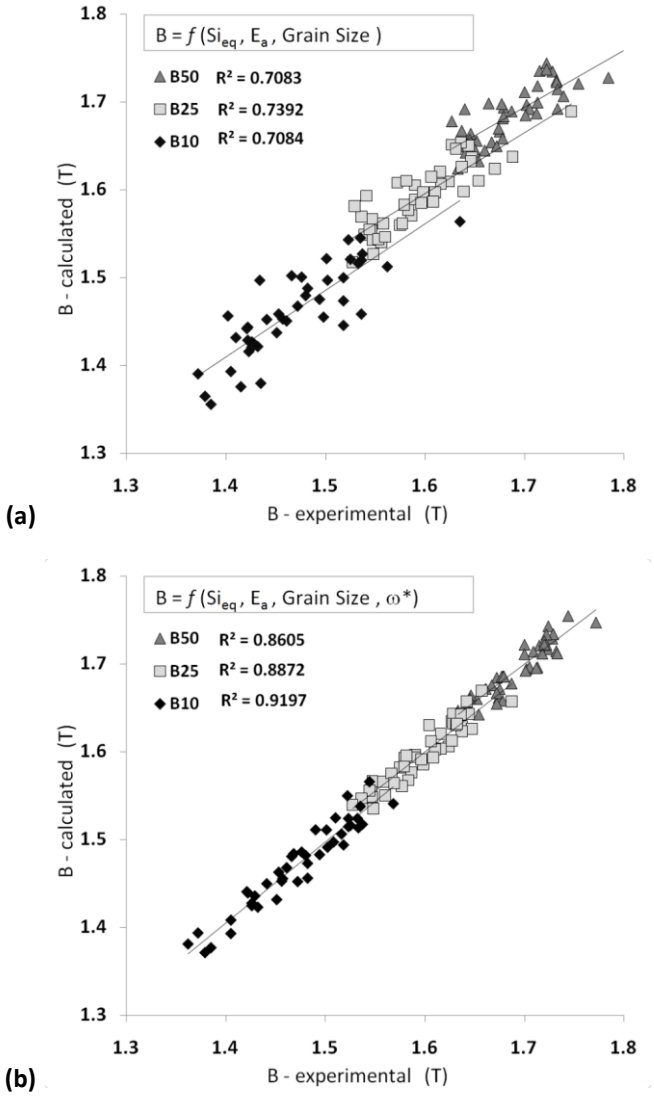

Figure 5.17 Calculated vs experimental values of the magnetic induction at different levels of the applied magnetic field. (a) Model based on silicon equivalent, anisotropy energy and grain size, (b) Model based on the same parameters plus the magnetic free pole density parameter (ω).*

5.6. Discussion

Magnetic induction is known to be a structure sensitive property of ferromagnetic materials. It means that the structural properties have direct effect on the magnetization behavior. In this study we focused on grain size, grain boundary inclination, anisotropy energy and chemical composition. To investigate the effect of chemical composition, the silicon equivalent was calculated considering the relative effect of silicon, aluminum and manganese on the saturation

magnetization [6]. To incorporate the effect of crystallographic texture, the magnetocrystalline anisotropy energy was taken into account. This seems to be a powerful tool especially when the anisotropy energy maps are plotted and compared to each other (cf. **Figure 5.13**). In an alternative way the magnetic quality of the texture can be evaluated by the A-parameter [17]. The A-parameter is the angle between the macroscopic magnetization vector and the closest <100> directions of the crystal. It was shown that the anisotropy energy and the A-parameter are linearly correlated [10].

Kawahara et. al. [12, 18] have done a dynamic observation of the interaction between magnetic domains and grain boundaries. According to their studies by Kerr and Lorentz microscopy, high angle grain boundaries have a more significant effect on the structure of magnetic domains developed at the grain boundaries than the low angle grain boundaries. They also reported that not only the misorientation between grains has an important role on the structure of magnetic domains at grain boundaries, but also the grain boundary inclination has a significant effect.

In a similar study, Tobin and Paul [15] have observed five fundamental domain types that may nucleate at the grain boundaries. According to them, the stability of different domain types depends on the magnitude of the free pole density at the grain boundary. **Table 5-4** shows the domain types that may nucleate at the grain boundary with different magnetic free pole density. The driving force for the development of these subsidiary domains is the reduction of magnetostatic energy due to the magnetic free poles. When the sample is under an externally applied field and the main domain walls move, the subsidiary domain is involved in this process, and consequently excess magnetization energy has to be provided.

In this study it is confirmed that besides the crystallographic orientation of grains, the inclination of the grain boundary additionally affects the magnetization behavior. It can also be seen (cf. **Table 5-3**) that all parameters included in the model have negative effects on the magnetic induction (negative coefficients of Si_{eq}, E_a, ω^*, and positive coefficient of 1/D), i.e. by increasing the value of the parameters the magnetic induction decreases. However, further evaluation of the contribution of each parameter (cf. **Table 5-5**) shows that the most effective parameter is the anisotropy energy with more than 50% contribution to the magnetization response and it becomes even more important with the increase of the external applied field. Conversely, the grain size with less than 5% has the minimum effect. At lower applied field the effect of Si_{eq} is more significant than the effect of the magnetic free pole density, but at higher applied filed the relevance of these effects are reversed, i.e. the contribution of free pole density increases from 19% to 23%, whereas the effect of Si_{eq} decreases from 26.3% to 14.6%.

Table 5-4 Stability of various domain structures at different magnetic free pole density [15]

domain type	$\omega^{*}=\omega/l_s$
No interaction	$0.00 < (\cos\theta_2 - \cos\theta_1) < 0.01$
Double spike	$0.01 < (\cos\theta_2 - \cos\theta_1) < 0.03$
Single spike	…
Echelon domain	…
Closure domain	$0.60 < (\cos\theta_2 - \cos\theta_1) < 0.70$

Table 5-5 Contribution of the model parameters in the magnetization response (%)

	Si_{eq}	E_a	Grain Size	ω^{*}
B10	30.1	65.7	4.2	
B10	26.3	52.6	1.9	19.2
B25	20.2	75.3	4.5	
B25	16.9	59.1	2.5	21.5
B50	19.0	76.9	4.1	
B50	14.6	60.2	2.3	22.9

The dominant effect of anisotropy energy at higher applied field can be explained by the rotation magnetization process. The rotation magnetization process tries to rotate the magnetization vector out of the easy magnetization direction and aligns it with the external applied field. Due to magnetocrystalline anisotropy energy, this rotation can be activated only when the external applied field is high enough.

The present model allows taking into consideration the effect of grain shape morphology in addition to grain size and crystal orientation. The manufacturing process of non-oriented electrical steels may produce a specific grain shape, e.g. columnar grains [19]. By optimizing the grain shape morphology, for a given average grain size and texture, additional benefits may be obtained in terms of electromagnetic properties of future grades of non-oriented electrical steels.

5.7. Conclusions

In this research, the effect of microstructural parameters on the magnetic induction of non-oriented electrical steels was studied. 3D EBSD performed by manual serial sectioning technique was used to derive precise information about grain boundary curvature and crystallographic orientation. The algorithms described in chapter 4 were employed to reconstruct the grain boundary surface mesh. This information was used to extract the local magnetic free pole density, which was then included in a model together with chemical composition, texture (in the form of magnetocrystalline anisotropy energy) and grain size to predict the magnetic induction.

The results show that the magnetic free pole density can be used as a parameter to study the interaction between magnetic domains and grain boundaries.

The higher density of the free poles at grain boundaries produces more subsidiary domains and reduces the speed of domain walls movement.

Together with grain size, anisotropy energy and chemical composition, the magnetic free pole density can be used to derive a more precise model of the magnetization behavior of non-oriented electrical steels.

5.8. References

1. Chen, C.W., *Magnetism and Metallurgy of Soft Magnetic Materials*. 1986, New York: DOVER PUBN Incorporated.
2. Kittel, C., *Physical Theory of Ferromagnetic Domains.* Reviews of Modern Physics, 1949. **21**(4): p. 541-583.
3. Eloot, K. *Nonoriented electrical steels. Flat steel products for electrical machinery*. 1997; 263-286].
4. Cullity, B.D. and C.D. Graham, *Introduction to Magnetic Materials*. 2009: Wiley.
5. Jiles, D.C., *Introduction to Magnetism and Magnetic Materials, Second Edition*. 1998: Taylor & Francis.
6. Bozorth, R.M., *Ferromagnetism*. 2003, New Jersey: Wiley.
7. Bertotti, G., *Hysteresis in Magnetism: For Physicists, Materials Scientists, and Engineers*. 1998: Academic Press.
8. Eloot, K., et al., *Relation between magnetic properties and changes in dislocation and cell structure due to cold deformation.* Journal of Magnetism and Magnetic Materials, 1996. **157**: p. 459-460.
9. Bavay, J.C. and J. Verdun, *NEW ELECTRICAL STEEL WITH HIGH PERMEABILITY.* Journal of Materials Engineering and Performance, 1993. **2**(2): p. 169-172.
10. Sidor, J.J., et al., *Through process texture evolution and magnetic properties of high Si non-oriented electrical steels.* Materials Characterization, 2012. **71**: p. 49-57.
11. Bunge, H.J., *Texture analysis in materials science : mathematical methods; translated by Peter R. Morris*. 1982, London ; Boston: Butterworths.
12. Kawahara, K., et al. *Effect of Grain Boundaries on Magnetic Domain Structures in Ferromagnetic Polycrystals*. in *Relationship between Magnetic and Structural Properties*. 2000. Japan: The Iron and Steel Institute of Japan.
13. Goodenough, J.B., *A theory of domain creation and coercive force in polycrystalline ferromagnetics.* Physical Review, 1954. **95**(4): p. 917-932.
14. Knowles, J.E., *The magnetostatic energy associated with a polycrystalline ferrite.* Journal of Physics D: Applied PhysicsEmail alert RSS feed, 1968. **1**: p. 987-994.
15. Tobin, A.G. and D.I. Paul, *Stability of Ferromagnetic Domain Structures at Grain Boundaries.* Journal of Applied Physics, 1969. **40**(9): p. 3611-3614.
16. Lee, S.B., A.D. Rollett, and G.S. Rohrer, *Three-dimensional microstructure reconstruction using FIB-OIM*, in *Recrystallization and Grain Growth III, Pts 1 and 2*, S.J.L. Kang, et al., Editors. 2007, Trans Tech Publications Ltd: Stafa-Zurich. p. 915-920.
17. Kestens, L. and S. Jacobs, *Texture Control During the Manufacturing of Nonoriented Electrical Steels.* Texture, Stress, and Microstructure, 2008. **2008**.
18. Kawahara, K., et al., *Observations of Interaction Between Magnetic Domain Wall and Grain Boundaries in Fe-3wt%Si Alloy by Kerr Microscopy*. MRS Online Proceedings Library, 1999. **586**: p. 169-174.

19. Kovac, F., M. Dzubinsky, and Y. Sidor, *Columnar grain growth in non-oriented electrical steels.* Journal of Magnetism and Magnetic Materials, 2004. **269**(3): p. 333-340.

Chapter 6. Three-Dimensional EBSD Characterization of Fatigue Crack Morphology

"No amount of experimentation can ever prove me right; a single experiment can prove me wrong."

Albert Einstein

quoted by Bob Moores in "Skeptical: Show Me Evidence-then I'll Believe" (2011), p. 25

6.1. Introduction

In diesel engines of trucks, the repetition of the start-up and shut-down of engines causes severe mechanical loading in some parts of the engine, such as cylinder blocks and heads and this may lead to localized cracking due to stresses that develop as a result of thermal gradients and thermal mismatch. This phenomenon is known as Thermo-Mechanical Fatigue (TMF). TMF is believed to be the dominating process responsible for cracks developing in engine components [1].

In the present chapter, the emphasis is on analyzing the crack path evolution induced in Compacted Graphite Iron (CGI) during TMF. The 3D EBSD technique, described in chapter 4, was employed to meticulously characterize TMF crack paths, in relation to microstructural features and to find out how and by which mechanisms the cracks predominantly develop. The content of this chapter has been published as a paper in the Journal of Materials Characterization with the collaboration of Dr. Sepideh Ghodrat[1].

6.2. Compacted Graphite Iron

Compacted Graphite Iron (CGI) is a common material of choice for diesel engine parts of heavy trucks. This is a type of graphitic cast iron, consisting of vermicular graphite particles embedded in a metal matrix of pearlite. This composite material

[1] Pirgazi, H., S. Ghodrat, and L.A.I. Kestens, Three-dimensional EBSD characterization of thermo-mechanical fatigue crack morphology in compacted graphite iron. Materials Characterization, 2014. 90: p. 13-20.

provides a suitable combination of thermal and mechanical properties to achieve the desired performance of cast iron cylinder heads [2]. The graphite provides favorable thermal properties (i.e. thermal conductivity), whereas pearlite is responsible for appropriate mechanical properties (strength and fatigue resistance). However, microstructural instability and evolution during operation may deteriorate the thermal and mechanical properties of CGI and accordingly the TMF properties. It is discussed by Seifert et al. [3, 4] that graphite particles in cast iron weaken the material in tension by decreasing the stiffness, since the graphite particles partly delaminate from the matrix. Cracks propagate also through the graphite particles due to the weak Van der Waals bonding along the c-direction of hexagonal crystalline structure of graphite [5]. In compression, though, interfacial microcracks are closed and a higher stiffness results. Also, variations in mechanical and thermal properties between the matrix and graphite result in local stresses and possible stress relaxation by cracking. These mechanisms affect the mechanical characteristics of the material, which are unavoidably coupled with damage processes [6].

6.3. Thermo-Mechanical Fatigue

Thermo-mechanical fatigue (TMF) is a particular type of Low Cycle fatigue (LCF), which is caused by stresses and strains that develop during changes in both thermal and mechanical loads. TMF is life limiting for blades and vanes of gas turbines, combustion chambers, high pressure and intermediate pressure rotors of steam turbines, components of diesel engines such as pistons used in cylinder heads and other components, which are exposed for long periods of time to elevated temperatures and subjected to large numbers of heating and cooling cycles. As a result of these cycles, the mechanical and thermal properties of the material subjected to TMF deteriorate. This fatigue damage can finally lead to localized cracking [7].

In order to understand TMF cracking and the involved mechanisms, it is important to characterize the microstructure evolution and the TMF behavior under realistic thermal and mechanical loads. Hence, to the purpose of studying the underlying microstructural mechanisms of TMF, a study has been carried out that was specifically aimed to characterize the localized cracking of cylinder heads due to the start-up/shut-down cycles of diesel truck engines. In order to simulate the TMF behavior occurring in cylinder heads a standard mechanical test has been developed [8] in which a dog-bone sample was cyclically heated up and cooled down between a maximum and a minimum temperature at which the sample was kept during a certain period (the holding time). Such a temperature cycle mimics the sequence of many start-stop cycles during the operational life of the engine. In order to reduce the testing time and also to improve reproducibility, specimens were provided with a sharp circumferential notch in the middle of the gauge length (cf. Section 6.4.2). Results on the mechanical properties measured in these tests can be found elsewhere [8, 9].

The emphasis in the present work is on the microstructural characterization of the ligament surrounding the fatigue crack path. To the present purpose of understanding the TMF mechanism, the microstructure of the ligament and the

precise characteristics of the crack features in relation to the local microstructure are of interest. This microstructural characterization is usually carried out on two-dimensional (2D) sections by conventional or Scanning Electron Microscopy (SEM) which reveals most of the microstructural features of the material. Statistical stereological techniques have been developed to gain insight into the three-dimensional (3D) aspects of the microstructure from the 2D data [10]. Although it has been possible to characterize most of the microstructural features in 2D using standard microscopy instrumentation and stereological procedures, there are still many important microstructural features that can only be measured in 3D [11]. Full crystallographic characterization of all kinds of interfaces, e.g. grain boundary character and inclination, spatial anisotropy of grain shape, second-phase precipitate morphology and crack propagation features are examples in which 3D information is of great importance [10, 12].

With 2D orientation microscopy and analyzing the crystallographic orientation in the vicinity of the crack it is possible to verify if the crack propagation is intergranular or transgranular. However, this characterization method cannot be used to study the fracture mechanisms in which the relation between fracture plane and certain crystallographic planes (cleavage or slip planes) are necessary. Therefore, an extensive SEM and EBSD study was carried out on CGI loaded under TMF conditions and microstructural changes during deformation were evaluated by analyzing quantitative data obtained by orientation contrast microscopy in 3D. Statistical processing of the crystallographic data was applied on a very wide scale of material in the order of millimeters.

6.4. Experimental procedures

6.4.1. Material and specimens

The material investigated in this study is Compacted Graphite Iron (CGI) with a pearlitic matrix. **Figure 6.1** shows the microstructure of CGI, which is composed of a complex morphology of compacted graphite particles, pearlite with a variety of lamellar structures, and a small fraction of ferrite. The nominal chemical composition is given in **Table 6-1**.

The high amount of carbon and silicon leads to the presence of the carbon-rich graphite phase in the microstructure of cast iron, named graphitic cast iron, also known as gray cast iron. In general, the chemistry of CGI is more complex than for other cast iron types; the content of inoculant elements (Mg, Ce), spheroidizing elements (Mg, Ca, and/or rare earth metals) and antispheroidizing (Ti and/or Al) elements must be controlled accurately in order to produce a microstructure that contains the worm-shaped vermicular particles [7].

Table 6-1 Nominal chemical composition of the CGI (wt.%)

C	Si	Mg	Cu	Mn	Cr	Ti	Sn	Pb
3.60-3.90	2.00-2.20	0.01-0.15	0.75-0.95	0.15-0.40	<0.10	<0.015	0.06-0.10	<0.002

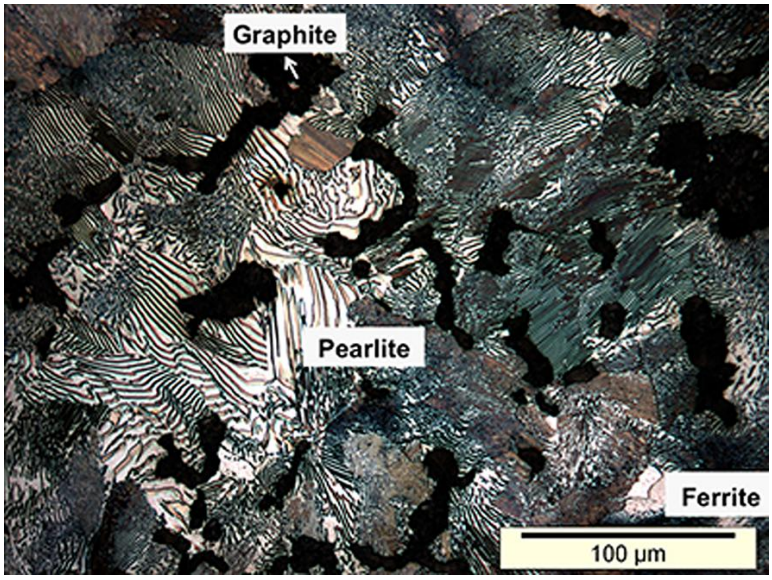

Figure 6.1 Microstructure of the pearlitic CGI.

6.4.2. TMF Test procedures

A TMF experiment was conducted using a 25 kN MTS servo-hydraulic fatigue machine capable of imposing independent temperature and strain profiles on a test specimen. Solid smooth dog-bone specimens were machined to a final cylindrical gauge length of 22.0 ± 0.25 mm and a diameter of Ø6.00 ± 0.025 mm. In a next step, the specimen was provided with a circumferential notch in the middle of the gauge length, with a depth of 0.2 mm and a 0.04 mm tip radius (cf. **Figure 6.2**). Cracks were always found to initiate from graphite particles at or near the notch tip, and in this respect a possible influence of surface roughness on TMF lifetime (as would be the case when using a smooth specimen) can be excluded when using notched specimen.

A high-frequency induction generator was used for heating. Cooling was accomplished by blowing compressed air from three sides onto the specimen and by thermal conduction into the water-cooled specimen grips. Detailed information about TMF test procedures and specimens are reported elsewhere [8, 13].

The TMF test was performed under total constraint conditions, meaning that the total strain measured by the extensometer was kept constant. By cycling the temperature between 50 °C and 420 °C, out-of-phase (OP) TMF loading was accomplished. Note that the applied constant temperature range (50-420 ºC) in combination with the coefficient of thermal expansion of the CGI (16×10^{-6} K^{-1}) leads to a fixed mechanical strain range of almost 0.6%, indicating that cyclic plasticity is bound to occur and a limited amount of cycles to failure is most probable. Holding times of 30 s were applied during both maximum and minimum temperatures in order to stabilize temperature levels throughout the specimen. This TMF test procedure is intended to replicate the thermal and mechanical conditions in the valve bridge area of cylinder heads.

6.4.3. Three-Dimensional Measurements

To have a better understanding of the effect of the crystallographic orientation on the TMF crack growth path, a TMF loaded sample, with 195 cycles to failure, was investigated by 3D EBSD measurements using the manual serial sectioning technique. This method includes consecutive steps of sample preparation and EBSD measurements. The sample preparation consists of mechanical polishing with OP-S (Oxide Polishing Suspension with colloidal silica as abrasive particles) solution, with a particle size of 0.04 µm. In this step an automatic polishing machine with a uniform rotational speed was used to make sure that all sections are parallel to each other. Furthermore, the planparalellity of the individual layers was also controlled by a series of micro-Vickers indentations around the measured area. The thickness of layers (Z distance) was measured using the same Vickers indentations and fixed to 8.0±0.5 µm. This value is fine enough to cover all desired microstructural details of the sample, and is big enough to make it possible to have a full 3D microstructure in a reasonable time. In total 31 sections were prepared to cover a total Z length of 240 µm. The EBSD measurements were carried out by employing a high resolution FEI Quanta^{TM} 450 FEG-SEM. EBSD patterns were obtained and analyzed by means of TSL$^{®}$ software. Each EBSD measurement was carried out in the middle of the gauge length of the TMF loaded sample in an area of 6,000 × 700 µm^2. For each section two adjacent EBSD scans with dimensions of 3000 × 700 µm^2 were merged. These measurements were performed with an in-plane step size of 3 µm on a square grid scanning pattern, by which the finest microstructural details of this material could be detected.

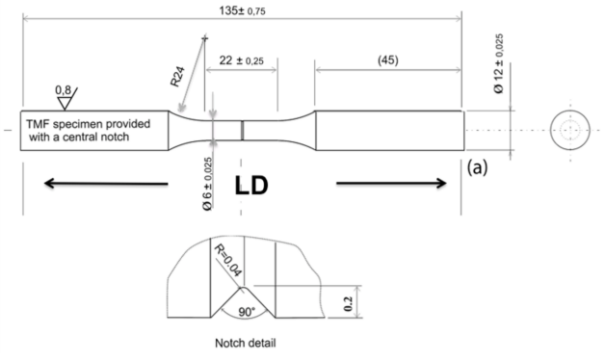

Figure 6.2 Circumferential notched dog-bone specimen with notch depth of 0.2 and a 0.04 mm tip radius. Dimensions are indicated in mm, LD is loading direction.

6.5. Results and Discussion

6.5.1. Data Processing (3D SEM-EBSD Imaging)

The first step to reconstruct the 3D microstructure is the alignment of the sections. In this study an algorithm, which is based on the minimization of the average disorientation between two adjacent sections was used [14]. The algorithm

proposed by Lee et al. [14] was improved by considering the rotational displacement as well as X-Y displacement between the slices. According to the method applied here, it was observed that for a particular alignment of two sections, always a well defined minimum exists and this minimum is taken into account as the correct alignment position. For a more detailed explanation about the alignment procedure, the reader is referred to **Section 4.3.1**.

After alignment, a triangulation algorithm was employed to reconstruct the crack surface. To this purpose, an algorithm proposed by Saylor et al. [15] was used. The triangulation started from the notch tip whereby points from two consecutive layers are connected to each other according to the schedule shown in **Figure 6.3a**, which defines the length d. Next, for two consecutive layers the closest neighbor vertex points are determined, defining the lengths d1 and d2 (cf. **Figure 6.3a**). The shortest length d1 is chosen to close the loop of the first triangle (cf. **Figure 6.3b**). This procedure is repeated recurrently to expand the entire triangulation mesh (cf. **Figure 6.3c**).

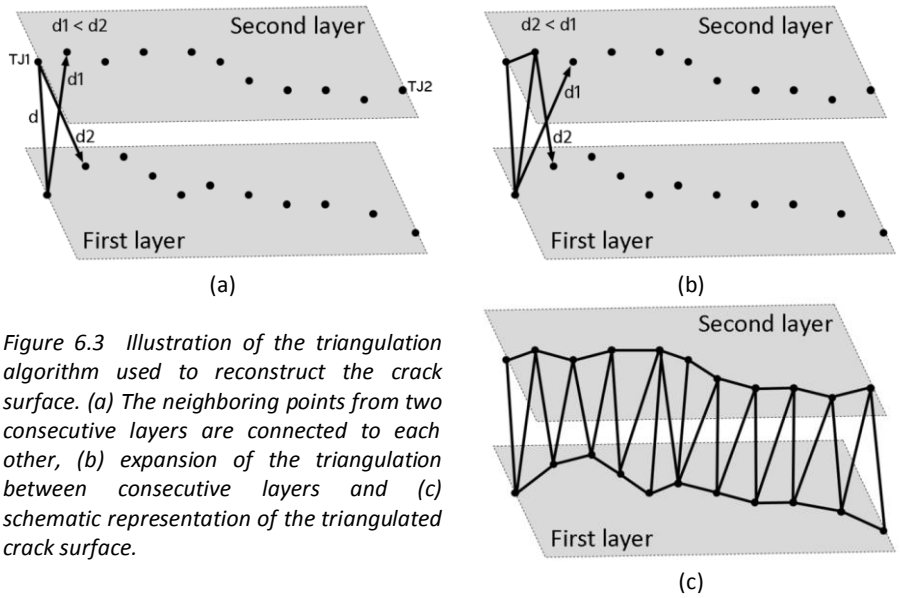

Figure 6.3 Illustration of the triangulation algorithm used to reconstruct the crack surface. (a) The neighboring points from two consecutive layers are connected to each other, (b) expansion of the triangulation between consecutive layers and (c) schematic representation of the triangulated crack surface.

Although the EBSD measurements provide extensive microstructural information especially about the crystallographic orientation, because of the low indexation rate in the vicinity of the crack it was not possible to precisely determine the morphology of the crack edge from the EBSD scans. For this reason, in addition to the EBSD scans, high resolution secondary electron SEM images were also recorded. For each section several secondary electron images with a magnification of 700 X were collected through the entire surface and were merged to show a high resolution large scale view of the surface (cf. **Figure 6.4**). As it can be seen from this figure crack and graphites were separately highlighted with different colors using a

MATLAB image processing toolbox and some manual corrections. This marking allows obtaining a sharp separation between metal matrix, graphite particles and the crack. These SEM images were converted to the format of an EBSD data set. To this purpose, it was assumed that each pixel of the image is one scan point with X and Y coordinates directly recovered from the X and Y coordinates of the pixels of the SEM image and Euler angles, image quality and confidence index arbitrarily assigned. To distinguish between crack, graphite and metal matrix, they were considered as three different phases. This helps us to look at crack and graphite separately in the ParaView® software, which is used for 3D image reconstruction.

Subsequently, the secondary electron derived data sets with graphite and crack as two separate phases were merged with the real EBSD scans. In order to do this, the scan information of graphite and crack derived from the SEM images was substituted in the real EBSD scan. This produces a new file with three phases (iron, crack and graphite) and the crystallographic orientations of the iron phase. The inverse pole figure (IPF) map of the reconstructed volume after applying the above mentioned procedure is presented in **Figure 6.5**.

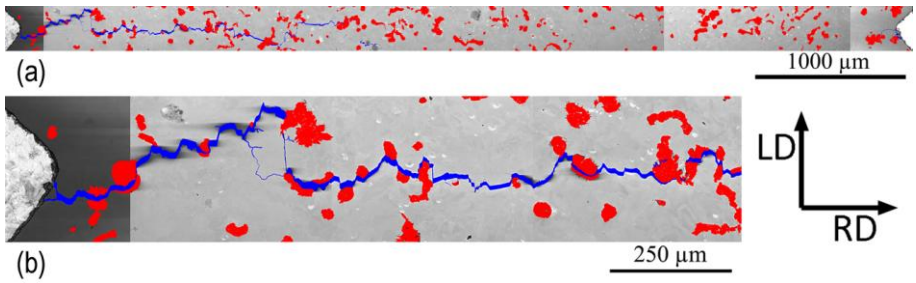

Figure 6.4 (a) Secondary electron SEM image through the entire thickness, this image consist of several individual images. The horizontal length of the image is 6 mm. (crack is highlighted as blue and graphite as red). (b) The same image with higher magnification (LD and RD are loading and radial directions, respectively).

6.5.2. Crystallographic Features of the Crack Path

It is known from the literature that brittle fracture in BCC metals, e.g. in steel, occurs on {001} cleavage planes. These observations were generally limited to single phase ferritic steels [16]. It remains to be verified, however, whether or not this still applies to brittle fracture as predominantly observed in the fine pearlitic matrix of the current CGI material under investigation [7]. Therefore, in order to verify the crystallographic features of the brittle fracture and evaluation of the relative effects of texture and graphite morphology on the TMF crack growth path, a quantitative study was carried out with the help of the 3D reconstructed volume. The ω angle which is the angle between the normal of the crack plane (in this case, each triangle of the triangular mesh of the crack plane) and the {001} plane which can only be observed in a 3D image was computed. A schematic drawing of the

crack plane and a {001} plane with the ω angle is depicted in **Figure 6.6**. The TMF crack extracted from the reconstructed microstructure is shown in **Figure 6.7**. The colors in this picture represent the value of the ω angle.

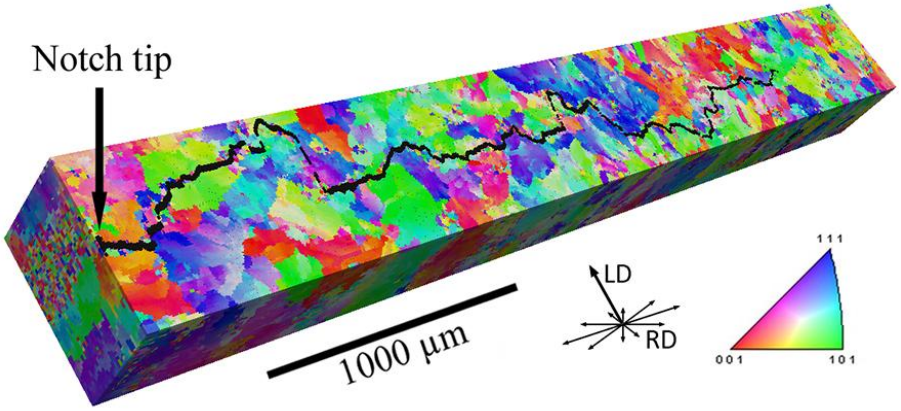

Figure 6.5 Reconstructed microstructure, crack is highlighted as black.

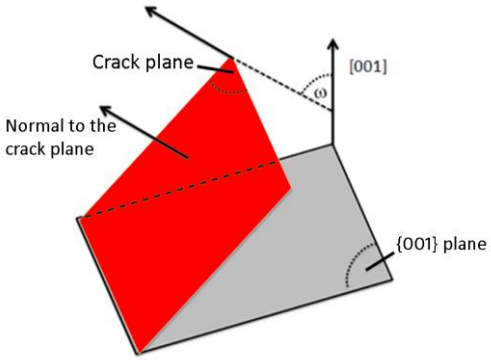

Figure 6.6 Schematic drawing of the crack plane and a {001} plane with ω angle.

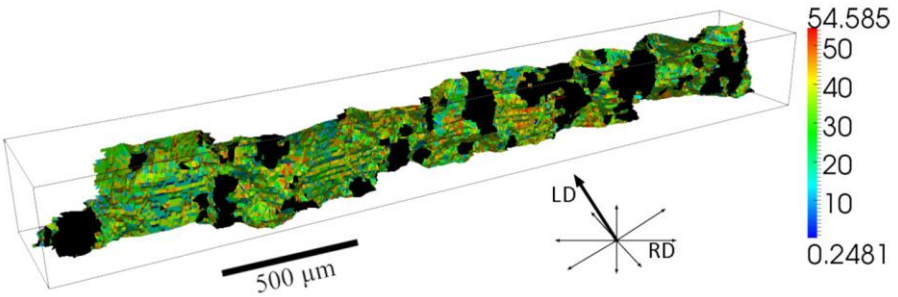

Figure 6.7 Lateral view of the crack path exhibiting the ω angles according to the color code of the legend. The black regions represent the graphite particles on the crack plane.

The measured distribution of the ω angle together with the random distribution is shown in **Figure 6.8**. This random distribution represents the distribution of the angle between the normal of randomly distributed planes and the nearest {001} plane. It can be seen that the measured distribution of ω closely resembles the random distribution of ω. The average values of ω for the measured and the random distributions are equal to 32.5˚ (with the standard deviation of 11.7˚) and 36.5˚, respectively. This result shows that there is no preferred crystal plane that is parallel to the crack plane and strongly suggests that the brittle fracture in CGI does not occur on the traditional {001} cleavage planes. This may be related to the fact that the pearlite metal matrix does not represent a continuous volume of BCC crystal, but a fine mixture of BCC ferrite and orthorhombic cementite (Fe_3C).

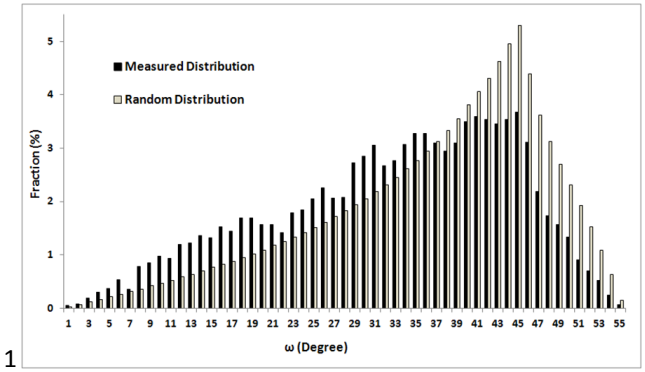

Figure 6.8 Measured and random distribution of ω angle as derived from 3D EBSD data.

The distribution of the (local) normals to the crack surface on the unit triangle of the standard stereographic projection has been represented in **Figure 6.9**. The intensity of this distribution ranges from 0.85 to 1.1 MRD (Multiples of Random Distribution) which is very close to the random distribution. This observation strongly supports the conclusion that there is no particular crystallographic preference of the fracture plane and the crystal plane parallel to the fracture surface is nearly of random orientation.

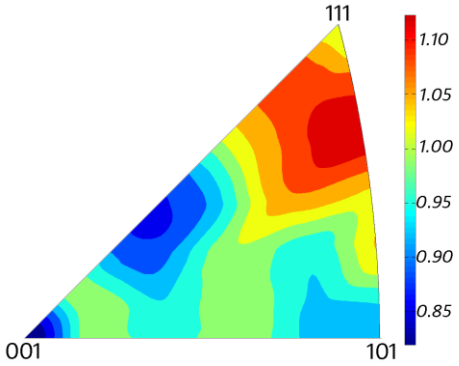

Figure 6.9 Distribution of the crack surface normals with respect to the crystal reference frame. The color bar is based on multiples of random distribution (MRD).

In order to check the hypothesis of crystal orientation effect on the crack path, a further analysis was carried out. In the previous evaluation it was found that there was no overall influence of crystal orientation on the crack propagation. It still remains to be verified, though, if the crystal orientation might have a local effect far away from the graphite particles, where there is no influence of the graphite morphology. To this purpose, the value of ω was evaluated as a function of distance to the nearest graphite particle *in* the crack plane and determined in the 3D sample volume (cf. **Figure 6.10**). If the crystal orientation effect were to play a role far away from the graphite particles, one would expect a negative slope of the curve that represents the ω value versus the distance to the nearest graphite particle. The measured data derived from the 3D data set, however, do not show such a descending slope, but nearly a constant ω value (~32˚) that very well approximates the average of the random distribution (~36˚).

6.5.3. Graphite Particles Distribution

The data analysis suggests a crucial role of graphite particles in the crack propagation mechanism, as it appears that the crack path jumps from one graphite particle to the neighboring one (cf. **Figure 6.4**) and crystal orientation is not of importance.

It was established that the total area fraction of the crack plane covered by graphite particles is equal to 23.9% (cf. **Figure 6.7**). However, this number has to be compared with the average fraction of graphite particles covered in arbitrary planes. 3D analysis shows that the average area fraction of graphite particles for a number of more than 1000 arbitrary planes is equal to 9.4% (with the standard deviation of 3.9%). Furthermore, the comparison of the measured area fraction of graphite particles in the crack path (23.9%) with the average area fraction of graphite particles in the planes parallel to the crack path -excluding the crack path itself- (9.6%) implies that the graphite morphology is nearly isotropic (cf. **Figure 6.11**).

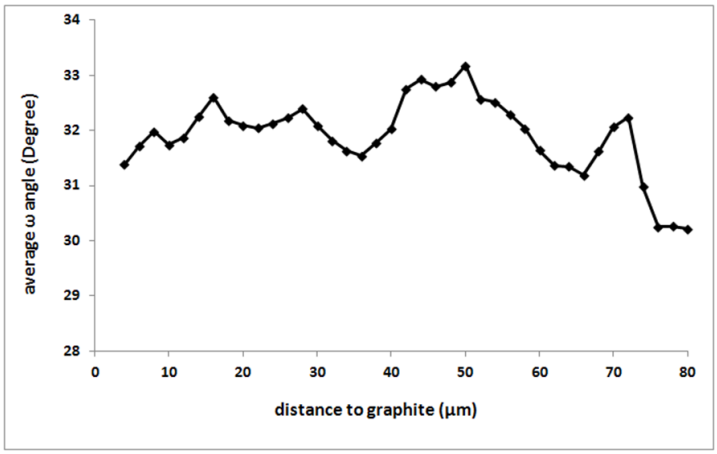

Figure 6.10 Measured deviation angle ω as a function of the distance from graphite particles. Each data point in this graph represents the average of at least 500 observations.

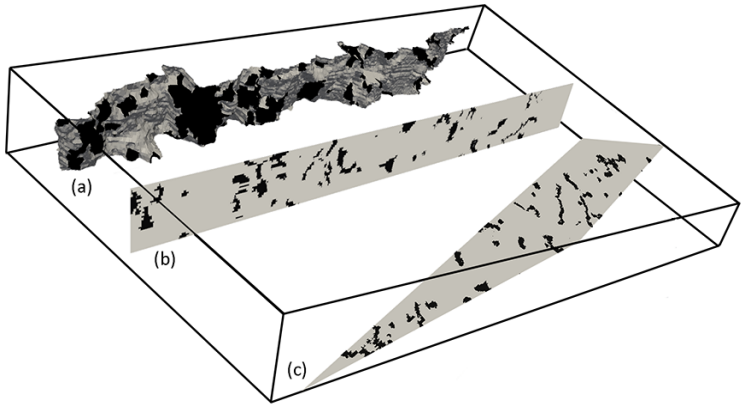

Figure 6.11 Distribution of graphite particles in (a) the crack plane, (b) an arbitrary plane parallel to the crack path and (c) an arbitrary plane inclined to the crack plane.

The present study, based on the precise quantitative microstructural analysis shows that graphite particles are of primary significance for crack propagation. However, it remains to be determined by which interaction mechanism the crack is guided through the metal matrix aiming for the maximum area fraction of graphite particles. In this respect, two main mechanisms might play a role: (i) the stress concentration field around a graphite particle interacts with the stress field at the crack tip, (ii) a delaminated zone at the graphite metal interface represents a small microcrack in the bulk of the metal matrix equally exhibiting a local stress distribution that will interact with the main crack. Considering the observation of graphite delamination which was extensively observed here (cf. **Figure 6.12**), the second hypothesis appears to be more probable [7].

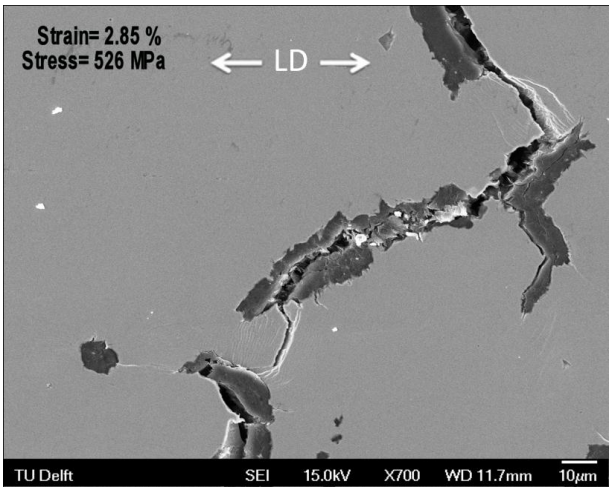

Figure 6.12 Microstructural observation during an in-situ tensile test showing cracks developing at the graphite-matrix interface and also through the graphite layers and growing through the matrix from one graphite particle to another.

This finding may have important technological consequences. In CGI, the graphite particles are of a vermicular morphology randomly distributed in space. The present study tells that graphite particles enhance crack growth. Thus, if it would be possible to design a cast iron with anisotropic distribution of graphite particles in such a way that there are less particles in the direction of crack propagation, perpendicular to the direction of maximum stress then better crack resistance might be obtained. Such an approach only makes sense if the direction of maximum load coincides with the direction of heat transfer.

6.6. Conclusions

Orientation contrast microscopy was employed to provide a deeper insight in the complex crack path morphology observed in compacted graphite iron (CGI) during thermo-mechanical fatigue (TMF) loading conditions. To meticulously characterize TMF crack paths, in relation to microstructural features and to find out how and by which mechanisms the cracks predominantly develop, 3D microscopy observations were employed.

The obtained results did not indicate a particular crystallographic preference of the fracture plane, i.e. the crystal plane parallel to the fracture plane was nearly of random orientation. This conclusion was obtained on the basis of extensive 3D microstructural characterization, in which the entire material volume (~ 1 mm^3) in the vicinity of the crack was mapped by orientation contrast microscopy. Whether or not the fracture plane was considered in the vicinity of a graphite particle did not have any effect on this conclusion.

The microstructural observations show that the graphite particles play a crucial role during crack propagation, as the crack path connects neighboring graphite particles. Quantitative analysis showed that the density of graphite particles on the fracture plane is more than double as high as in any other arbitrary plane of the structure. Hence, it is obviously revealed that crack growth is enhanced by the presence of graphite particles.

6.7. References

1. Hallstein, R., et al., *Thermal-mechanical fatigue behaviour of vermicular cast iron*. Progress in Mechanical Behaviour of Materials, ed. F. Ellying and J.W. Provan. 1999. 301-306.
2. Rundman, K.B., *Cast Irons*, in *Encyclopedia of Materials: Science and Technology (Second Edition)*, K.H.J.B. Editors-in-Chief: , et al., Editors. 2001, Elsevier: Oxford. p. 1003-1010.
3. Seifert, T., et al., *Mechanism-based thermomechanical fatigue life prediction of cast iron. Part II: Comparison of model predictions with experiments.* International Journal of Fatigue, 2010. **32**(8): p. 1368-1377.
4. Seifert, T. and H. Riedel, *Mechanism-based thermomechanical fatigue life prediction of cast iron. Part I: Models.* International Journal of Fatigue, 2010. **32**(8): p. 1358-1367.
5. Davis, J.R. and A.I.H. Committee, *Cast Irons*. 1996: ASM International.
6. Sehitoglu, H., *Thermal and Thermomechanical Fatigue of Structural Alloys*, in *ASM Metals Handbook, Volume 19, Fatigue and Fracture*. 1996, ASM International: , United States of America. p. 1313-1402.
7. Ghodrat, S., *Thermo-Mechanical Fatigue of Compacted Graphite Iron in Diesel Engine Components*. 2013.
8. Ghodrat, S., et al., *Measurement and characterization of Thermo-Mechanical Fatigue in Compacted Graphite Iron.* International Journal of Fatigue, 2013. **48**: p. 319-329.
9. Ghodrat, S., et al., *Effects of Holding Time on Thermomechanical Fatigue Properties of Compacted Graphite Iron Through Tests with Notched Specimens.* Metallurgical and Materials Transactions a-Physical Metallurgy and Materials Science, 2013. **44A**(5): p. 2121-2130.
10. Zaefferer, S., S.I. Wright, and D. Raabe, *Three-dimensional orientation microscopy in a focused ion beam-scanning electron microscope: A new dimension of microstructure characterization.* Metallurgical and Materials Transactions a-Physical Metallurgy and Materials Science, 2008. **39A**(2): p. 374-389.
11. DeHoff, R.T., *Quantitative serial sectioning analysis: preview.* Journal of Microscopy, 1983. **131**: p. 259-263.
12. Lewis, A.C., et al., *Two- and three-dimensional microstructural characterization of a super-austenitic stainless steel.* Materials Science and Engineering a-Structural Materials Properties Microstructure and Processing, 2006. **418**(1-2): p. 11-18.
13. Haehner, P., et al., *Research and development into a European strain-controlled thermo-mechanical code-of-practice for fatigue testing.* International Journal of Fatigue, 2008. **30**(2): p. 372-381.
14. Lee, S.B., A.D. Rollett, and G.S. Rohrer, *Three-dimensional microstructure reconstruction using FIB-OIM*, in *Recrystallization and Grain Growth III, Pts 1 and 2*, S.J.L. Kang, et al., Editors. 2007. p. 915-920.
15. Saylor, D.M., A. Morawiec, and G.S. Rohrer, *Distribution of grain boundaries in magnesia as a function of five macroscopic parameters.* Acta Materialia, 2003. **51**(13): p. 3663-3674.

16. Randle, V. and P. Davies, *Crystallography of brittle fracture and deformation twinning in ferritic steels.* Materials Science and Technology, 2005. **21**(11): p. 1275-1281.

Chapter 7. Deriving the Grain Boundary Character Distribution from 3D EBSD Data

"The most important things in my life, I have learned from people who disagreed with me."

Hadi Pirgazi

7.1. Introduction

Although many microstructural features of materials can be characterized with conventional 2D analytical techniques, there remains a body of important microstructural properties (e.g. detailed grain boundary features) that can only be measured in three-dimensions (3D). The emphasis of this chapter is to derive the grain boundary character distribution from a 3D data set. A general alignment algorithm is proposed to correct for spatial misalignment as well as for misorientation between planar sections. A method is described to represent the grain boundary normal with respect to the crystal reference frame and to represent the grain boundary character distribution in a discretized space in five dimensions.

7.2. Five parameters of Grain Boundary

Five parameters are required to fully describe a grain boundary plane. Three parameters of the orientation change across the grain boundary, which is called the misorientation and includes the crystallographic orientation relationship between the lattices of the adjacent grains. Two additional parameters specify the orientation of the grain boundary plane normal, which is referred to as the grain boundary inclination [1, 2]. Many important properties of materials such as corrosion resistance [2], brittleness and toughness [3] are affected by the precise nature of grain boundaries. The procedure of improving specific material properties by changing the properties of grain boundaries is known as Grain Boundary Engineering (GBE) [2]. For GBE it is necessary to be able to derive, represent and investigate the Grain Boundary Character Distribution (GBCD). The GBCD, $\lambda(\Delta g,n)$, is defined as the relative frequency of occurrence of grain boundaries with specific

type of misorientation (Δg) and boundary plane normal **n** [4]. Three parameters of the misorientation and one parameter of the grain boundary plane normal can be directly derived from the 2D orientation contrast map. The fifth parameter can be estimated from planar sections using stereological method [5], or can be extracted from 3D data. The techniques for 3D characterization of the microstructures are based on two different approaches: (i) observation with high energy radiation [6, 7] and (ii) by serial sectioning [8-10].

Serial sectioning has been the most widely used method to acquire 3D data at the macro/microscale of opaque materials. This technique has been widely used to extract 3D information from magnesia [11], lead-tin alloy [12], Yttria [13], nickel [5, 14] and CuZr alloy [15]. In this technique, a series of closely spaced parallel sections reveal the third dimension of the microstructure. The usual method for serial sectioning involves the cyclic removal of parallel layers of the sample, followed by imaging (e.g. by EBSD) of the planar sections [8, 16]. The removal of the material for serial sectioning can be performed with different methods: e.g. mechanical polishing, chemical polishing, Focused Ion Beam (FIB) tomography and laser or electrical discharge ablation [17]. Independent of the method employed for the preparation of the sections, the serial sectioning technique suffers from the misalignment between consecutive sections, which needs to be accurately corrected before further data processing [18].

The goal of this chapter is to derive the grain boundary character distribution from 3D EBSD data collected by serial sectioning using the mechanical polishing technique.

7.3. Experimental procedures

7.3.1. Material and Three-Dimensional Characterization

A polycrystalline pure nickel sheet with 1.0 mm thickness was used for this study. The sample was annealed for 1 hour in the open atmosphere at a temperature of 1000 °C, which resulted in a bimodal grain structure with many large grains (with grain sizes of 0.3 to 0.9 mm), surrounded by small grains (with an average grain size of 200 µm). As it can be seen in **Figure 7.1**, twins are also evident in the microstructure and the grain boundary analysis reveals that a high majority of grain boundaries (45%) are composed of Coincident Site Lattice (CSL) boundaries, especially grain boundaries carrying the Σ3 type of misorientation (<111>60°).

Wide field 3D Electron Back-Scattering Diffraction (EBSD) was performed on the RD-TD section of the sample by the serial sectioning technique explained in **Chapter 4**. The sample preparation was done by conventional mechanical polishing to remove a layer with a certain thickness (7 µm). After each polishing step, the EBSD measurements was performed in a high resolution FEG-SEM (of type FEI Quanta^{TM} 450®) on a large area (3,200 × 3,200 µm^2) with an in-plane step size of 6 µm to obtain the local crystallographic orientations. In order to meticulously fix the scan area on subsequent layers for EBSD measurements, micro-Vickers indentations were used to mark a grid on the sample. These indentations were also used to measure the thickness of each removed layer.

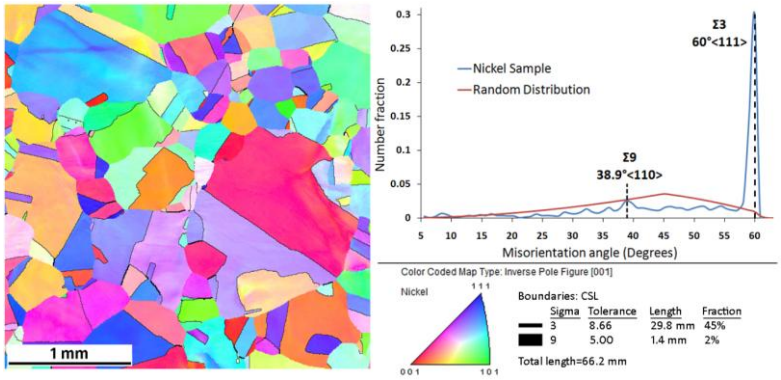

Figure 7.1 ND inverse pole figure map of the Ni sample. The grain boundaries carrying Σ3 and Σ9 types of misorientations are shown with black thin and thick lines, respectively.

7.3.2. Post Processing Analysis

After collecting 50 consecutive sections the 3D volume was reconstructed. Reconstruction was carried out using two algorithms: (i) the first one for precise alignment of the sections and (ii) the second one for the surface meshing of the grain boundary planes by triangulation.

It was found that the 2D EBSD sections in this case were not entirely parallel, which resulted in dimensional distortion between adjacent layers (cf. **Figure 7.2a**). Therefore, the translational alignment procedure (explained in **Chapter 4**) needs to be improved to correct this further misalignment. To this purpose, a two step registration algorithm (which will refer to as the full alignment) was developed. The first step is to correct any spatial translation, rotation and distortion between the layers. In this step, the lower section is kept fixed, but the four corners of the upper section are freely moved in x and y directions (to stretch or shrink the map). Assuming that the distortion in the map is linear, the new coordination of the scan points are calculated from the coordinates of the corners using a bilinear interpolation technique. The calculated values are then truncated in multiples of step size values. For each position of the four corners, the average fit between the two sections was calculated by averaging out the misorientation angle between each pixel in the upper section and its neighboring pixel in the lower section. Finally the position of the four corners, which resulted in the minimum average misorientation between two adjacent sections, is selected as the optimum to obtain the best spatial alignment (cf. **Figure 7.2b**).

The second step of the alignment algorithm is to correct the misorientation between two adjacent sections produced by the rotational and planparallelity misalignment. This can be seen as a difference in inverse pole figure coded colors of the same grains in two consecutive sections (cf. **Figure 7.3a** and **b**). To this purpose, a transformation matrix was composed from individual transformations around RD, TD and ND:

$$T = T_{RD}(\theta_{RD}).T_{TD}(\theta_{TD}).T_{ND}(\theta_{ND}) \qquad 7.1$$

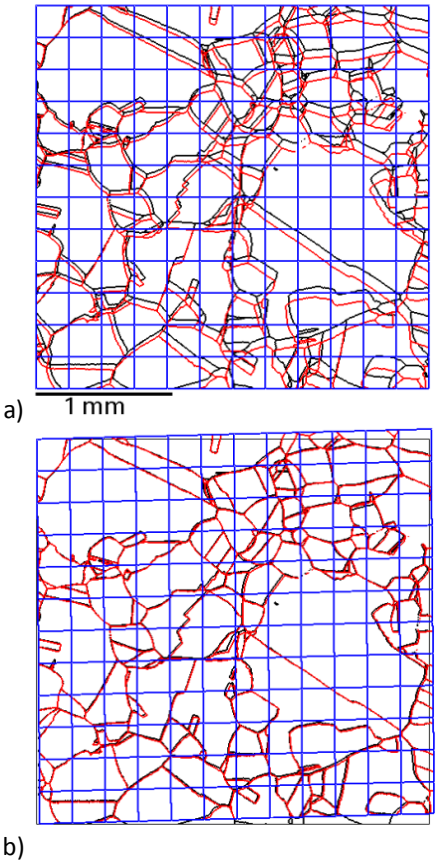

Figure 7.2 Grain boundaries of two consecutive sections, (a) before and (b) after full spatial alignment. The section with the black boundaries is kept fixed, and the other one is moved to acquire the best alignment. The blue grid represents the distortion correction which has been applied on the moving section (with red grain boundaries).

where $T_{RD}(\theta_{RD})$ is a transformation of θ_{RD} around the RD axis (and equally for $T_{TD}(\theta_{TD})$ and $T_{ND}(\theta_{ND})$). The θ values were changed between -5° and 5° with 0.1° step. For all points in the upper EBSD scan, the orientations were transformed by the T matrix and the average misorientation angle between two sections was calculated. Finally the transformation matrix which resulted in the minimum average misorientation between two adjacent sections is chosen to correct the misorientation caused by the misalignment. The two steps of the alignment algorithm were performed repeatedly until no further correction was required. **Figure 7.3** shows the results of the mentioned alignment procedure. It can be seen that any misalignment, i.e. translational, rotational and planparallelity (in case of 2 non-parallel consecutive sections, which usually appears as a stretched image in the EBSD map) have been largely corrected (cf. **Figure 7.3c**).

The second algorithm was used for grain boundary plane triangulation. To this purpose, two grain boundaries between two pairs of corresponding triple junctions were divided into equal segments and triangulation was carried out based on an

algorithm proposed by Saylor et al [19]. This procedure was explained in detail in **Section 4.3.2.3** of **chapter 4.**

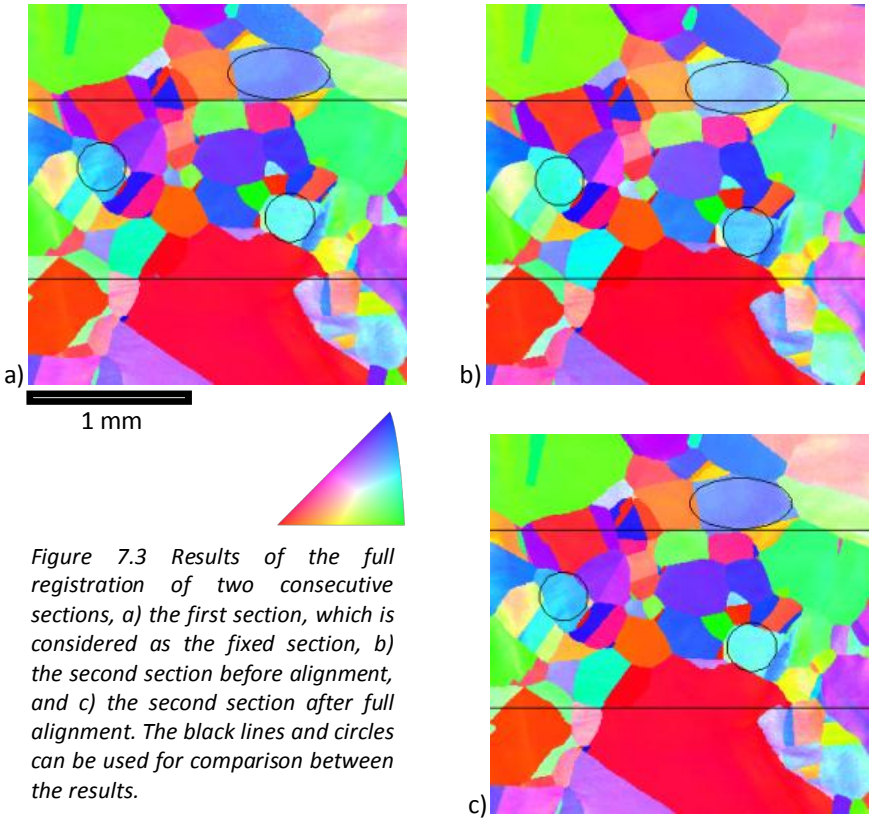

Figure 7.3 Results of the full registration of two consecutive sections, a) the first section, which is considered as the fixed section, b) the second section before alignment, and c) the second section after full alignment. The black lines and circles can be used for comparison between the results.

7.4. Results and Discussions

7.4.1. Aligned 3D microstructure

Figure 7.4 shows the 3D volume of the reconstructed microstructure before alignment, after translational alignment (by shifting one section along RD and TD with respect to the other section, as proposed by Lee et al. [20]), and after full alignment (as applied in this study). In the original results (i.e. before alignment, cf. **Figure 7.4a**), there are discontinuities in grain orientations and boundary planes are ledged. The translational alignment (cf. **Figure 7.4b**) makes grain boundaries smoother but abrupt changes of orientation between sections remain. The full alignment (cf. **Figure 7.4c**) improves not only boundary curvatures but also leads to more continuous orientation gradients in the grains. This observation was quantitatively analyzed by computing the average misorientation between the corresponding pixels of the adjacent sections. The results indicate that the full alignment reduces this misorientation from 10.0° (for the original results) and 5.8° (after translational alignment) to 2.8°.

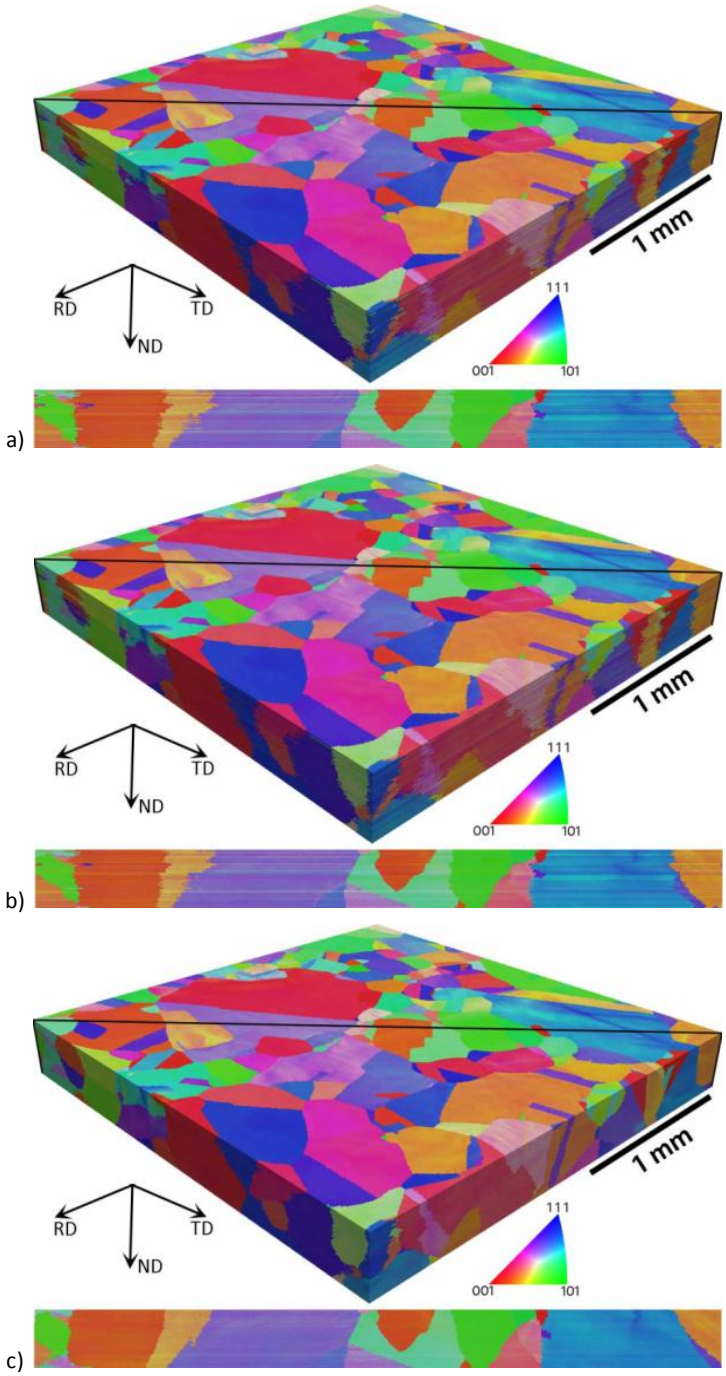

Figure 7.4 ND inverse pole figure volume of the reconstructed microstructure together with the cross section of the specified plane (black lines), a) the stack of the original EBSD data without any alignment, b) after translational alignment, and c) after full alignment. The size of this volume is 3,000×3,000×350 μm^3, and it contains 470 grains.

7.4.2. Grain boundary surface mesh

The grain boundary fitting technique presented in **Section 4.3.2.3**, fits a polynomial function on the grain boundary points of each section. However, the triple junctions are considered as fixed points and their coordinates are constrained to the scan grid. This results to a sub-step size misalignment between consecutive sections, which will introduce errors in the calculation of grain boundary normals. This situation is schematically presented in **Figure 7.5**. For simplicity, the ideal trace of a grain boundary in the X-Z plane is depicted in **Figure 7.5a**. As the experimentally observed grain boundary in each section is constrained to the scan grid, the grain boundary trace after connecting every single neighboring section will be as plotted in **Figure 7.5b**. The arrows are the normals to each segment of the grain boundary and their length is proportional to the length of the grain boundary segment. The distribution of the angle between the grain boundary segments and the ideal configuration has been presented in the same figure. As it can be seen, when the grain boundary is constructed by connecting every single neighboring section, there will be a large deviation between the normal to each segment and the ideal configuration. However, by making the connection between every two, three or four sections, the deviation angle continuously decreases (cf. **Figure 7.5c** to **e**).

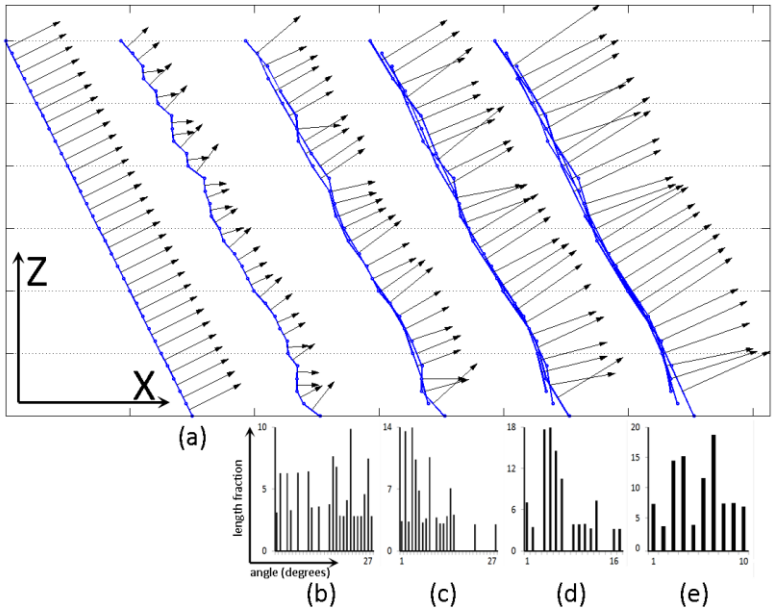

Figure 7.5 Schematic representation of reconstructing a grain boundary in the X-Z plane. (a) The ideal configuration, (b) reconstructed by connecting every single neighboring section, (c to e) reconstructed by connecting every 2nd, 3rd and 4th sections, respectively. The arrows show the normal to each boundary segment and are scaled to the length of the segment. The graphs show the deviation angle of the segment normals with respect to the ideal configuration.

Figure 7.6 represents the previously mentioned boundary construction procedure

in 3D. As it can be seen, by performing the triangulation between every two, three and four sections, a smother grain boundary is reconstructed. In these images, for simplicity, only one set of triangles has been plotted. For example, in **Figure 7.6c** which is the result of the triangulation between every three section, only the triangles constructed between sections 1, 4, 7 , … has been plotted (the other sets of triangles in this case are between sections 2, 5, 8 , … and between sections 3, 6, 9 , …). The distribution of grain boundary normals in the sample reference frame (X-Y-Z) is shown in **Figure 7.7**. These distributions represent the stereographic projection of the normal to each triangle in the sample reference frame, considering the area of each triangle as the weight factor. Considering the fact that the considered grain boundary plane has three large planar facets, which are parallel to each other, it is expected to have a high intensity pole in the distribution. It can be seen that by increasing the interval between the sections, a less scattered distribution with higher intensity appears. However, the difference between intervals of two to four sections (cf. **Figure 7.7b** and **d**) is not considerable. On the other hand, by increasing the interval between the sections, the matching fraction (cf. **Section 4.3.2.3** of **Chapter 4**) of triple junctions between two sections drops from 70% to 50% for intervals of one and four, respectively. Therefore, the best configuration for grain boundary triangulation was found between every two sections, which includes at least 65% of matched triple junctions between neighboring sections and results in a reliable grain boundary pole distribution.

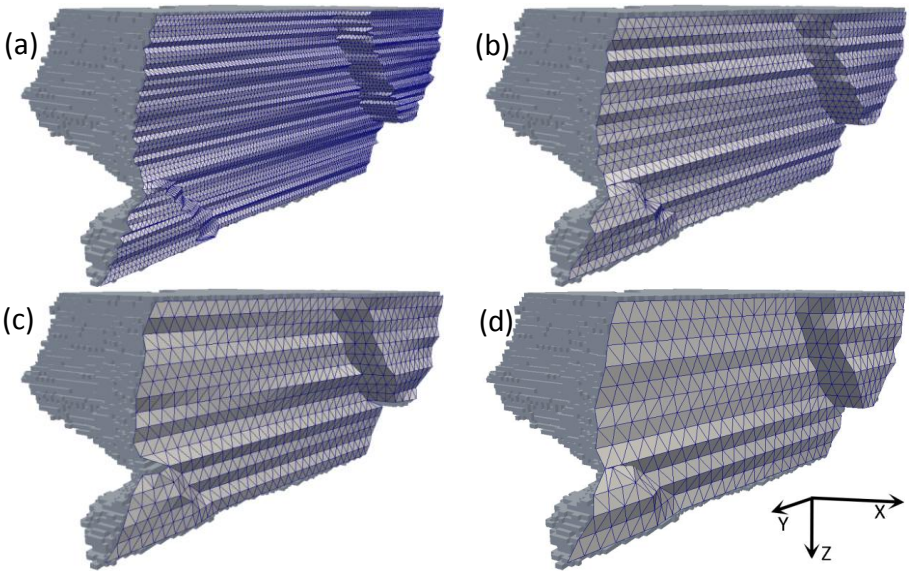

Figure 7.6 Surface meshing of the grain boundary planes by triangulation between every (a) one, (b) two, (c) three and (d) four sections.

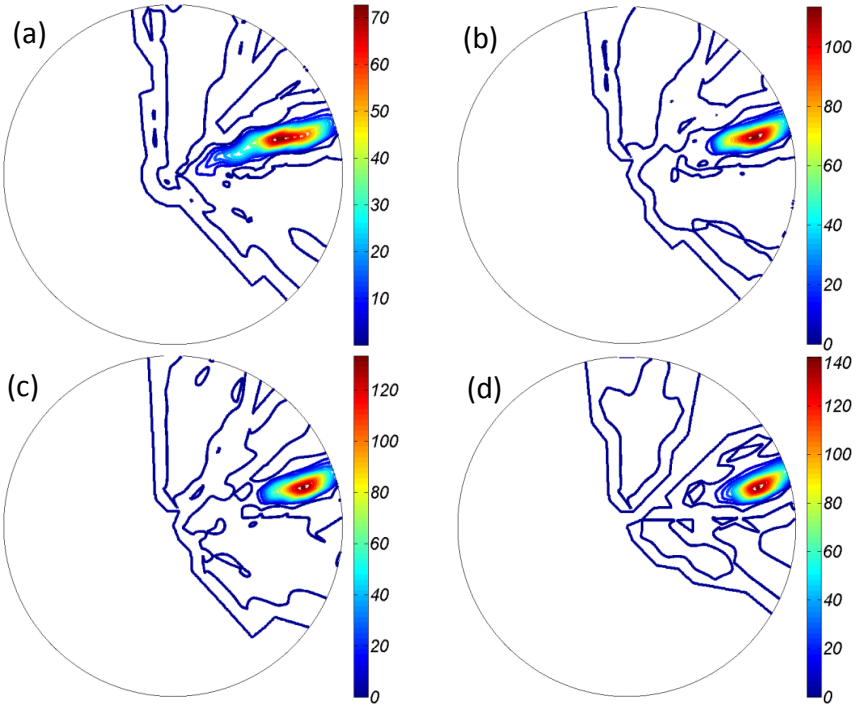

Figure 7.7 Distribution of the grain boundary normals with respect to the sample reference frame corresponding to the surface meshes presented in Figure 7.6. The color bar is based on multiples of random distribution (MRD).

7.4.3. Grain boundary character distribution (GBCD)

The reconstructed (triangulated) grain boundary planes are used to derive the grain boundary character distribution, i.e. the relative frequency of occurrence $\lambda(\Delta g,n)$ of a grain boundary with specific type of misorientation and normal to the plane. Each triangle in the mesh is classified with the misorientation of the grains on both sides (Δg) and the normal to the grain boundary in the crystal reference frame (n_c). Although $\lambda(\Delta g,n)$ is a continuous functions, for calculation it is more convenient to represent it as a finite set of discrete grain boundary types. In the followings, the discretization techniques for partitioning of the misorientation and grain boundary normal space have been explained.

In this research, the crystallographic misorientations are represented by Euler angles. The entire misorientation space is from 0° to 360°, 180° and 360° for φ_1, Φ and φ_2, respectively. It is proposed in the literatures [21, 22] to parameterize this space by φ_1, cosΦ and φ_2 in the ranges of (0 to 360°), (-1 to 1) and (0 to 360°), respectively. This parameterization allows further partitioning into equal volume units. Here, the φ_1 and φ_2 parameters have been divided into 36 parts with 10° distance. The cosΦ parameter has been divided into 18 parts with 1/9 distance (cf. **Figure 7.8**). Consequently, the continuous function of misorientation will be approximated by 23,328 (36×18×36) discrete set of misorientation types.

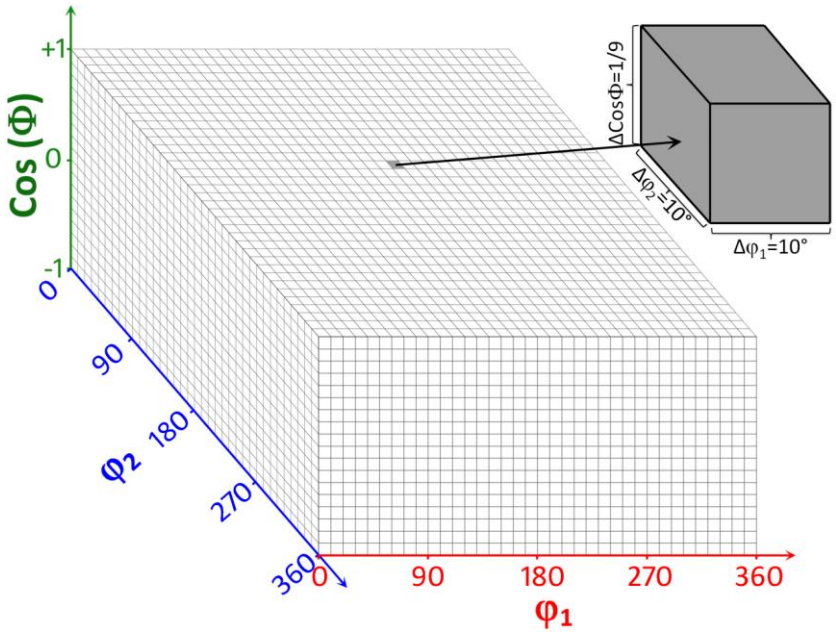

Figure 7.8 Discretization of the entire parameterized Euler space for approximation of misorientation types across the grain boundaries. The entire volume has been discretized into 23,328 (36×36×18) equal volume cells.

The entire space of the grain boundary normal, which can be represented on a unit sphere, was also partitioned into equal area units. To this purpose, the method proposed by Gringorten and Yepez [23] was used to divide the unit sphere into equal area cells. **Figure 7.9** shows the equal area grid used for partitioning the grain boundary normal space. This continuous space is divided in 722 equal area cells (361 in each hemisphere), and therefore the continuous functions of grain boundary will be approximated by over 16 million (23,328×722) discrete grain boundary types.

After the proper discretization of the grain boundary parameters, the computation of the GBCD function can be started by calculating the misorientation on both sides of each triangle (i.e. g_1 and g_2). As in cubic crystals there are 24 symmetrically equivalent orientations for a given orientation (g), thus there will be 24^2 equivalent misorientations with respect to g_1 (cf. **Equation 7.2**)

$$\Delta g_{1-2} = O_i \, g_1 \, (O_j \, g_2)^{-1} \qquad 7.2$$

whereby O_i and O_j are the crystal symmetry operators. Taking into account the misorientations with respect to g_2 (cf. **Equation 7.3**), leads to another 24^2 equivalent misorientations.

$$\Delta g_{2-1} = O_i \, g_2 \, (O_j \, g_1)^{-1} \qquad 7.3$$

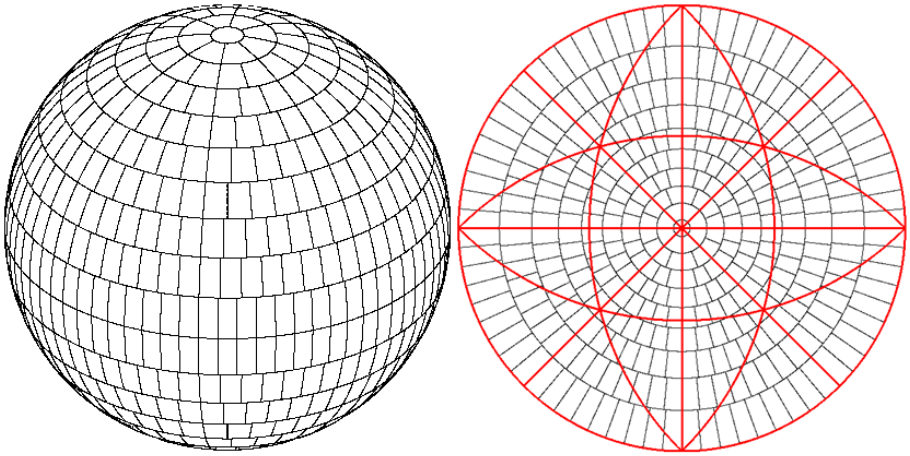

Figure 7.9 Equal area grid employed for binning the surface of the grain boundary normal space (left) and the corresponding stereographic projection (right). The entire surface of the sphere has been divided into 722 equal area cells (361 in each hemisphere). Red_lines denote the 24 symmetrically equivalent areas of crystallographic directions.

Therefore, for a single triangle there will be 2×24^2 equivalent misorientations which can be located in the appropriate cells of the discretized misorientation space. For each calculated misorientation, the normal to the grain boundary in the crystal reference frame (n_C) is calculated using the vector perpendicular to the surface of the triangle as the local normal to the grain boundary plane in the sample coordinate system (n_S) and the orientation matrix of the non-inversed grain in **Equations 7.2 and 7.3**. For example, in the case that the misorientation has been calculated using **Equation 7.2,** the corresponding normals will be calculated by the **Equation 7.4**.

$$N_C = \pm O_i \; g_1 \; n_S \qquad 7.4$$

The (±) sign in this equation is due to the fact that it is arbitrary whether the grain boundary normal is pointed to each side of the grain boundary plane. Considering these two normals, $2\times2\times24^2$ equivalent grain boundary types will be generated for each triangle in the grain boundary surface mesh. The calculated boundary normals are then located in the appropriate cells of the discretized grain boundary normal space and the area of the triangle is added to that cell. In order to expresses the results in units of Multiples of Random Distribution (MRD), the area in each cell is divided by the average area per cells (i.e. the total area of all cells divided by the number of cells). With this representation, if the value associated with a specific type of grain boundary is greater than one, it means that the total area of that type of grain boundary is larger than would be expected for the random distribution.

Visualization of the 5D grain boundary character distribution ($\lambda(\Delta g,n)$) is challenging. One way is to plot the distribution of the grain boundary normals averaged over the entire misorientation space (i.e. ($\lambda(n)$). **Figure 7.10** shows the distribution of $\lambda(n)$ plotted in the stereographic projection.

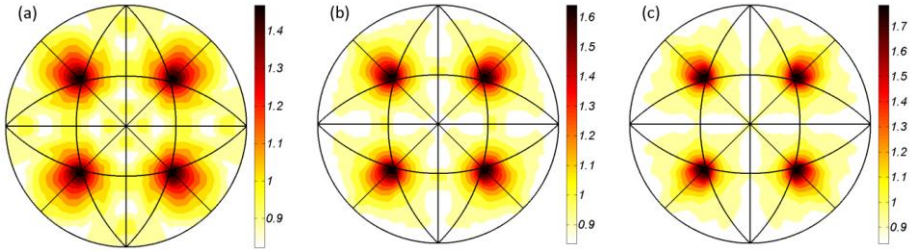

Figure 7.10 (a to c) Distribution of grain boundary normals averaged over the entire misorientation space after surface meshing between every single, two and three sections, respectively. The color bar is expressed in multiples of random distribution (MRD).

The three distributions represented in **Figure 7.10** are the results of the grain boundary surface meshing between every single, two and three planar sections. Considering that these distributions have been plotted in the crystal reference frame, it can be seen that in all of them the maximum occurs at {111}nd[orientations. However, the results show that by increasing the interval between planar sections from one to two (figure a and b), a less scattered distribution with higher intensity is obtained. These differences are less significant after further increase of the interval between sections to three layers (cf. **Figure 7.10c**).

Another way to visualize the five dimensional grain boundary parameters is by plotting the distribution of grain boundary normals for a specific type of misorientation. As it can be seen from the 2D analysis (cf. **Figure 7.1**) approximately 45% of the total population of the grain boundaries in this material are of Σ3 (i.e. 60°@{111}) type of misorientation. Therefore, the focus is only on the grain boundaries carrying this one specific misorientation. **Figure 7.11** shows the distribution of grain boundary normals for Σ3 type of misorientation. Similar to **Figure 7.10**, this figure represents the data obtained by different triangulation intervals and as it was expected, by increasing the sections interval, the intensity of the distributions increases. On the other hand, only in **Figure 7.11a** small traces of tilt boundaries are evident. The presence of these tilt boundaries might be caused by wrongly indexed grain boundary normals due to the non-smooth grain boundary plane. As it can be seen, by increasing the section interval during triangulation (which results in a smoother grain boundary plane), no more traces of tilt grain boundary are evident. In **Figure 7.11d**, the position of pure twist and pure tilt boundaries have been marked by the red circle and the blue line, respectively. In a pure twist boundary, the grain boundary normal is parallel to the misorientation axis ({111} in case of Σ3 misorientation) and in a pure tilt boundary, the grain boundary normal is perpendicular to the misorientation axis [1].

This figure can be used to investigate whether the Σ3 grain boundaries are coherent or incoherent twin boundaries. In a coherent twin boundary, the grain boundary plane is parallel to a common {111} plane of both crystals. At a coherent twin boundary, the regular stacking sequence of close-packed {111} planes inverts and the nearest and next nearest neighbor coordination are unchanged. Therefore, the energy of coherent twin boundaries is very small and they appear as straight boundaries. Due to the very small energy, the coherent twin boundaries are

relatively immobile. If a Σ3 grain boundary plane is not parallel to the {111} crystallographic plane in both intersecting grains, the twin is called incoherent twin boundary [24].

Figure 7.11 shows a maximum on the <111> pole, which is perpendicular to the {111} crystallographic plane. This means that the grain boundary planes of the Σ3 type are predominantly bounded by {111} crystal planes at both sides. This indicates that the majority of Σ3 grain boundaries are coherent twin boundaries. Similar results, obtained by serial sectioning using the FIB tomography technique, have been reported by Rohrer et al. [5] for IN100 nickel base superalloys. They have concluded that the important factors for a precise derivation of the grain boundary character distribution from 3D EBSD data are the alignment of the 2D sections, the ratio of the out-of-plane to in-plane spacing (in this research this factor was considered as the interval between the 2D sections during grain boundary surface meshing) and the discretization of the grain boundary space.

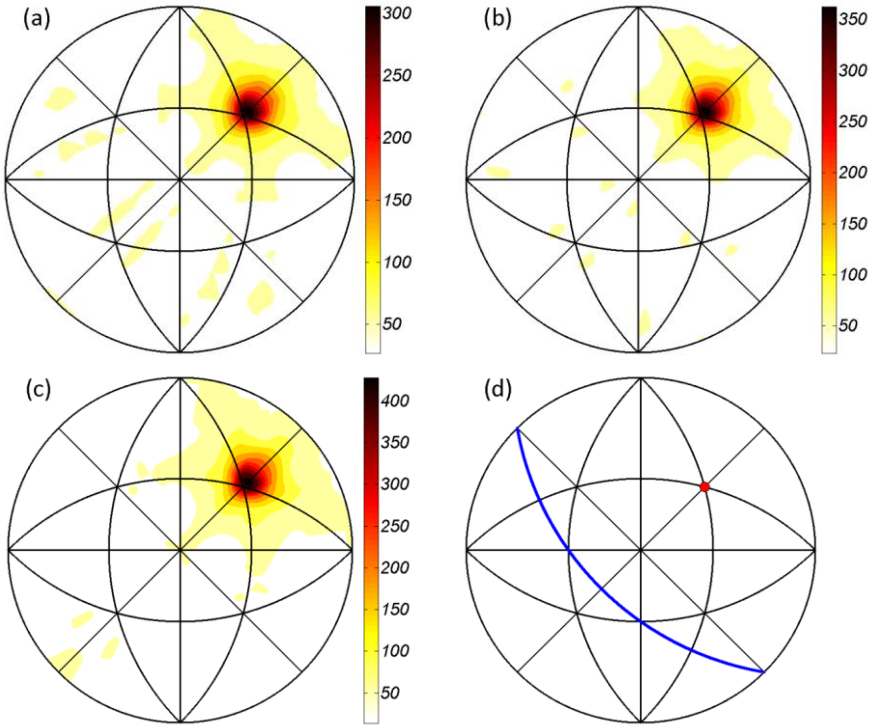

Figure 7.11 (a to c) Distribution of grain boundary normals for Σ3 type of misorientation after surface meshing between every single, two and three sections, respectively. (d) Position of the normal of pure twist (red circle) and pure tit (blue curve) grain boundaries with Σ3 type of misorientation. The color bar is expressed in multiples of random distribution (MRD).

To select a specific type of misorientation, one may work with a threshold such as Brandon's criterion. According to this criterion the maximum permissible deviation from coincidence is given by an equation of the form $\theta=\theta_0(\Sigma)^{-1/2}$, where $\theta_0\approx15°$ [25].

Therefore, for the Σ3 misorientation, the maximum permissible deviation is 8.66°. The Σ3 misorientation can be represented by the Euler angles φ_1=45°, Φ=70.53° and φ_2=45°. If the mis-misorientation angle (the term mis-misorientation is used to describe the orientation distance between two misorientations) between a misorientation and the Σ3 misorientation is less than 8.66°, it is considered as a Σ3 misorientation. **Figure 7.12** shows he locus of the Σ3 misorientations together with the distribution of misorientations for 4 consecutive sections from the 3D stack and the grid which was used to discretized the parameterized misorientation space. As it can be seen, the Σ3 misorientation locus has an ellipsoid shape, which intersects with 28 cells of the discretized misorientation space (the space shown in the figure is a 3×3×4 cell structure and the Σ3 misorientation locus does not intersect with the eight cells on the corners).

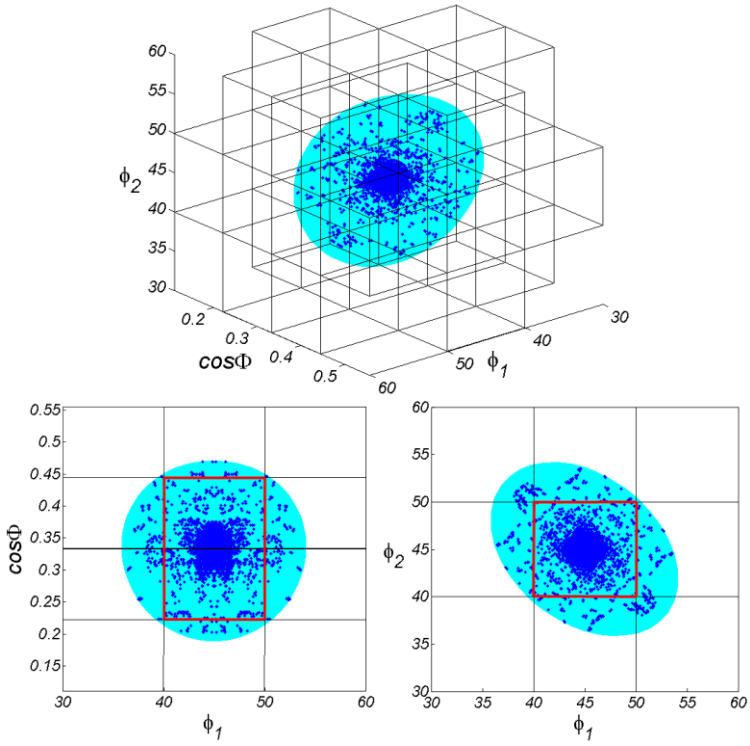

Figure 7.12 (top) Experimental (blue dots) and calculated (cyan ellipsoid) misorientations within the threshold of Brandon's criterion (8.66°) for the Σ3 misorientation. The distributions have been plotted in the discretized misorientation space employed in this study. (bottom) Two different views of the top volume for better visualization.

To derive the character distribution of grain boundaries carrying Σ3 type of misorientation, one may consider only the two highly populated cells (marked by red lines in **Figure 7.12**) which are entirely in-locus (as was done by the distributions presented in **Figure 7.11**). The volume of these two cells only occupies

47% of the volume of the Σ3 locus, and as the rest of the volume of the locus is less populated, the derived distribution might express a significantly high intensity.

Another possibility is to include all 28 cells intersecting with the Σ3 locus in the calculations. However, as a considerable fraction of many of these cells does not belong to the Σ3 locus, a significantly lower intensity will be expected. Although a very fine discretization may solve this problem, it needs practically impossible calculation time and significantly more independent observations to populate the cells.

Our suggestion to solve this problem is to include all and only the in-locus misorientations to calculate the GBCD. To this purpose, the mis-misorientations between the Σ3 and all 2×24×24 misorientations (between two orientations on both sides of a boundary) are calculated. These misorientations are divided into two groups, i.e. inside and outside the Σ3 locus. For the ones which are inside the locus, the grain boundary normal in crystal coordinate system is calculated and located in the appropriate cell of the grain boundary normal space (the same as the previously explained technique). The following equation is then used to calculate the intensity in each cell based on the MRD:

$$I_i = \frac{A_i}{A_R} = \frac{A_i}{\frac{A_t}{\frac{V_t}{V_{\Sigma 3}} \times 722}} = \frac{A_i}{\frac{A_t}{\frac{259{,}200}{47.43} \times 722}} \qquad 7.5$$

In this equation A_i is the total area of grain boundaries in cell i. A_R is the total area of grain boundaries in one cell if the distribution was random. As it can be seen, A_R is the result of dividing the total area of grain boundaries in all cells by the total number of cells. The number 259,200 (360×360×2) is the volume of the entire parameterized misorientation space, i.e. φ_1, cosΦ and φ_2 with the range of (0 to 360°), (-1 to 1) and (0 to 360°), respectively. The other two numbers, i.e. 47.43 and 722 are the volume of the Σ3 locus and the total number of cells of the discretized grain boundary normal space (cf. **Figure 7.9**), respectively. The volume confined by the Σ3 locus is calculated by a standard MATLAB procedure, which allows to calculate the volume contained by a given convex hull.

The results of the above mentioned methods have been presented in **Figure 7.13.** Note that all the distributions in this figure have been derived from the same triangulated surface. Although the distributions are very similar, as it was expected, the distribution based on the two highly populated cells of the Σ3 misorientation (cf. **Figure 7.13a**) shows a very high intensity, whereas the distribution based on all the intersecting cells with the Σ3 locus (cf. **Figure 7.13b**) shows a very low intensity. As it can be seen, using the method base on the misorientations inside the locus of

the Σ3, a distribution with the maximum intensity between the previous two distributions is obtained (cf. **Figure 7.13c**) and regarding the differences discussed on **Figure 7.12**, we believe that this distribution shows the correct intensity.

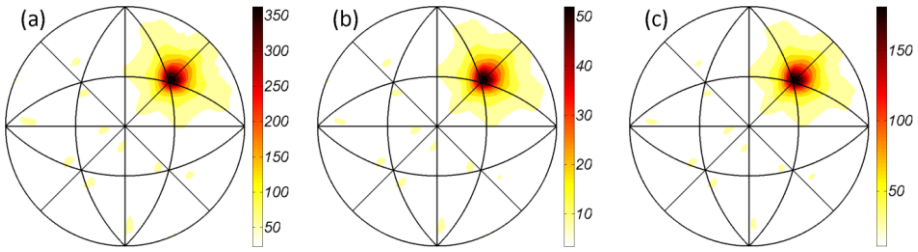

Figure 7.13 Distribution of grain boundary normals for the Σ3 type misorientation after surface meshing between every two sections. (a) Considering only the two highly populated cells, (b) Considering all the cells intersecting with the Σ3 misorientation locus (28 cells).(c) Considering only the misorientations inside the locus. The color bar is expressed in multiples of random distribution (MRD).

The method presented here can be used to derive the GBCD of any other type of misorientation with desired threshold. Especially for high-Σ CSL boundaries in which the Brandon's criterion is smaller. For example, for Σ9 type of misorientation, the Brandon's criterion tolerance is 5°. If we use the discretization technique (10° for φ_1 and φ_2, and 1/9 for cosΦ) the locus of the Σ9 misorientation intersects with 6 cells. As it can be seen in **Figure 7.14**, none of these cells is entirely inside the misorientation locus. This means that some non-Σ9 misorientations will be included in the calculations. This problem will be solved using the presented technique based on the in-locus misorientations, or a finer discretization. Self-evidently the latter costs significantly higher computations which is not the case for the former.

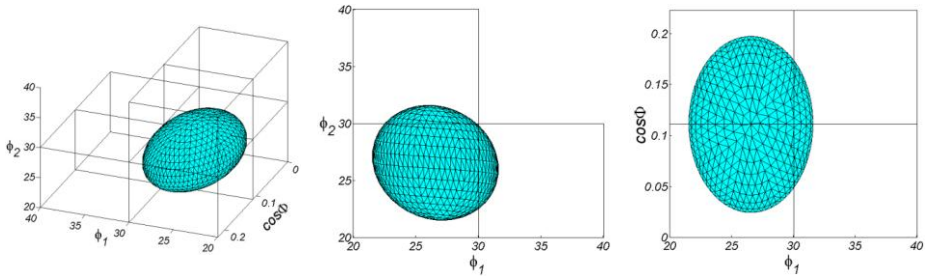

Figure 7.14 (left) The locus of misorientations not exceeding the threshold of Brandon's criterion (5°) for the Σ9 misorientation. (middle and right) Two different views for better visualization.

7.5. Conclusions

Serial sectioning by mechanical polishing was used to collect 50 planar EBSD sections from a pure nickel sample. A two step alignment algorithm was employed

to correct any misalignment including translation, rotation and distortion as well as the misorientation between the adjacent sections. The results showed that this full alignment procedure produces smoother grain boundary planes and continuous orientation gradients inside the grains. The latter could not be achieved with the conventional alignment technique, which includes only translational correction.

The triangulation technique was used to derive the grain boundary surface mesh. It was shown that by performing the triangulation between every other section instead of every single neighboring section, a less scattered distribution of grain boundary poles was obtained resulting in an increased intensity in the representation space.

The grain boundary character distribution was calculated by discretization of the misorientation space and the grain boundary normal space. It was found that the grain boundary planes of Σ3 type are predominantly parallel to {111} crystal planes on both sides, which indicates that the majority of the Σ3 grain boundaries are coherent twin boundaries.

Considering the disadvantages of existing discretization technique, a different method was presented based on exclusively considering the misorientations inside the tolerance locus associated with the misorientation under consideration, e.g. the $\Sigma 3$ misorientation. It was shown that with this new approach, the GBCD of misorientations with small tolerances can be precisely derived without the need of a very fine discretization of the representation space, which would be computationally very expensive.

7.6. References

1. Randle, V. and I.o. Materials, *The Role of the Coincidence Site Lattice in Grain Boundary Engineering*. 1996: Institute of Materials.
2. Randle, V., *Grain boundary engineering: an overview after 25 years.* Materials Science and Technology, 2010. **26**(3): p. 253-261.
3. Watanabe, T. and S. Tsurekawa, *Toughening of brittle materials by grain boundary engineering.* Materials Science and Engineering: A, 2004. **387–389**(0): p. 447-455.
4. Saylor, D.M., et al., *Measuring the five-parameter grain-boundary distribution from observations of planar sections.* Metallurgical and Materials Transactions a-Physical Metallurgy and Materials Science, 2004. **35A**(7): p. 1981-1989.
5. Rohrer, G.S., et al., *Deriving grain boundary character distributions and relative grain boundary energies from three-dimensional EBSD data.* Materials Science and Technology, 2010. **26**(6): p. 661-669.
6. Gault, B., et al., *Atom Probe Microscopy*. 2012: Springer.
7. Miller, M.K., *Atom Probe Tomography*, in *Handbook of Microscopy for Nanotechnology*, N. Yao and Z.L. Wang, Editors. 2005, Kluwer Academic Publisher. p. 227-246.
8. DeHoff, R.T., *Quantitative serial sectioning analysis: preview.* Journal of Microscopy, 1983. **131**: p. 259-263.
9. Zaefferer, S., S.I. Wright, and D. Raabe, *Three-dimensional orientation microscopy in a focused ion beam-scanning electron microscope: A new dimension of microstructure characterization.* Metallurgical and Materials Transactions a-Physical Metallurgy and Materials Science, 2008. **39A**(2): p. 374-389.
10. Uchic, M., et al., *An Automated Multi-Modal Serial Sectioning System for Characterization of Grain-Scale Microstructures in Engineering Materials*. Proceedings of the 1st International Conference on 3d Materials Science, ed. M. DeGraef, et al. 2012. 195-202.
11. Saylor, D.M., A. Morawiec, and G.S. Rohrer, *The relative free energies of grain boundaries in magnesia as a function of five macroscopic parameters.* Acta Materialia, 2003. **51**(13): p. 3675-3686.
12. Rowenhorst, D.J. and P.W. Voorhees, *Measurement of Interfacial Evolution in Three Dimensions.* Annual Review of Materials Research, Vol 42, 2012. **42**: p. 105-124.
13. Dillon, S.J. and G.S. Rohrer, *Characterization of the Grain-Boundary Character and Energy Distributions of Yttria Using Automated Serial Sectioning and EBSD in the FIB.* Journal of the American Ceramic Society, 2009. **92**(7): p. 1580-1585.
14. Li, J., S.J. Dillon, and G.S. Rohrer, *Relative grain boundary area and energy distributions in nickel.* Acta Materialia, 2009. **57**(14): p. 4304-4311.
15. Khorashadizadeh, A., et al., *Five-Parameter Grain Boundary Analysis by 3D EBSD of an Ultra Fine Grained CuZr Alloy Processed by Equal Channel Angular Pressing.* Advanced Engineering Materials, 2011. **13**(4): p. 237-244.

16. Alkemper, J. and P.W. Voorhees, *Quantitative serial sectioning analysis.* Journal of Microscopy-Oxford, 2001. **201**: p. 388-394.
17. Echlin, M.P., et al., *A New Femtosecond Laser-Based Tomography Technique for Multiphase Materials.* Advanced Materials, 2011. **23**(20): p. 2339.
18. Uchic, M.D., *Serial Sectioning Methods for Generating 3D Characterization Data of Grainand Precipitate-Scale Microstructures*, in *Computational Methods for Microstructure-Property Relationships*, S. Ghosh and D. Dimiduk, Editors. 2011, Springer US. p. 31-52.
19. Saylor, D.M., A. Morawiec, and G.S. Rohrer, *Distribution of grain boundaries in magnesia as a function of five macroscopic parameters.* Acta Materialia, 2003. **51**(13): p. 3663-3674.
20. Lee, S.B., A.D. Rollett, and G.S. Rohrer, *Three-dimensional microstructure reconstruction using FIB-OIM*, in *Recrystallization and Grain Growth III, Pts 1 and 2*, S.J.L. Kang, et al., Editors. 2007, Trans Tech Publications Ltd: Stafa-Zurich. p. 915-920.
21. Saylor, D.M., et al., *Distribution of grain boundaries in SrTiO3 as a function of five macroscopic parameters.* Journal of the American Ceramic Society, 2004. **87**(4): p. 670-676.
22. Rohrer, G.S., et al., *The distribution of internal interfaces in polycrystals.* Zeitschrift Fur Metallkunde, 2004. **95**(4): p. 197-214.
23. Gringorten, I.I., P.J. Yepez, and U.P. Laboratory, *The Division of a Circle Or Spherical Surface Into Equal-area Cells Or Pixels*. 1992: Phillips Laboratory, Directorate of Geophysics.
24. Wolf, U., et al., *THE INFLUENCE OF GRAIN-BOUNDARY INCLINATION ON THE STRUCTURE AND ENERGY OF SIGMA=3 GRAIN-BOUNDARIES IN COPPER.* Philosophical Magazine a-Physics of Condensed Matter Structure Defects and Mechanical Properties, 1992. **66**(6): p. 991-1016.
25. Brandon, D.G., *The structure of high-angle grain boundaries.* Acta Metallurgica, 1966. **14**(11): p. 1479-1484.

Chapter 8. Conclusions and Suggestions for Future Research

"To be suspicious is not a fault. To be suspicious all the time without coming to a conclusion is the defect."

Lu Xun (Chinese writer 1881-1936)

8.1. Conclusions

In this thesis, serial sectioning by mechanical polishing was successfully performed on different materials: non-oriented electrical steels, compacted graphite iron and pure nickel. The consecutive two-dimensional EBSD sections were collected to reconstruct the images of the three-dimensional microstructure. The sections were aligned based on the principle of minimum average misorientation between adjacent sections. The developed technique and algorithms were employed to study material properties that depend on the 3D characteristics of the microstructure. These are the main conclusions of this work:

- Serial sectioning by mechanical polishing is an applicable method to obtain large scale 3D microstructures of different metals and alloys, covering a sampled material volume of several mm^3, and thus with statistically relevant data.

- The proposed alignment algorithm, which further expands on a previously published version, can be used to precisely correct for translational, rotational and stretching misalignment between the 2D sections. This alignment procedure produces a smooth grain boundary plane and continuous orientation gradients inside the grains, as corresponding to real 3D microstructures. The latter could not be achieved with conventional alignment techniques, which only include translational correction.

- The triangulation technique was used to derive the grain boundary surface mesh. It was shown that by performing the triangulation between every other section instead of between every single neighboring section, a less scattered distribution of grain boundary poles is obtained in the representation space,

consequently producing maxima of higher intensity.

- The 3D network of reconstructed boundaries was found to be a very useful tool to study the interaction between magnetic domains and grain boundaries. The results showed that by taking into account the density of magnetic free poles at grain boundary planes, a more precise model can be derived of the magnetization behavior of non-oriented electrical steels.

- The serial sectioning technique was employed to provide a deeper insight in the complex crack path morphology observed in compacted graphite iron during thermo-mechanical fatigue loading conditions. The obtained results did not indicate a particular crystallographic preference of the fracture plane, i.e. the crystal plane parallel to the fracture plane was nearly of random orientation.

- 3D microscopy observations also showed that the graphite particles play a crucial role during crack propagation, as the crack path connects neighboring graphite particles. Quantitative analysis showed that the density of graphite particles on the fracture plane is more than double as high as in any other arbitrary plane of the structure. Hence, it is obviously revealed that crack growth is enhanced by the presence of graphite particles.

- A 3D data set was used to derive the grain boundary character distribution of a pure nickel sample. The grain boundary character distribution was calculated by discretization of the misorientation space (in equi-volume bins) and the grain boundary normal space (in equi-area bins). It was found that the grain boundary planes of Σ3 (<111>60°) misorientations are dominantly parallel to {111} crystal planes on both sides, which indicates that the majority of Σ3 grain boundaries are of coherent type.

- Considering the disadvantages of the discretization technique, an alternative method was presented based on the misorientations confined to a tolerance locus associated with the misorientation under consideration. It was shown that with this new approach, the grain boundary character distribution of misorientations with small tolerances can be precisely derived without the need of a very fine discretization mesh, which would be computationally very expensive.

8.2. Suggestions for Future Research

This study is only a modest contribution to the research on the application of serial sectioning for 3D characterization of metal microstructures. There still remain many research topics in this field to be addressed. Some suggestions are:

- By the time of this work, most of research works on 3D characterization have been performed on single phase materials. Perhaps an interesting idea is to employ the developed techniques to study the grain boundary and phase boundary distribution in two-phase and multi-phase materials. This can be very beneficial especially for studies related to phase transformation phenomena.

- Another idea is to study the 3D features of grain fragmentation during plastic deformation by 3D-EBSD via serial sectioning. The developed method can be employed to derive the grain boundary character distribution of the deformed material. This information can be used to establish a link between the type of the grain boundary and the grain-grain interaction during plastic deformation.